Formation of Nanostructured Assemblies of Light-harvesting Proteins by Photochemical Methods

By Hang Xu

Department of Chemistry

University of Sheffield

A Thesis Submitted to the University of Sheffield for the Degree of Master of Philosophy

November 2015

Acknowledgement

I would like to express my deep gratitude to Prof. Graham J. Leggett for his patience, support, guidance, valuable advice, constructive suggestions and comments throughout my MPhil.

A special thank goes to GJL group members past and present, Anna Tsargorodska, Brice Darroch, Abdullah Al Souwaileh, Omed Al-Jaf, Jessie Xia, Nan Cheng, Alexander Johnson, Paul Chapman, Najwa Latif, Mar Cardellach, Charlie Smith, Oscar Siles-Brugge, Max Chambers, Rob Ducker and Samson Patole for their helps and friendship.

I would like to dedicate this work to my dear parents Xuefeng Xu and Yabo Zhou. I would never make it without their priceless support, love and patience. This gratitude also goes to my grandparents, my aunts, uncles and cousins (Chenming Zhou, Dan Zhou, Huifang Han, Shanshan Liu, Taoran Zhou and Ruike Sun) my friends in China Caibo Yue, Zhenpeng Zuo, Xiaoyao Deng and Lixin Zhang for their love and accompany.

To my best friends in UK, Bo Chen, Xiaoting Chen, Youcao Ren, Jie Gao, Jia He and Yuhua Wang, and all the other friends and housemates in Opal 2 and 59 summer street for their moral and friendship.

Contents

Abstract

The main focus of this project was the formation of the nanostructured assemblies of light-harvesting proteins by photochemical methods. Scanning near-field photolithographic and interferometric lithographic approaches were utilized to fabricate the desired nanopatterns and light-harvesting proteins were immobilized on these nanopatterns.

Self-assembled monolayers (SAMs) of an oligo (ethylene glycol) functionalized trichlorosilane were fabricated on both mica and silicon substrates. SAMs formed on mica substrates were compared with those on silicon substrates in water contact angles, ellipsometric thickness, atomic force microscopy (AFM) roughness and AFM height measurement. X-ray photoelectron spectroscopy (XPS) spectra were obtained to enable the detailed characterizing of these SAMs. Kinetic studies were performed by varying the preparation time of each specimen, to enable determination of the optimum immersion time to yield high quality monolayers for photolithography and optical readout.

SAMs of aminopropyltriethoxysilane protected by oligo (ethylene glycol) modified 2-nitrophenylethoxycarbonyl (OEG-NPEOC-APTES) were fabricated on mica substrates. The behavior of the OEG-NPEOC-APTES surfaces on exposure to X-ray was studied by comparing the XPS N1s spectra as a function of time. Micron and nanometer scale patterns were yielded by mask-based, scanning near field photolithographic and interferometric lithographic methods. Proteins were immobilized on these patterns.

Chapter 1. Introduction

1.1 Self-Assembled Monolayers (SAMs)

The name "self-assembled monolayer" (SAMs) was coined by a journalist in New Scientist in 1983 describing the work of Jacob Sagiv and co-workers[1], on defining the well-controlled self-assembled multilayer films. Their research was inspired by the basic approach which is still common in modern monolayer-building methods that was devised by Langmuir and Blodgett (LB) several decades earlier. In 1930s, Irving Langmuir and Katherine Blodgett described an approach to the formation of monolayers of amphiphilic molecules on the surface of water or suitable volatile solvent and their subsequent transfer to a substrate that was passed through the film as shown in figure 1.1. This procedure could be repeated for certain times and each time a further layer was added to the newly formed layers increasing the film thickness. Sagiv and co-workers achieved a step forward in avoiding some of the inherent drawbacks in the LB method resulting from the use of mechanical manipulation in the fabrication and superposition of monolayer films. Thus, a method where monomers spontaneously associated and organized at the solid-liquid interfaces which was known as self-assembly was introduced to us[1-4]. In this method, the properties of a surface could be completely changed by this self-assembled, a few nanometers thick films regardless of the shape, size or state of dispersion of the solid substrate. It was a spontaneous process in which covalent bond, formed between the adsorbates and the substrate, providing a very stable foundation and leading to minimization of the total interfacial free energy of the system. Multilayers were also accomplished in the same approach simply by chemical activation of the exposed outer surface. Moreover, this superior method could be managed in many ways, e.g., structure of the adsorbates, density of components, the choice of substrates, cleanness of the substrates, time of formation, solvent properties and circumstance, such as temperature, humidity and luminance for further applications. These aspects will be discussed in the subsequent review [5, 6].

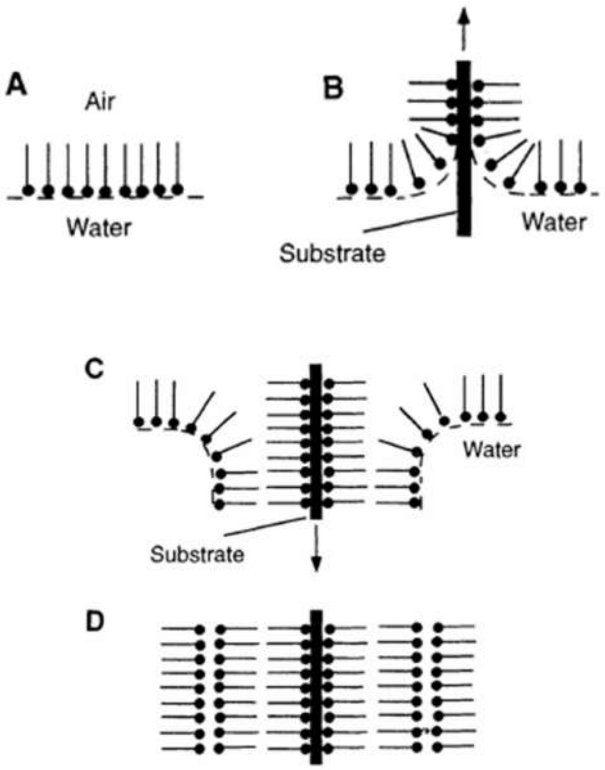

Figure 1.1 Schematic diagrams showing monolayer and multilayer formation on a solid substrate using the Langmuir-Blodgett technique.[4]

1.1.1 Components and substrates

The advantages offered by SAMs are mainly due to the chemical characteristics of their component molecules and the way in which those components are arranged in monolayers.

Figure 1.2a shows the basic structure of a SAM system. It includes three parts, namely head group, alkyl chain and surface-active tail group. The head group interacts strongly with the substrate and the energy of the covalent bond that forms between the head group and substrate is the factor that influences the quality, stability and density of the monolayer. This also means that different combinations of head group and substrate can form different monolayers that are stable in various circumstances. For example, the well-studied and regularly used combinations are alkanethiol (R-SH) and Au, Ag, Cu, Pt; alkylsilane ($R\text{-}SiCl_3$) and SiO_2; alkylphosphonate ($R\text{-}PO_3^{2-}$) and transition metal acides; fatty acid and AgO, Al_2O_3. Here the formation of alkanethiol and alkylsilane SAMs will be discussed in detail. Because the formation of SAMs depends on the formation of a chemical bond between the active head group and the

substrate, the specific characteristics of substrates also limit the types of monolayers that can be grown on them. Only when the cross-sectional diameter of the alkyl chain of the adsorbate molecule is smaller than the distance between the anchor groups, does a well-packed and ordered SAM form.

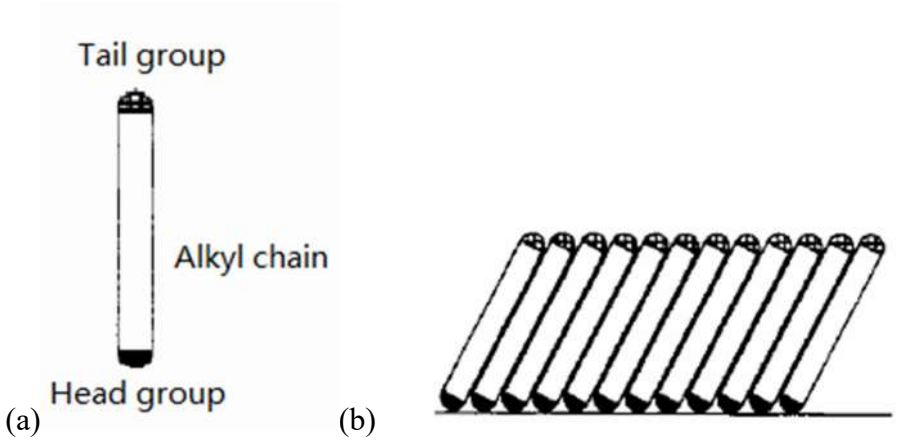

Figure 1.2 Schematic representations of (a) components of SAMs and (b) a well-packed monolayer.

The length of the alkyl chain directly controls the thickness of the SAMs, the space between two layers or substrate and multilayers. Not only the molecular arrangement but also any inter-chain interactions between chemisorbed molecules can be affected by differences in adsorbate alkyl chain lengths and other structural characteristics of the adsorbate. For instance, work by Bain and Whitesides (figure 1.3) on monolayers formed by the coadsorption of two thiols with different alkyl chain lengths revealed that when the substrate was immersed in a solution of these two thiols, an inner part of the monolayer formed that was well-packed, but the outer part of the monolayer became disordered and liquid like, because of the existence of the shorter chain, the longer chain would lose lateral support[7]. Since both the longer and the shorter thiols themselves could form well-packed, pseudo crystalline, oriented monolayers, the smoothness of the resulting surface strongly depended on the similarity of the chain lengths in cases where more than one thiol was involved.

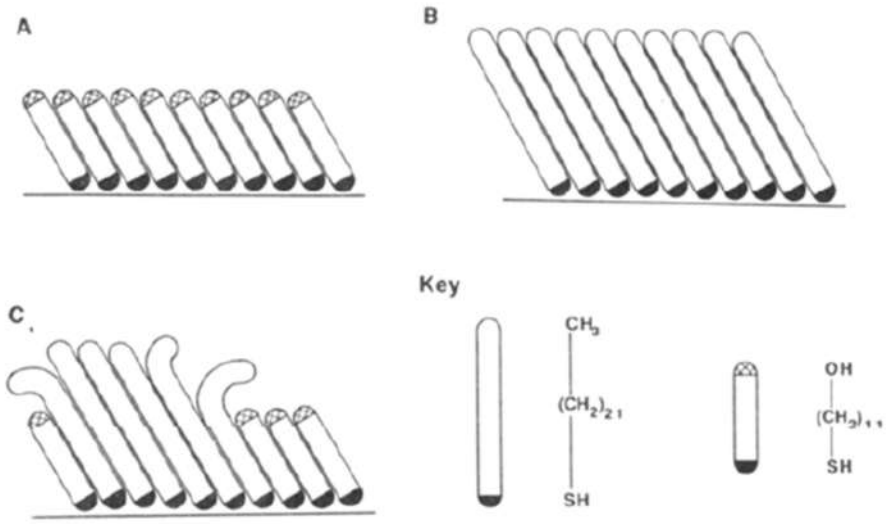

Figure 1.3 Schematic diagrams illustrating the comparison between a one-component monolayer and a two-component monolayer formed from adsorbates with different alkyl chain lengths. In A and B, both thiols form well-packed monolayers on the substrates when there is a mixture of the two thiols (C) the monolayer forms a disordered and liquid-like surface.[8]

Once the SAM formation process completed, and a well-packed and ordered monolayer has formed, the tail group is the factor that determines the properties of the newly formed surface. A wide range of tail groups, such as the hydroxyl group (-OH), nitrile group (-CN), carboxyl group (-COOH), alkene (-CHCH2) and amino-group (-NH_2), can be chosen to introduce desired functionalities to SAMs.

1.1.2 SAMs of alkylthiolates on Au(111)

Although there are several metal such as Au, Ag, Pt, Ti and Cu that can react with alkanethiols and form monolayers, the most well-defined are thin Au films on silicon wafer, mica or glass. This is due to the stability of gold which does not normally from surface oxides, in contrast to other metals i.e. copper, silver or titanium, and the covalent bonding energy of Au-S which is quite high. In studies of temperature-programmed desorption, Dubois *et al.* estimated that the energy barrier to desorption of alkylthiolates from Au(111) was ca. 125 $KJmol^{-1}$.[12] Calculations by Schlenoff *et al.*[9] and Sellers[10] indicated that the net adsorption energies for chemisorption on Au(111) were 12.7, 9.4 and 5.5 kcal/mol respectively for CH_3SH, H_2S and RS-H, where R contains at least two carbon atoms. Their results suggest that the hemolytic

bond strength of RS-Au is approximately 40-50 kcal/mol [11]. In the absence of oxygen, the reaction was take place on gold surface is believed to follow the equation:

$$R-S-H+Au_n^0 \rightarrow R-S^-Au^+ \cdot Au_n^0 + \frac{1}{2}H_2 \qquad (1.1)$$

Work by Fenter *et al.* [13] and Chidsey *et al.* [14] using helium diffraction and atomic force microscopy revealed that the adsorption site of sulfur atoms is in the 3-fold hollow of the gold lattice and is a simple $\sqrt{3}\times\sqrt{3}$R 30° overlayer with a c(4×2) superlattice (figure 1.4).

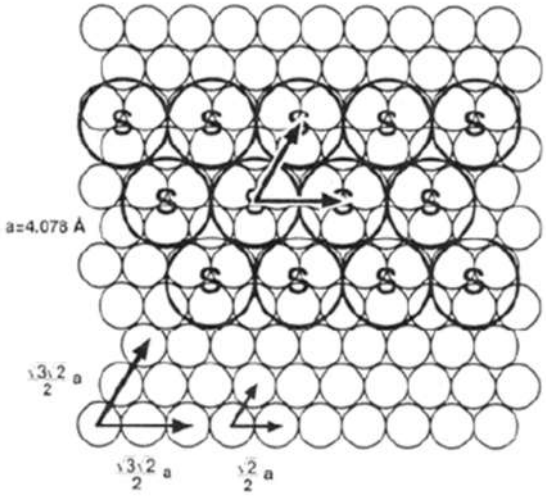

Figure 1.4 A top view of Au(111) surface with a thiolate overlayer. The big circles with S represent sulfur atoms from thiolate which site in the 3-fold hollow of the gold lattice.[8]

The formation process of this thiolate overlayer can be divided roughly into two steps, namely high speed adsorption and low speed crystallization and self-exchange. As the names suggested, these two significantly different steps were observed by experimental studies in most cases of thiolate adsorption. In relatively dilute solution (1 mM), the first step was followed in real time by second harmonic generation and analyzed by contact angle goniometry and X-ray photoelectron spectroscopy, finding out that, in about 2 mins, the surface was 80-90% covered by thiolate and the thickness of overlayer was approaching to the maximum value[16]. The second step could last from several minutes to a few days. During this stage, the disordered layer

formed in the first a few minutes crystallized gradually to form a ordered two-dimensional array[15].

1.1.3 Alkyl siloxane SAMs on silica

Silicon exposed to air at room temperature will form a thin layer of native oxide on its surface. This thin layer interacts with the outer environment of the silicon wafer and influences the reaction with alkylsilane remarkably. The chemical properties of this native oxide layer were investigated by many researchers. It has been found that the amount of adsorbed water or hydroxyl groups on the oxide surface plays an important role in the SAM growth[17-20]. For example, the reaction of chlorosilanes with a hydrated oxide surface is as follows:

$$Cl - SiR_3 + H - O - R' = R' - O - SiR_3 + HCl \quad (1.2)$$

If R' is silicon dioxide and R is an alkyl group, then the breaking of Cl-Si and H-O covalent bonds enables the formation of an R'-O-Si bond and the transformation of a normal oxide to the desired surface. However, when silicon oxide and chlorosilanes exist in absolutely dry conditions or the water layer is too thin, the reaction does not proceed[18]. On the other hand, the presence of too much water promotes the polymerization of chlorosilanes in solution which results in a lower coverage, or the deposition of the clumps of the pre-polymerized adsorbates.

Figure 1.5 shows the 4 steps in which the self-assembly process take place. Step 1, the physisorption of alkylsilanes onto the hydrated surface, is followed by reaction between surface silanol group and the silane, step 2 and the formation of covalent bond (step 3) to the surface. When unreacted alkylsilane molecules approach a surface that is partially covered by silanes, they may either react with surface silanol groups, or form cross-links to adsorbates before themselves forming covalent bonds to the surface. The alkyl chains are disordered at the point. However, over time the film approaches equilibrium in which the alkyl chains are close-packed. The time takes to react equilibrium depends on several factors including, in particular, the nature of the head group, with film formation coming to completion much faster for $SiCl_3$ than for $SiOR_3$. There are 3 principle factors which influence the reaction, namely the concentration and volume of the solution and the reaction time. As the concentration

of the solution increases, the rate of the collision of the adsorbates with the surface increases. The formation of the monolayer is promoted. The decreasing of volume has the same effect[21].

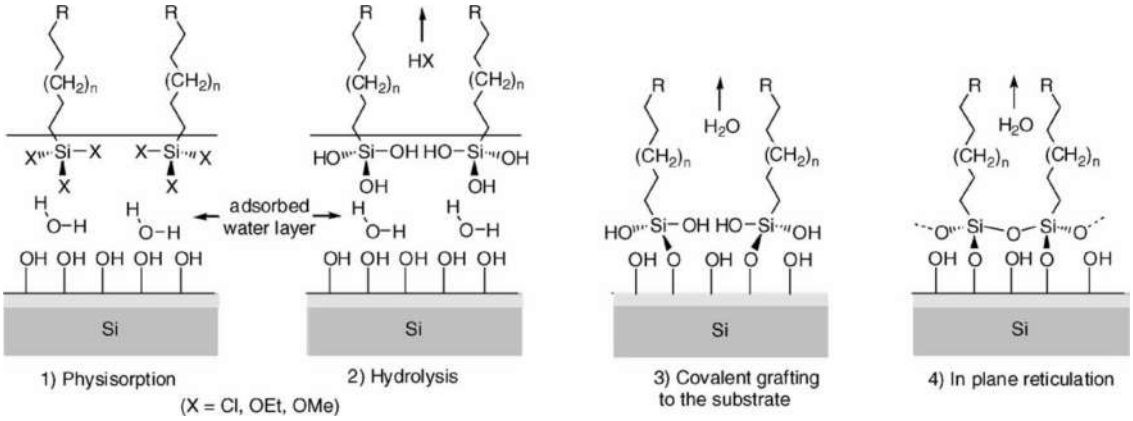

Figure 1.5 Schematics of the 4 steps of the formation of alkyl siloxane SAMs on silica.[21]

1.1.4 Formation of films of alkylsilanes on mica

The mechanism of the formation of SAMs on mica is thought to be similar to that which applies to silicon dioxide.[43-45] Hydrated alkylsilanes are covalently bonded both with the mica surface and with other adsorbed alkylsilanes by cross-linking.

The composition of mica was investigated (table 1.1) by Jia *et al.* [22] using X-ray fluorescence spectrometry. Mica is a material rich in Al^{3+}, Mg^{2+} and Na^{+}. The 3D structure of mica is a "sandwich" with a layer of octahedral coordinated Al^{3+} ions lying between two layers of silica tetrahedra above and beneath. The negative charges generated from these layers are counterbalanced by the K^{+} ions located in the inner layer. However, this structure makes it challenging to form SAMs on mica because it presents a comparatively low density of silanol groups on which adsorbates may be robustly anchored. It is 2D polymerization among alkylsilanes in the solution before anchoring to mica surface that enables multi-functional alkylsilanes to form SAMs while mono-functional silane will not connect to mica surface as the hydroxyl groups are inaccessible[22-25].

Table 1.1 Components in mica analyzed by X-ray fluorescence spectrometry.[22]

Composition	wt %	Standard error	Element	wt %
SiO_2	47.91	0.25	Si	22.40
Al_2O_3	34.63	0.24	Al	18.33
K_2O	10.30	0.15	K	8.55
Fe_2O_3	4.85	0.11	Fe	3.40
Na_2O	0.69	0.034	Na	0.51
MgO	0.67	0.033	Mg	0.40
TiO_2	0.62	0.031	Ti	0.37
Others	0.33	-	Others	-

Because it was a layered crystalline structure, mica yields atomically flat surface planes when cleaved and is widely used in scanning probe microscopy. As silicon wafers and glass slides have greater roughness than mica, mica as a substrate is essential when high-resolution imaging is required.

1.1.5 SAM stability

The important roles played by humidity, concentration and immersion time in the process of the formation of SAMs have been discussed before both for alkanethiols and alkylsilanes. However, they also affect the long-term stability of SAMs.

Firstly, the time-dependent evolution of the organization of adsorbates follows the sequence: (i) nucleation of adsorbates with small molecular cluster at very initial stage; (ii) formation short stripes followed by growth of the ordered phases and finally (iii) formation of a dense structure[29]. Increasing the concentration of components or prolonging the immersion time of substrates promotes the formation of monolayers or even multilayers and accelerates the adsorption onto substrates[26,27]. However, these effects were not guaranteed to occur above a critical concentration. It was also observed that no further layers were formed for reactions under certain circumstance no matter how long the immersion time was[28].

Secondly, numerous experimental results show that the relative humidity in the ambient is critical[18,28,30]. The monolayer fabricated by Rozlosnik *et al.* [28] under strict control of humidity illustrated that a high quality and well-defined monolayer required a thin aqueous layer (relative humidity 40%-60%) on the surface of the substrate while anhydrous conditions were needed in the solvent.

Finally, the solvents and environmental temperature also influence the formation process dramatically. Tan and co-workers[31] found that the solubility of solvents significantly controlled the growth of SAMs which meant in order to obtain the highest quality of coverage it was necessary to synchronize the polarity of the solvent and components. Temperature was also formed to be an important parameter. Coverage decreased with increasing deposition temperature above a critical growth temperature (approximately>28˚C). If the increase continues, the processes that may occur are phase transition, desorption and dissociation[32]. Naturally, SAMs have specific melting temperatures and will melt when being heated but silane-based monolayers show greater thermal stability than thiol-based monolayers. At a temperature below the melting point, organizational arranges may occur including the evolution of disorder and gauche defects.

1.1.6 Photooxidation of SAMs

Numerous research articles illustrated the mechanism, process and products from the photooxidation of alkanethiols[33-36]. However, those from alkylsilanes were remained less documented. The type of photochemical reactions observed is different for the two types of SAM. Ultraviolet (UV) irradiation causes either a spatially resolved degradation or chemical modification. Under irradiation at short wavelengths, it was believed that the step-wise photooxidation mechanism occurs as follows when the wavelength of the excitation laser is ca. 190 nm[37].

Table 1.2 Step-wise photooxidation mechanism.[37]

$R{-}H + O \rightarrow R^{\bullet} + HO^{\bullet}$	(L1)
$R^{\bullet} + O_2 \rightarrow ROO^{\bullet}$	(L2)
$ROO^{\bullet} + h\nu \rightarrow RO^{\bullet} + O$	(L3)
$ROO^{\bullet} + HO^{\bullet} \rightarrow RO^{\bullet} + HOO^{\bullet}$	(L4)
$RCH_2O^{\bullet} + O_2 \rightarrow RCHO + HOO^{\bullet}$	(L5)
$RCHO + h\nu \rightarrow R^{\bullet} + CHO^{\bullet}$	(L6)
$RCH_2CHO + O \rightarrow RCH^{\bullet}CHO + HO^{\bullet}$	(L7)
$RCH^{\bullet}CHO \rightarrow RCH_2^{\bullet} + CO$	(L8)
$RCHO + O \rightarrow RCO^{\bullet}$	(L9)
$RCO^{\bullet} + O_2 \rightarrow RC(O)\,O_2^{\bullet}$	(L10)

From the above equations, it may be seen that the initial step is the homolysis of a C-H bond, leading to the formation (L1), of peroxide radicals (L2-4) which may be

oxidized further into carbonyls (L5). Aldehyde groups may undergo further photolysis causing loss of carbon (L6-8) while RCHO groups yield $RCO^{\cdot}$ in the final step (L10), which are the precursor to carboxylic acids. Hence, the alkyl chain gradually shortened during these reactions[36].

As we have been discussed, all these outstanding features of SAMs above drew wide attention from researchers who were looking for a model template in the study of nanoparticles, surface modification, nanoscale fabrication and interaction between substrates and biological nanostructures.

1.2 Surface lithography methods

1.2.1 Micro-contact printing

Mirco-contact printing (μCP) was invented by Whitesides and co-workers in 1990s[38]. This technique is a direct patterning method which enables the transfer of organic molecular[39], polymer brushes[40] or nanoparticles[41,42] inks from a elastomer mold to various substrates in a design pattern. It was subsequently developed into a range of techniques known collectively as "soft lithography".

The mechanism of micro-contact printing, which includes moolding, inking, printing and surface derivatization, is shown schematically in figure 1.6. The manufacture of a pattern is simple. A low molecular weight prepolymer is cast onto a silica relief master. After curing (cross-linking) the polymer is peeled off the master and used as a stamp. The surface of the stamp is "inked" by coating within a solution of the adsorbate of choice prior to transfer to the substrate by mechanical contact. During the procedure of printing, it is the conformal contact between the stamp and the substrate that determines the amount of ink solution adsorbed and while printing the adsorbates the ink diffuses from the stamp onto the substrate to form a pattern[46]. There are several patterning routes. For example, lattice and rhombus patterns can be formed by double printing of features in thin lines[38], followed by selective deposition to achieve multiple component surfaces. Wet etching of metals is accomplished by patterning a SAM which prevents the metal surface from dissolving, such as hexadecanethiol on a gold surface. Exposing a hexadecanethiol-patterned gold surface to an etchant results in the dissolution of gold in the unprotected areas. This method is useful for the

producing of arrays of micro-electrodes[47].

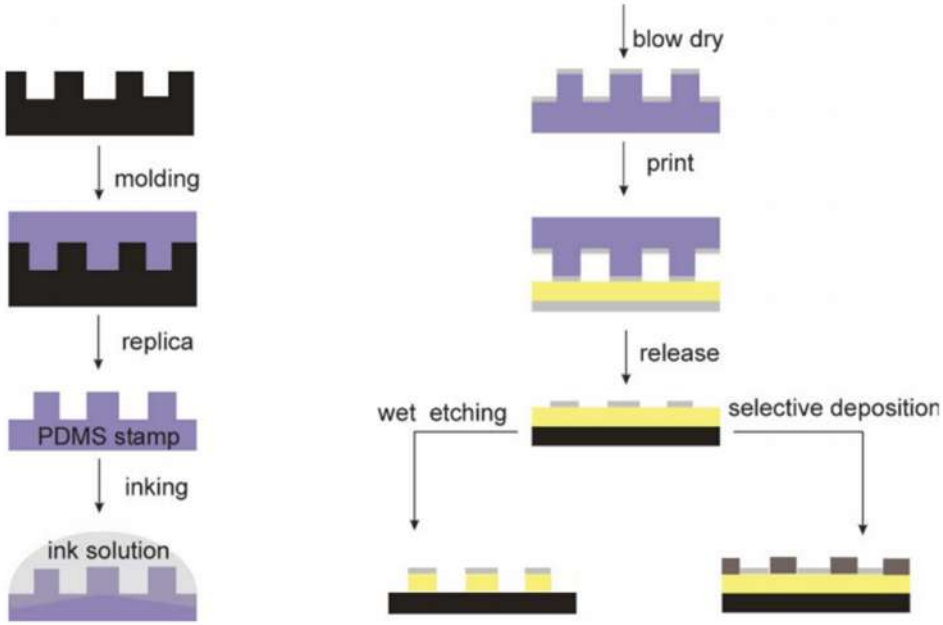

Figure 1.6 Schematic representation of the process of micro-contact printing.[46]

1.2.2 Electron beam lithography

Electron beam lithography was developed for patterning nanometer scale features (as small as sub-10 nm) because, while diffraction effects limit the improvement in resolution of conventional photolithography, the wavelength of electrons is much smaller and diffraction is not a problem on nanometer length scales. Electron beam lithography requires the exposure of an electron sensitive surface referred to as a resist which causes modifications of the structure of the resist, rendering it either less or more soluble. Through subsequent development of the resist, the features of the modified regions of the resist can be transferred subsequently to the substrate[56,59].

The most widely used resist is poly(methyl methacrylate) (PMMA). Chang *et al.* reported using electron beam lithography to form patterns on irregular and fragile substrates with PMMA. PMMA was spin-coated and baked to dry in order to be peeled off forming a free-standing PMMA film. This film could be topped or attached to irregular surfaces. Subsequently, with the ability to control inter-feature spaces precisely, electron beam lithography accomplished the production of patterns on infeasible surfaces for other lithographic techniques[57].

1.2.3 Photolithography

1.2.3.1 UV laser lithography through a mask

Photolithography was been used widely to pattern SAMs[34-37,66-70]. Localized photooxidation was carried out by far field laser irradiation through a mask to generate patterns consisting of selectively activated surfaces to be used for further reactions. However, the resolution of this method was limited by diffraction effects.

1.2.3.2 Interferometric lithography

Interferometric lithography (IL) is a simple but powerful technique that utilizes a laser beam to produce rapidly nanometer-scale periodic features over a macroscopic area. Many works utilized commercial developed laser source such as 244 nm (frequency-doubled argon ion laser), 364 nm (continuous-wave Ar^{++} lines) and 355 nm (third-harmonic of YAG laser)[66,71]. The concept of IL is shown schematically in figure 1.7 while the period of features generated by IL is given by:

$$d = \frac{\lambda}{2sin\theta} \qquad (1.3)$$

where the period (d)of the generated interference pattern depends on the laser source wavelength (λ) and the angle (θ) at which two laser beams interfere. Figure 1.7 shows a schematic representation of a Lloyd's mirror interferometer, where one half of a coherent beam strikes the sample and the other half strikes a mirror, from where it is reflected onto the sample to interfere with the first half of the beam[68]. By keeping the mirror-sample angle at 90˚, the smallest period is achivable at normal incidence to the Lloyd's mirror where the laser source is equally divided between top and down which means θ=45˚ and d=λ/√2.

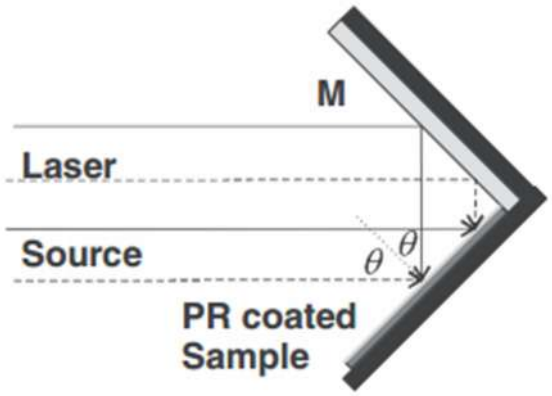

Figure 1.7 schematic representation of Lloyd's mirror arrangement for two-beam interference IL.[66]

A variety of photoresists has been successfully patterned on different length scales using IL, including PMMA[69], oligo(ethylene glycol) (OEG) terminated silane[70], alkanethiolates on gold[68] and alkylphosphonates on titanium oxide[67]. Two images characterized by AFM for conventional IL patterns are shown in figure 1.8 (a, b). Nanodots were yielded by Tsargorodska *et al.* in double exposure fashion by rotating the sample on the stage through an angle between two exposures (figure 1.8 c, d). By controlling the interference angle between two parts of the beam and the rotation angle, the sizes of the nanodots could be managed which allowed selectively wet etching and deposition for nanofibres or nanoparticles in the same scale. The effects of annealing were also explored in this work. A high degree of crystallinity and good optical properties including strong plasmon bands were witnessed by comparing annealed and unannealed samples characterized by X-ray diffraction and AFM[68].

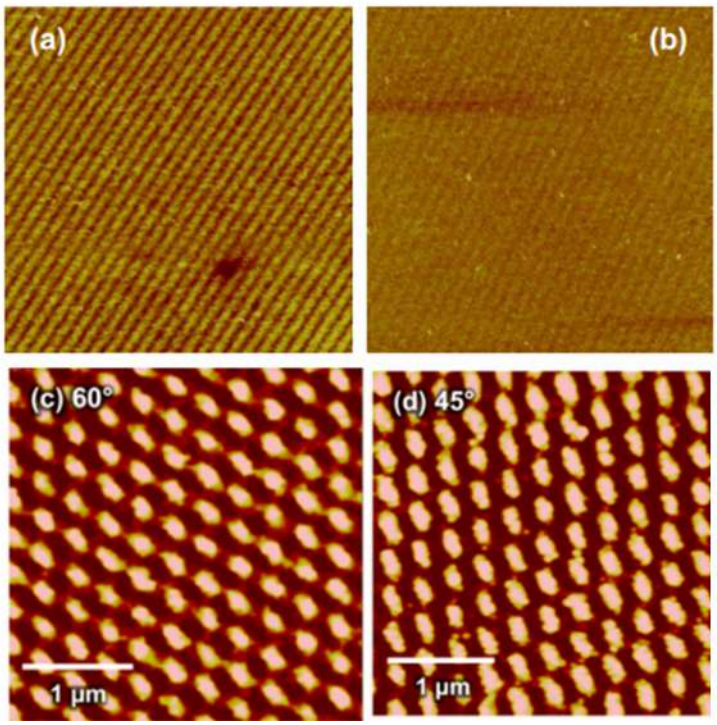

Figure 1.8 (a) AFM topographical images of as-prepared nanostructures, size: 5.7× 5.7 µm^2, and z-range of 0 – 7 V; (b) size: 5.7× 5.7 µm^2, and z-range of 0 – 1 V; (c, d) Samples fabricated using two exposures with varying angles of rotation between exposure.[68,69]

1.2.4 Scanning probe lithography

Scanning probe lithography (SPL) uses scanning probe microscope to create nanopatterns on solid substrates. Scanning probe lithography can be divided into two main types namely, addition lithography and elimination lithography. What will be discussed here are 'dip-pen nanolithography' as addition lithography and 'nanoshaving and nanografting' and 'scanning near field lithography' as elimination lithography[46].

1.2.4.1 Dip-pen nanolithography

Dip-pen nanolithography (DPN) was invented and developed by Mirkin *et al.* in 1999[48]. DPN uses adsorbate solutions as 'ink', cantilevers and tips from atomic force microscopy (AFM) as 'nib' and substrates of interest as 'paper' to 'write' patterns of nanometre or angstrom resolution directly (figure 1.9). The lithographic process of DPN relies on surface affinity of substrates and the capillary force between the tip and

the contacting surface[49-51]. Under ambient conditions, a water meniscus forms between a tip and a substrate, providing a path for transfer of adsorbate solution to the substrate. The feature size may be influenced by the humidity, translate rate and temperature[38]. Under the conditions of low humidity or high temperature, the evaporation of adsorbates solution will be so severe that it causes the formation of discontinuous lines. Increasing the rate decreases the sizes of the created pattern but will eventually, at high speeds, lead to the formation of discontinuous features[49].

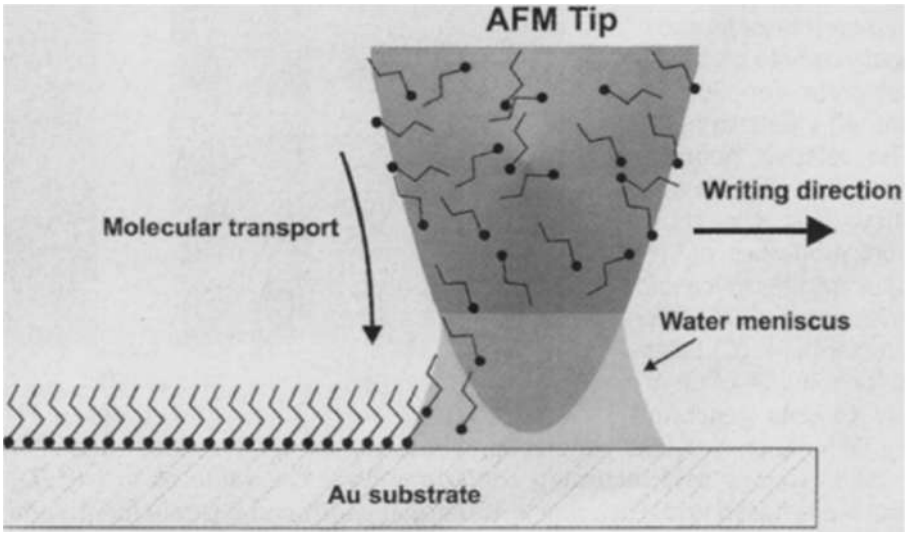

Figure 1.9 Schematic representation of DPN process.[48]

A significant drawback of DPN is that the translation rate is required to be relatively slow and, moreover, the process is intrinsically a serial one. Compared to micro-contact lithography or any other soft lithography, the formation of patterns over large areas is very slow. To address this problem, Mirkin and co-workers developed a 'nanoplotter', or probe array, in which a large number of probes is scanned simultaneously[52].

1.2.4.2 Nanoshaving and nanografting

As an elimination lithography technique, multiple component surfaces with high spatial precision down to sub-100 nm were fabricated by a combination application of nanoshaving, nanografting and dip-pen lithography[48,53]. The concept of this technique (figure 1.10) is to use an AFM tip to remove adsorbates molecules from a fully formed SAM in the presence of a second adsorbate which assemble into the bare regions

forming a molecule pattern.

The reason why nanoshaving and nanografting can obtain high spatial resolution is that unlike DPN, the resolution of this technique relies on the intrinsic stability and sharpness of the tip and the load applied rather than the texture of substrates or ambient conditions[55]. In order to both remove the existing SAM and prevent the tip from being irreversible damaged, the load exerted on the tip must lie within a narrow range. A high load of 5-50 nN is applied for shaving and a reduced load of 0.5-5 nN is used to characterise surface topography[51,54]. By changing the adsorbate each time operating nanoshaving, multiple components surfaces were successfully produced.

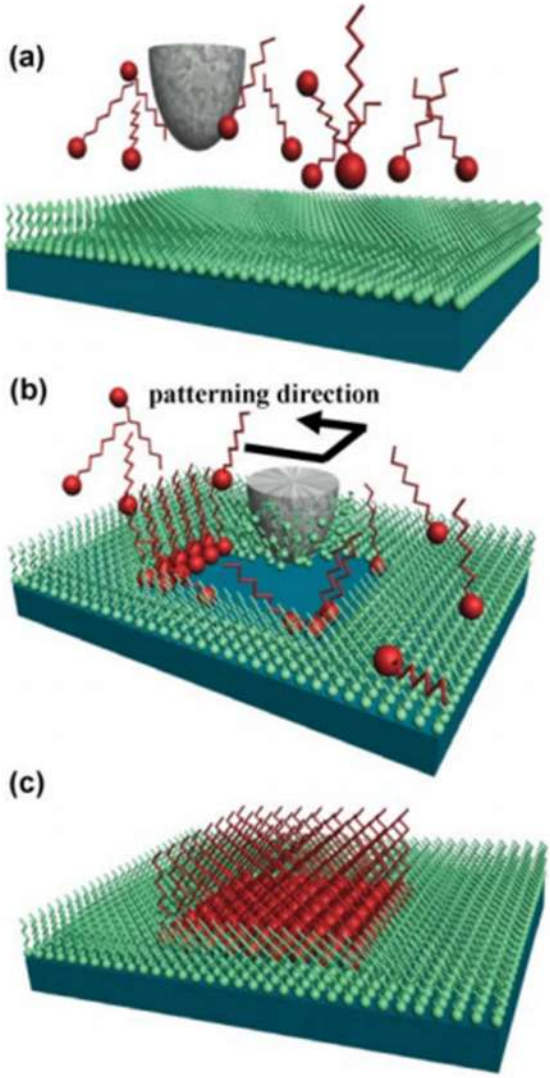

Figure 1.10 Schematic representations of nanoshaving and nanografting.[46]

Originally, nanografting was carried out in solutions for the unconstrainted self-assembly of the second adsorbate. During the prolonged process of nanoshaving, the exchange between ligands inside the solution and on the substrate cannot be neglected[46]. This concern was solved by Liu *et al.* with the development of a nanopen reader and writer (NPRW) which was performed in the air as the schematic demonstrated in figure 1.11[55].

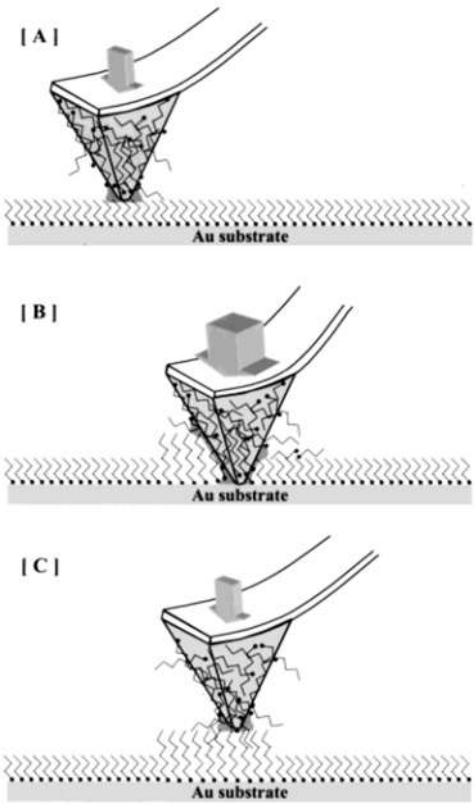

Figure 1.11 Schematic representations of nanopen reader and writer (NPRW).[55]

The nanografting lithography of NPRW was achieved by the exchange of adsorbate molecules between the precoated tip and the prepared SAM on the substrates. Since this exchange was a spatially constraint procedure, the deposition of new adsorbates was further accelerated because the molecules were delivered directly to the surface in high density and contact[55].

1.2.4.3 Scanning near field optical lithography

The diffraction limit still defines the ultimate resolution of optical lithography. Electron beam lithography was developed to surmount this fundamental barrier. Even

though some other optical lithography techniques (such as phase mask photolithography[61]) was reported to be able to provide pattern features smaller than excitation source wavelength, their resolution was not rivalled that of electron beam lithography. Scanning near field optical lithography, was developed as an alternative method to produce features with lateral resolution down to 9 nm, significantly smaller than the diffraction limit and rivalling the resolution of electron beam lithography[60].

Scanning near field optical lithography employs a combination of scanning near field microscope (SNOM) and an excitation source (UV laser) which is coupled to a probe consisting of either a tapered optical fibre or a hollow pyramidal tip attached to a cantilever. The probe is, in both cases, coated with an opaque metal film such as aluminium[56] as the schematic illustrates in figure 1.12.

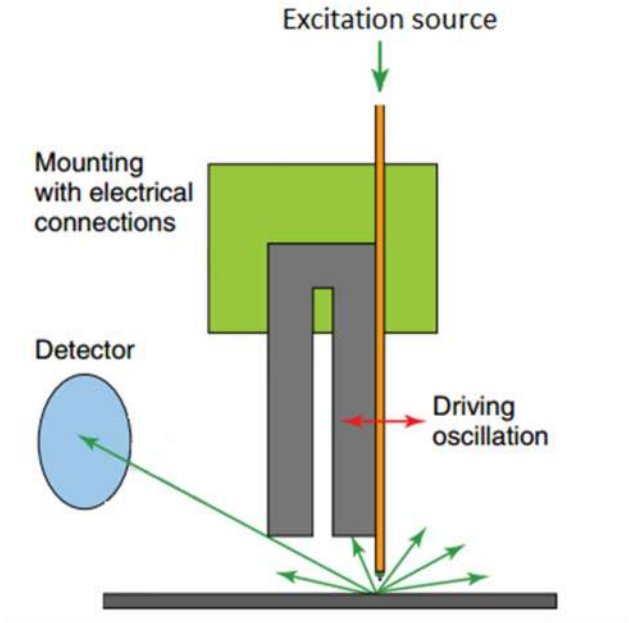

Figure 1.12 Schematic diagram of scanning near field optical lithography.[56]

Localized photooxidation performed by SNOM utilizes various systems consisting of photo sensitive SAMs to generate features on the nanoscale. Sun *et al.* used a frequency-doubled argon ion laser (λ=244 nm) coupled to a SNOM which enabled alkanethiolates and 4-chloromethylphenylsiloxane (CMPTS) to be transformed into alkanesulfonates and carboxylic acid terminated siloxanes, respectively, that could be further reacted in a liquid-based procedure. During exposure of CMPTS, the Cl-C

bond was broken by UV irradiation in a homolysis fission. Following the homolysis, an aldehyde group was formed firstly, and subsequently on extended exposure, the aldehyde group was oxidized into a carboxylic acid group[60,64]. Credgington *et al.* reported similar nanostructures formed on conjugated polymers such as poly(*p*-phenylene vinylene), PPV and crosslinkable poly(9,9'-dioctylfluorene) with a lateral resolution below 60 nm (<λ/5). Their work opens routes to the site-selective insolubilization of a precursor polymer under exposure to the confined optical field[63].

Alang Ahmad *et al.* reported the characterising of the protection group, nitrophenylpropyloxycarbonyl protected aminopropyltriethoxysilane (NPPOC-APTES), which underwent photocleavage (scheme 1.1) under UV irradiation (λ =325 or 364 nm). Without the addition of carbonyl scavenger, NPPOC-APTES accomplished a superior photodeprotection efficiency by yielding an alkene byproduct to display an amine terminate group at the surface. By immersing the photooxidized specimen in the solutions of different reagents, surface derivatization was achieved. In this way, SAMs formed with NPPOC-protected alkanesiloxane were repeatedly patterned with features on different length scales[62].

Scheme 1.1 Proposed mechanism of NPPOC deprotection by UV laser.[62]

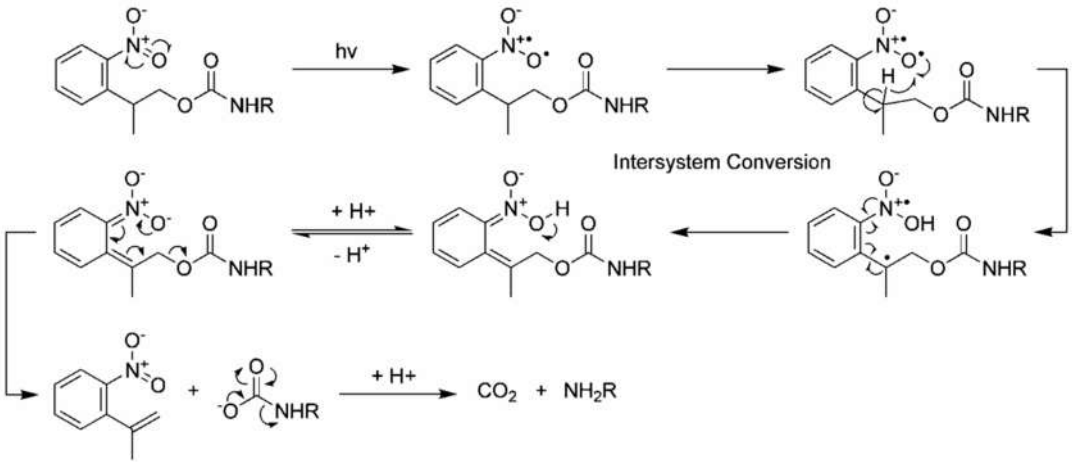

1.3 Protein patterning

1.3.1 Autofluorescent proteins (AFPs)

Autofluorescent proteins (AFPs) have become a major tool in biochemistry and cell biology research with numerous variants being cloned every year and a large number of reports available since the discovery of green fluorescence in *Aequorea* in 1955 by Davenport *et al;* They discovered the fluorescent properties of green fluorescent protein (GFP) isolated from the jellyfish *Aequorea victoria* (*A. victoria*)[72]. In 1992 the gene of GPF was first cloned by Prasher *et al*[74]. An explosion of interest has been witnessed since then because of two attractive properties of GFP. On one hand, without adding any cofactors for posttranslational modification or folding, GPF displays fluorescence once exposed to other organisms. On the other hand, GFP produces fluorescence when fused with other proteins which means that GFP can act as a fluorescent tagging agent enabling specific proteins to be tracked in living cells by simple techniques[75].

Ormo *et al.* reported that the structure of AFPs contains a universal secondary structure element which is an 11-stranded β barrel wrapped around a single central helix. The crystal structure and the overall folding of GFP are shown in figure 1.13. The α helix is buried deeply inside the β barrel structure while both N- and C- termini are exposed outside. Thus, the α helix (i.e. fluorophore) of GFP is unreachable for solvents or fused proteins and peptides, which provides GFP with relatively low environmental sensitivity comparing to other proteins and the function of fluorescent tagging by fusing with other proteins[76]. The stability of wild-type GFP (wtGFP) is reflected in producing normal fluorescence even at 70˚C, in a crystal or when frozen. However, the fluorescence of wtGFP reacts to certain ambient conditions such as pH[73].

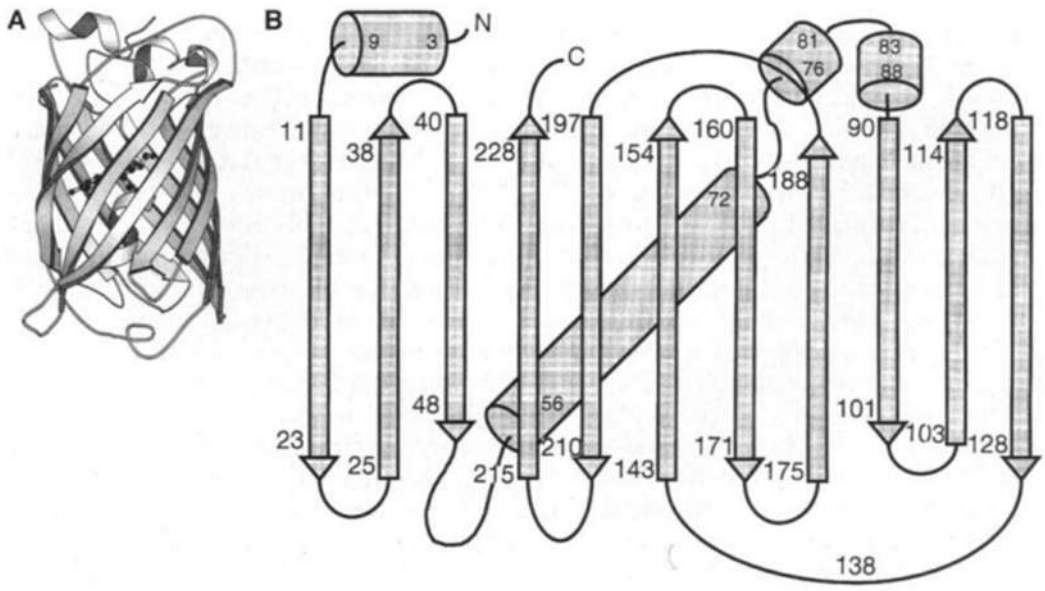

Figure 1.13 (a) Crystal structure of GFP with the β barrel shown in structural cartoons and the core chromophore in a space-filling representation. (b) Schematically showing the overall fold of GFP with approximate residue number at the beginning and ending of the secondary structure elements where N represents -NH_2 terminus and C represents –COOH terminus.[76]

WtGFP has two absorption maxima at 395 and 475 nm and yields an emission at 505 nm with a quantum yield of 0.72 to 0.85 if excitation occurs at the primary absorption peak of 395 nm. The problem is that although GFP has two excitation photon wavelengths, it shows a single emission peak in the spectra. Hence, numerous efforts have been made to modify the spectral properties of wtGFP in order to provide a palette of proteins with a number of excitation and emission spectra which resulting in a series of derivatives. Shaner *et al.* looked at the fluorescent properties of a number of variants aiming to find the best fit for different experimental purposes. Enhanced GFP (EGFP) performed quite well in this comparison. It folded normally at both room temperature and at 37˚C. Moreover, it displayed a relatively high photostability as the protein which took the longest time (actually 174 s) to be bleached from an initial emission rate of 1000 photons/s down to 500 photons/s upon excitation[77].

1.3.2 Light-harvesting proteins

Photosynthesis is a process that involves the transformation of light energy, which is harvested by pigments organized in a protein complex, into clean and stable chemical

energy, which furnishes the world with power. The 'factories' where the photochemical reactions take place are photosystems (PS). In green plants, the light-harvesting antennae are light-harvesting complex I (LHCI) and light-harvesting complex II (LHCII) for PS I and PS II, respectively, which bind chlorophyll *a*, chlorophyll *b*, and carotenoids. In algae (rhodophytes), the type of bound chlorophyll is only chlorophyll *a* while it is chlorophyll *a* and *c* in chromophytes, haptophytes and dinoflagellates[78,79].

Consider the integral membrane light-harvesting complex II (LH2) of the purple bacterium *Rhodopseudomonas acidophila (Rps. acidophila)* strain 10050. Papiz *et al.* investigated the structure of B800-850 LH2 at a resolution of 2.0 angstrom and 100 K which was shown schematically in figure 1.14[80,84]. The reason why this bacterium is called B800-850 is because the two types of pigments it contain, which are bacteriochlorophylls (BChls) and carotenoids. The bacteriochlorophylls are arranged in two rings, the B800 ring, absorbing at 800 nm, and the B850 ring, absorbing at 850 nm. The B800-850 LH2 complex structure: figure 1.14 (a, b) top view into LH2 lumen; figure 1.14 (c, d) side view. The apoproteins (β-chains) are shown as ribbons (purple) while the α-chains are in light-green. The BChls as are in dendritic structures where a-B850 (red), b-B850 (green), B800 (blue) and rhodopin glucoside (orange). The N terminus is left exposed at the bottom of figure 1.14 (c, d) (orange) while at the top of figure 1.14 (b, c) are where the C terminus located. The newly found C terminus residues can be seen extending upwards (light-green) at the top of figure 1.14 (d). The detergent structure of B800-850 LH2 was explored in crystals by Prince *et al.* at a resolution of 12 angstrom which was determined by neutron crystallography[81,87].

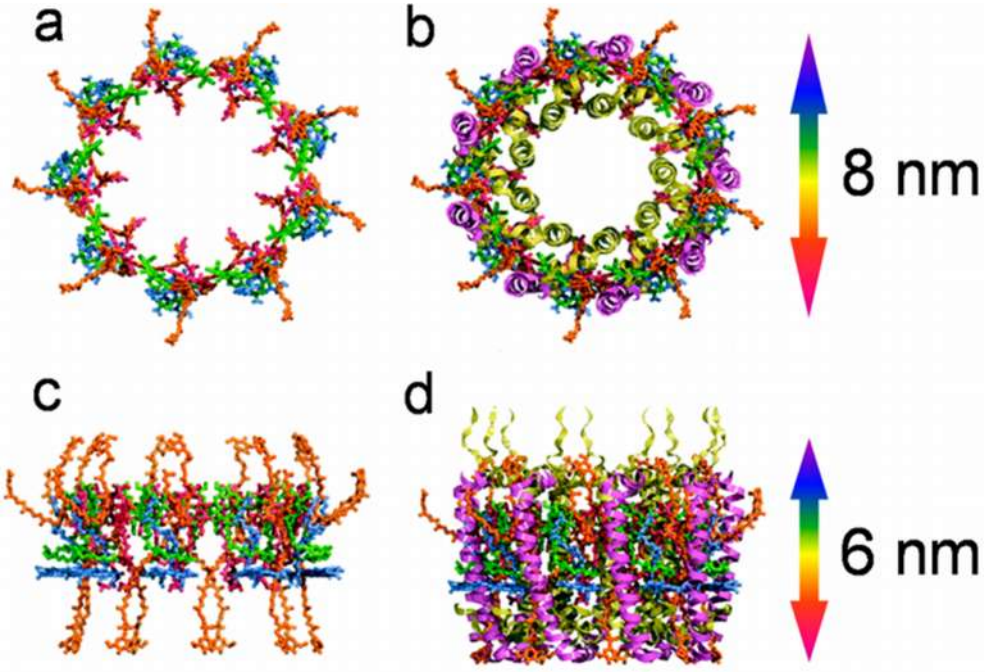

Figure 1.14 Schematically illustration of the B800-850 LH2 complex structure. Reproduced.[80,84]

1.3.3 Protein immobilization

1.3.3.1 Photoactive chemistry

Selective protein immobilization or protein patterning is a process which involves the interaction between active proteins (such as GFP and LHII) and pre-patterned surfaces with protein-resistant regions and protein-attractive regions, which enable proteins to be immobilized at a selective location. Although every surface lithographic technique that has been discussed in previous sections may be used for patterning of such surfaces for protein immobilization, photolithography has been used relatively extensively because of its high in resolution, ease in manipulation and low costs[88]. The types of materials producing proteinresist surfaces are very inclusive, such as poly(ethylene glycol) (PEG) which is the most commonly used nonfouling proteinresist and oligomeric ethylene glycol (OEG) based SAMs[88], nitrophenyl based SAMs [silanes or thiols with o-nitroveratryloxycarbonyl (NVOC), R-methyl-o-nitropiperonyloxycarbonyl (MeNPOC), nitrophenylpropyloxycarbonyl (NPPOC) and 2-nitrophenylethoxycarbonyl (NPEOC) protecting groups)] (Figure 1.15b-e)[90-92], nitrophenyl based polymer brushes [poly(oligoethylene glycol) methacrylate (POEGMA)][93] and arylazide based SAMs [perfluorophenylazide (PFPA) protecting

groups] (figure 1.15a)[89]. These varieties of protein-resistant materials share common properties that enable them to resist the physical absorption of proteins which are hydrophilic, electrically neutral and containing groups that are hydrogen-bond acceptors rather than donors as Whitesides *et al.* described in detail[94]. However, as is shown in figure 1.15, after being exposed to UV irradiation, these protein-resistant materials are all able to be transformed into structures containing active radicals which, in contrast, act as protein-attractive regions.

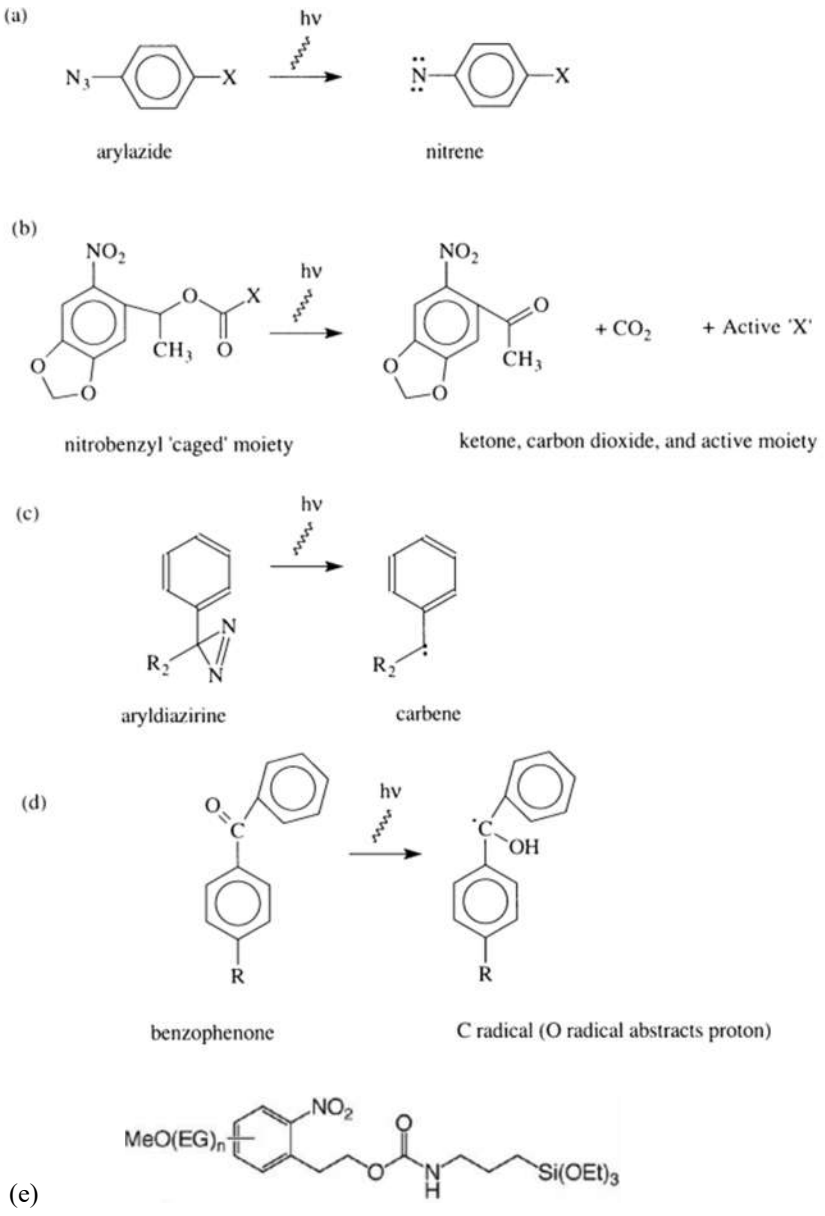

2-nitrophenylethoxycarbonyl (NPEOC)-silane

Figure 1.15 (a) The chemical structure of arylazide and the transformation during UV

irradiation of an arylazide results in an active nitrene which can react with C-H, C-C, C=C, N-H, O-H or S-H bonds. (b) Nitrobenzyl caging format (similar to NVOC) and the chemical transformation upon UV irradiation where a 'caged' moiety results in a ketone, carbon dioxide and the active moiety. (c) Aryldiazirine which after UV irradiation displays an active carbene that can react with C-H, C-C, C=C, N-H, O-H or S-H bonds. (d) Benzophenone upon UV irradiation. A benzophenone forms a biradical and then results in a C-C bond. (e) NPEOC-silane which displays an active $R–NH_2$ group upon photodegradation that can react with the –COOH terminus from proteins.[89,90]

1.3.3.2 Nonspecific attachment

The process by which proteins are immobilized onto the exposed protein-attractive regions consists of two aqueous based dynamic procedures. Whitesides et al. illustrated these procedures in a schematic diagram as was shown in figure 1.16. The key point of this process, although less reported, was believed to be the interaction between aqueous solution and surfaces of proteins and solid substrates. The first procedure involved the interfaces of protein-water and solid substrate-water formed separately before the second procedure where the protein reorganized on absorption. This reorganization might result in modifications of the protein-water interface[94,95].

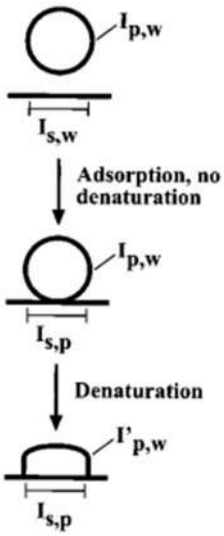

Figure 1.16 Schematic representation of the process proteins absorbed onto surfaces where represented as I: interface, p: proteins, w: water, s: solid.[94]

1.4 Aim of the project

The big goal of our programme is to develop a new field of research, Low-Dimensional Chemistry, which is the manipulation of chemical structure and bonding in a spatially selective fashion at the level of single molecules, the interfacing of molecules with functional elements and the assemble of components into systems. To achieve this goal, top-down (lithographic) methodology and bottom-up (synthetic) techniques are unified to yield control of molecular structure and function across the length scales, from molecular to the macroscopic. To replicate the functionality of the low-dimensional system, the fabrication of multiple-component systems remains the biggest challenge. This thesis will focus on the research of methodology to fabricate multi-component structures. The goal is to achieve the biochips with multi-protein patterns with the size of nanometer scale.

Figure 1.17 shows the chromatophore vesicle from R. sphaeroides (a), which contains the bacterial photosynthetic apparatus, and the mechanism of bacterial photosynthesis (b). Light is captured by light-harvesting complex 2 (LH2) and the energy funnelled to a special chlorophyll-protein complex consisting of light-harvesting complex 1 (LH1) and the photosynthetic reaction centre (RC). The LH1-RC complex contains a metal complex at its heart where ubiquinone (Q) is converted to ubiquinol (QH_2). QH_2 diffuses through the membrane to membrane-bound cytochrome bc_1 complexes, which oxidise QH_2 to Q. During the QH_2 – Q redox cycle, cytochrome bc_1 complexes pump protons across the membrane, leading to a transmembrane proton gradient which drives proton transfer back through ATP synthase, driving the conversion of ADP to ATP.

(a)

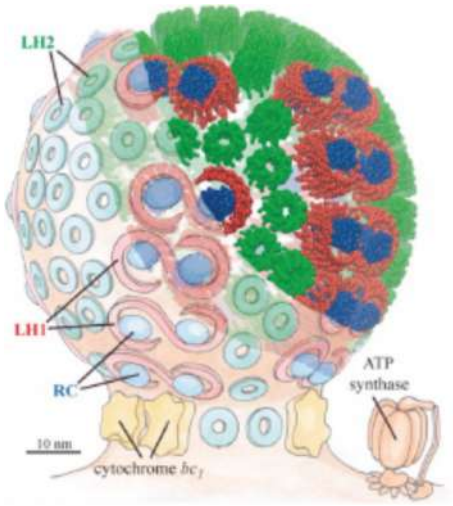

(b)

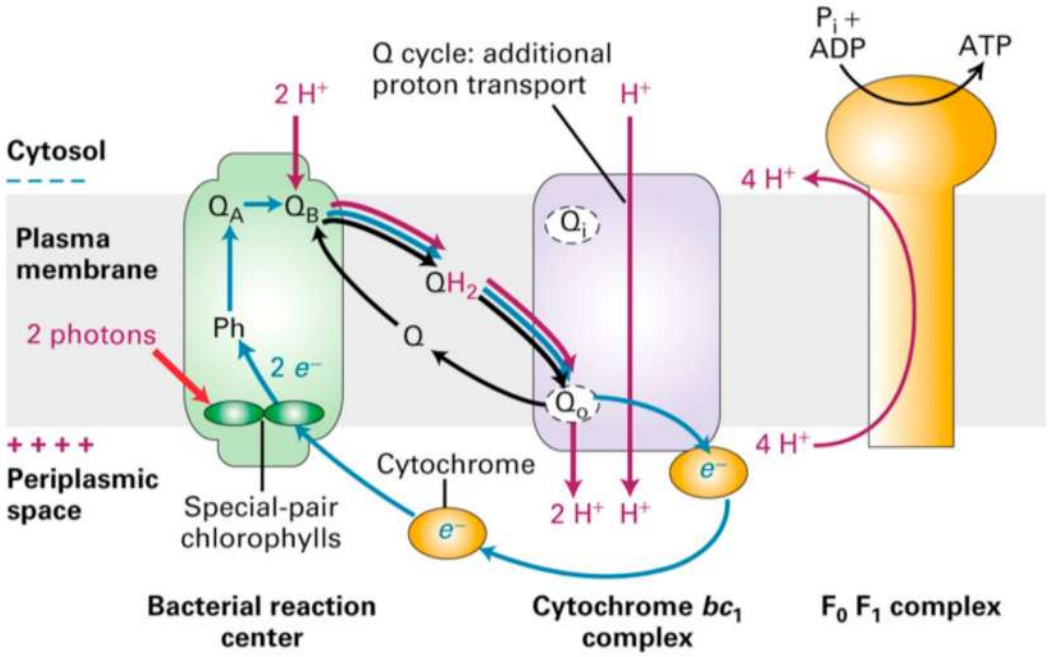

Figure 1.17 (a) The chromatophore vesicle containing the bacterial photosynthetic apparatus from R. sphaeroides[105]. (b) The mechanism of bacterial photosynthesis[106].

In physics, low-dimensional structures are defined to be ones with highly constrained lengths in two or more dimensions. In many senses, the chromatophore vesicle even all biomolecules may be considered to be low-dimensional. Our ambition is to

construct a low-dimensional system that replicates the bacterial photosynthetic apparatus on a chip as shown in Figure 1.18. When irradiated by light, LH2 would transfer the excitation energy through LH1 to RC. QH_2 could be generated during the process and migrate to cytochrome bc_1 by itself, where it would be oxidised back to Q. Concomitantly photons would be pumped across a membrane from the photon-accumulated reservoir to a photon-permeable polymer film that connects with ATP synthase, where ADP could be converted to ATP. Luciferase would consume those ATP and emit luminescence. Each "corral" shown as the box below will be fabricated on the solid substrates from nanostructured polymer brushes. Channels which allow quinones, protons and ATP to diffuse will be built up to connect those "corrals".

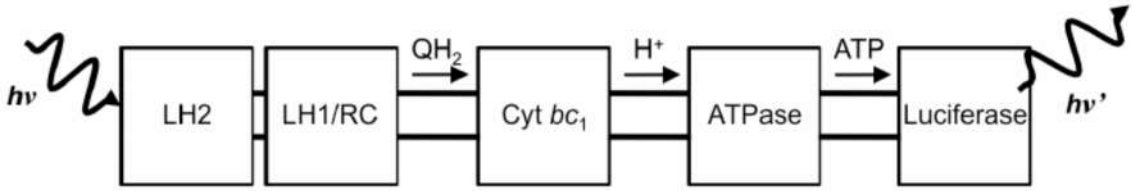

Figure 1.18 Schematic illustration of a low-dimensional system that replicates the bacterial photosynthetic apparatus.

The objectives of the research discussed in this dissertation are the development of methods for fabrication of 1-dimensional protein structures (which is defined as lines narrower than 100 nm in two dimensions in this project) on flat substrates and the integration of molecular nanolines with metallic nanostructures for optical readout and studies of mechanisms of energy migration. These objectives necessitate the development of methods for the formation of functional organic films on flat mica substrates, the utilization of scanning near-field photolithographic and interferometric lithographic approaches to fabricate the desired nanopatterns and the immobilization of light-harvesting proteins on these nanopatterns. The findings of this dissertation are fundamental components of the 'bottom-up' methodology which allow the subsequent fabrication of lipid-bilayer and the immobilization of multiple proteins such as LH1 and LH2.

Chapter 2. Experimental

2.1 Materials

2.1.1 Kinetic study of oligo(ethylene glycol) terminated silane SAMs on mica

2-[Methoxy(polyethyleneoxy)propyl] trichlorosilane (90%) was supplied by Fluorochem. Hydrogen peroxide solution (100 volumes >30%), sulfuric acid (95%), ammonia solution(S. G. 0.88, 35%) were supplied by Fisher Chemical and ethanol (absolute) was supplied by VWR international S.A.S. Sodium dodecyl sulfate (SDS) was supplied by Sigma-Aldrich. Toluene (HPLC grade) was obtained from a Grubbs dry solvent system and de-ionised water was obtained from a Veolia water system (PureLab Ultra, ELGA). Silicon wafers (reclaimed, p-type, <100>) were bought from Compact Technology and mica sheets (25 mm×50 mm) were bought from SPI Supplies Division. A 12 place carousal reaction station was obtained from Radleys Discovery Technologies. Nitrogen gas was supplied by departmental compressed gas system. All the chemicals mentioned above were used as received.

2.1.2 Protein patterning on OEG-NPEOC-APTES films

Oligo (ethylene glycol) (OEG) modified 2-nitrophenylethoxycarbonyl (NPEOC) protected aminopropyltriethoxysilane (OEG-NPEOC-APTES) was synthesized by AF ChemPharm Ltd. Protein GFP and LH2 were supplied by co-worker Dr M. Carton, Department of Molecular Biotechnology, University of Sheffield. Glutaraldehyde solution (Grade Ⅱ, 50% in water), phosphate buffered saline (PBS) and 4-(2-hydroxyethyl)-1-piperazineethanesulfonic acid (HEPES) were bought from Sigma-Aldrich. Hydrogen peroxide solution (100 volumes >30%), sulphuric acid (95%), ammonia solution(S. G. 0.88, 35%) were supplied by Fisher Chemical and ethanol (absolute) was supplied by VWR international S.A.S. Toluene (HPLC grade) was supplied by departmental dry solvent system and de-ionised water was obtained from Veolia water system (PureLab Ultra, ELGA). Nitrogen gas was supplied by departmental compressed gas system. All the chemicals mentioned above were used as received.

2.2 Glassware cleaning and substrate handling

All the glassware which was in direct contact with substrate and reagents was washed by piranha solution. Piranha solution is a mixture of 95% sulfuric acid solution and 30% hydrogen peroxide solution in the ratio of 3:1 and is commonly used to remove organic residue because of its strong oxidizing property. Extreme caution should be exercised when preparing and using piranha solution since it is both strongly acidic and strongly oxidizing and may detonate on contact with organic materials. After the glassware was washed in piranha solution it was washed repeatedly by rinsing with deionised water and dried in an oven.

Silicon wafers and mica sheets were cut to suitable size to fit the sample preparation tubes and for subsequent experiments. They were placed in tubes separately, cleaned by ultra-sonication in sodium dodecyl sulphate (SDS) solution (ca. 1mM) for 15 mins and then rinsed with de-ionised water 3 times. Tubes were filled with piranha solution and left for 1 to 3 h. After rinsing with copious amount of de-ionised water, the glass containers were placed on a hot plate and filled with RCA solution (a mixture of hydrogen peroxide, ammonia solution and de-ionised water (1:1:5)) for 30 min. Tubes and samples were rinsed 3 times with de-ionised water. Finally, they were dried in an oven overnight at 120ºC. Mica substrates were prepared by cutting mica sheets to size using scissors and cleaving them to expose a clean surface.

2.3 SAM preparation

Silicon wafers and mica sheets were cut into 1.5 cm×3.0 cm pieces. One corner of each sample was cut off to enable the two sides to be differentiated. Substrates were placed in the tubes in the carousel reaction station under a nitrogen atmosphere before injecting the solution of 2-[methoxy(polyethyleneoxy)propyl] trichlorosilane (in different concentrations) in toluene. It was essential that the substrates were immersed in the solution entirely and the whole station was covered by aluminium foil to prevent any possible contact with UV light since this OEG-terminated silane used here was photo sensitive. Reaction time varied from 30min to 72h. Prepared samples were washed by toluene three times from a wash bottle, then ultrasonically cleaned (5 min) and dried using nitrogen gas. All samples were placed in clean sealed tubes and

annealed in the vacuum oven for 1 h at 120ºC. Tubes were covered by foil during all procedures.

Mica sheets were immersed in 1 mM OEG-NPEOC-APTES toluene solution for 24 h and were washed by rinsing with toluene 3 times before being ultrasonically cleaned for 5 min. The samples were blown dry under a nitrogen gas stream. All samples were placed in clean sealed tubes and annealed in the vacuum oven for 1h at 120ºC. Samples were wrapped in foil to prevent exposure to light.

2.4 NPEOC transformation under exposure to X-ray

Five annealed NPEOC samples were sent to XPS analysis. Only the element of nitrogen was analysed during the close scan which took 400 seconds each and every sample was scanned for 6 times.

2.5 Protein patterning through UV photolithography

For micro patterns, samples were covered by a copper mask (1000, 1500 or 2000 mesh squared grids) (Agar, Cambridge, UK), then by a transparent clean quartz disk in order to keep the mask in position during subsequent manipulation, and finally exposed to a 244 nm wavelength UV laser beam from a Coherent Innova 300C frequency doubled argon ion laser. The laser intensity was varied between 10-100 mW and had a diameter approximately 2-3 mm. Samples were washed and ultrasonically cleaned in PBS solution before being immersed in glutaraldehyde (25% v/v) (GA) water solution. Finally, samples were incubated in a solution of GFP in PBS buffer overnight. Samples were rinsed with PBS buffer solution 3 times and stored by immersion in PBS buffer solution in a fridge (4 ºC) prior to further experiments. All the operations were carried out in a dark room. Schematic representations of preparation procedures are as follows:

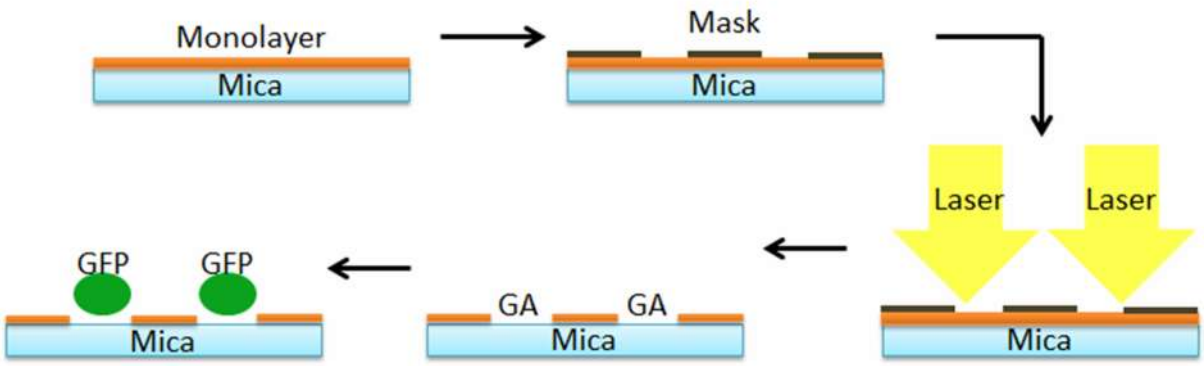

Figure 2.1 Schematic representations of the manipulation procedures of fabricating a micron scale pattern using a mask.

Nanoscale patterning utilizing a Witec AlphaSNOM coupled to a HeCd laser (325nm). Cantilever probe with hollow pyramidal tips were used. An aperture was formed at the apex of the tip (figure 2.2b). The diameter of the aperture was ca. 170 nm. Laser light was transformed along an optical fibre and focused by a 0.2 numerical aperture lens onto the topside of the aperture in the probe. Feedback was achieved by using optical defection from the backside of the cantilever holding the probe, as shown in figure 2.2 (a). The reflected signal was measured by a photodetector, enabling control of the tip weight, ensuring that the sample remained at all times within the near field of the probe.

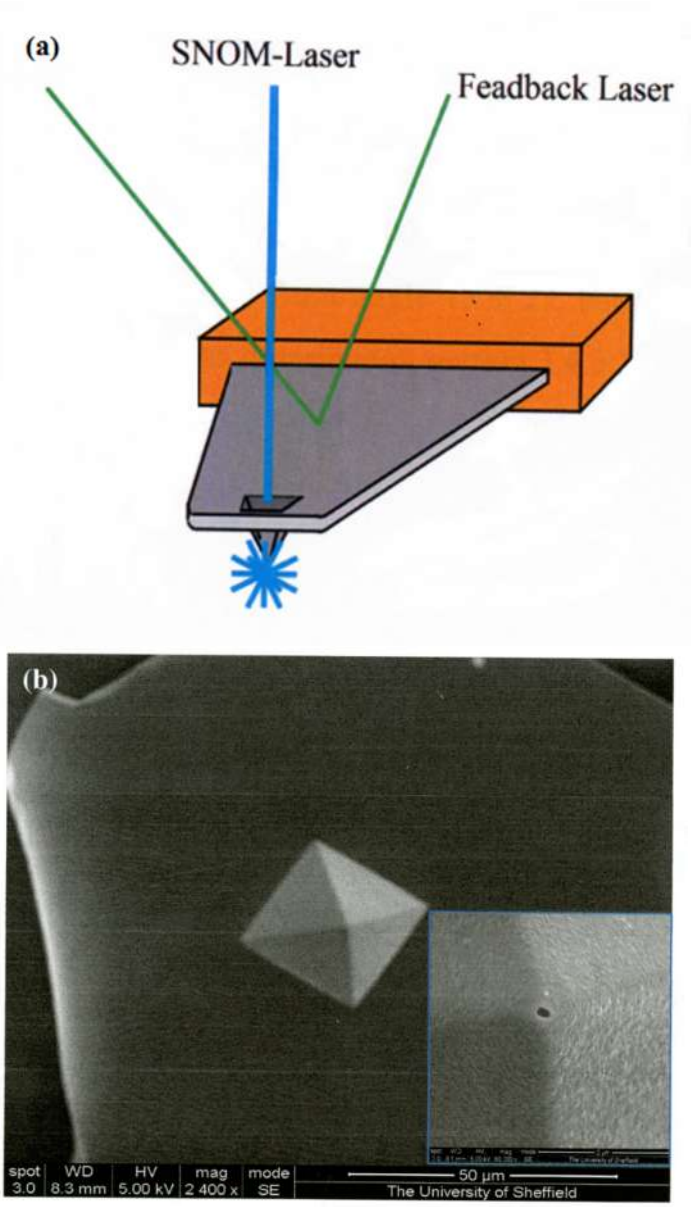

Figure 2.2 (a) The experimental setting of a SNOM probe and detector. (b) A picture of the hollow aperture of a SNOM probe. The smaller image in the right down corner was taken by zooming in on the apex area of the probe.[104]

IL was carried out using a Lloyd's mirror interferometer coupled to the frequency doubled argon ion laser. The beam was defocused to cover ca. 1 cm^2. Protein adsorption was carried out by immersing the samples in a solution of the protein in the appropriate buffer. PBS was used for GFP, while Hepes buffer was used for LH2.

2.6 Surface analysis techniques

2.6.1 Contact angle measurement

The scientific study of contact angles and wettability began with the work of Thomas Young *et al.* [96] in 1805. Since then, the phenomenon has been studied both mathematically and chemically and the utilization of contact angles in estimating surface tensions spread rapidly. A representative model of contact angle measurement is shown in figure 2.3 where a liquid droplet is placed on a homogeneous flat solid surface. The extent of the spreading and the area of the resulting solid-liquid interface is determined by the relationship of γ_{SV}, γ_{SL} and γ_{LV} , the surface free energies of the solid-vapour, solid-liquid and liquid-vapour interfaces, respectively. The cosine of the contact angle θ between the liquid and the solid surface obeys the Young's equation:

$$\cos\theta = \frac{\gamma_{SV} - \gamma_{SL}}{\gamma_{LV}} \qquad (2.1)$$

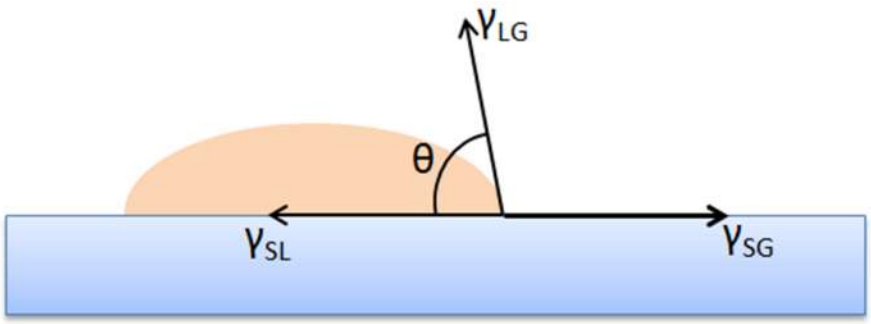

Figure 2.3 Schematically representations of the definition of contact angle.

Theoretically, when the water contact angle is greater than 90˚, it means that the surface is hydrophobic, while when the contact angle is less than 90˚, surface is regarded as a hydrophilic as shown in figure 2.4.

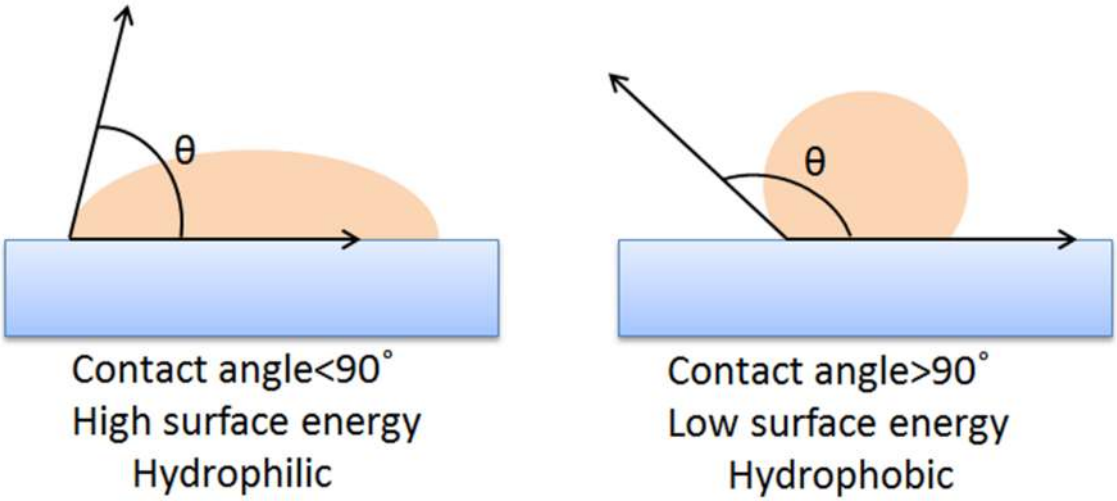

Figure 2.4 Comparison of the contact angles of hydrophobic and hydrophilic surfaces.

J. Bico *et al.* [97] studied the influence of the roughness of homogeneous surfaces on contact angle data. Their research revealed that it was the fraction of the solid actually in contact with the liquid not the roughness itself that determined the contact angle of the surface, because the existence of air particles in the cracks of rough surfaces could decrease the proportion of solid in contact with liquid making the surface hydrophilic. Consequently, by utilizing a smooth but microscopic spiked surface, extremely high contact angles of approximately 180˚ were obtained, described as 'pearl drops' (figure 2.5).

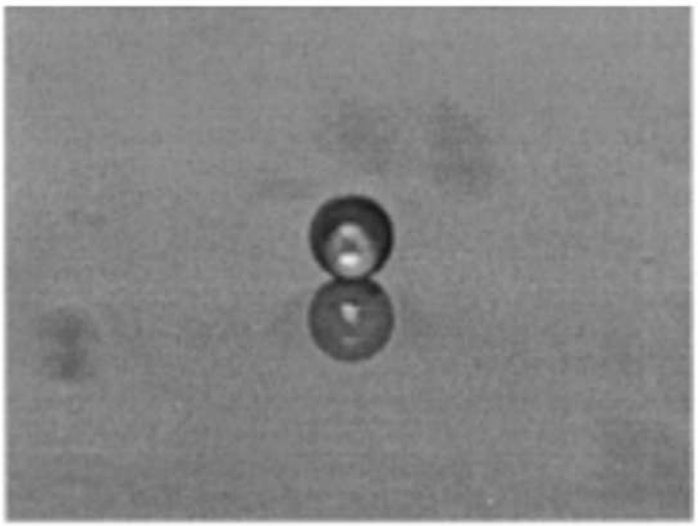

Figure 2.5 Pearl drops on smooth but microscopic spiked surface.[97]

Contact angles were measured using a Rame-Hart goniometer with a static sessile drop system. A drop of liquid (pure water in this project and the volume of each drop is about 2 μL) at the end of the syringe was lowered onto the surface until it contacted with the sample and the profile of the water droplet was observed through a goniometer after it had come to equilibria. Five measurements were taken and recorded in different spots of the same sample and the mean of these measurements was quoted for each sample.

2.6.2 Ellipsometry

The technique of ellipsometer was first coined by A. Rothen[100] in 1945 to describe an optical instrument for the measurement of thin films on solid surface by the reflection of polarized light. As is shown in Figure 2.6, the setup of a null ellipsometer includes a light source, a rotatable polarizer, a quarter wave compensator, a rotatable analyser and a detector. A light beam emits from the light source falls down onto the sample surface in a degree (θ) after the rotation of polarizer and compensator and passes through the analyser to be analysed and finally reaches the detector. The basic principle of ellipsometric measurement is not only to measure the different state of polarization of incidence (i) and reflection (r) vector wave, but by measuring the state of polarization to obtain certain information for further analysis[98]. For example, given the orientation of the azimuth angles of the polarizer (P), compensator (C) and analyser (A) around the beam axis in Figure 2.6 and by analysing the shift of the vector wave upon the reflection on sample surface, the thickness (d) (Figure 2.7) of the thin film on solid surface can be obtained via following equations

$$\rho = \frac{\gamma_p}{\gamma_s} = \tan\psi \cdot e^{i\Delta} \qquad (2.2)$$

$$\rho = -\tan A\left[\frac{\tan C + \rho_C \tan(P-C)}{1-\rho_C \tan(P-C)}\right] \qquad (2.3)$$

$$\beta = \frac{2\pi d}{\lambda} N_1 \cos\phi_1 \qquad (2.4)$$

where ρ stands for the ratio between reflection coefficients of the light polarized parallel (p) and the perpendicular (s) to the plane of the incidence. The ratio of γ_p and γ_s are affected by the values of amplitude component ψ and the phase shift Δ.

Meanwhile, the amplitude transmittance of compensator ρ_C is known. β is the thickness of phase 1, N denotes the refraction index of phases 1 and 2 and ϕ_1 is as shown in Figure 2.7[98,99]. In order to calculate the thickness (d) on the substrate, refraction properties and model are required, such as the refraction index of each sublayer in the film, dielectric function tensor and thickness coefficients.

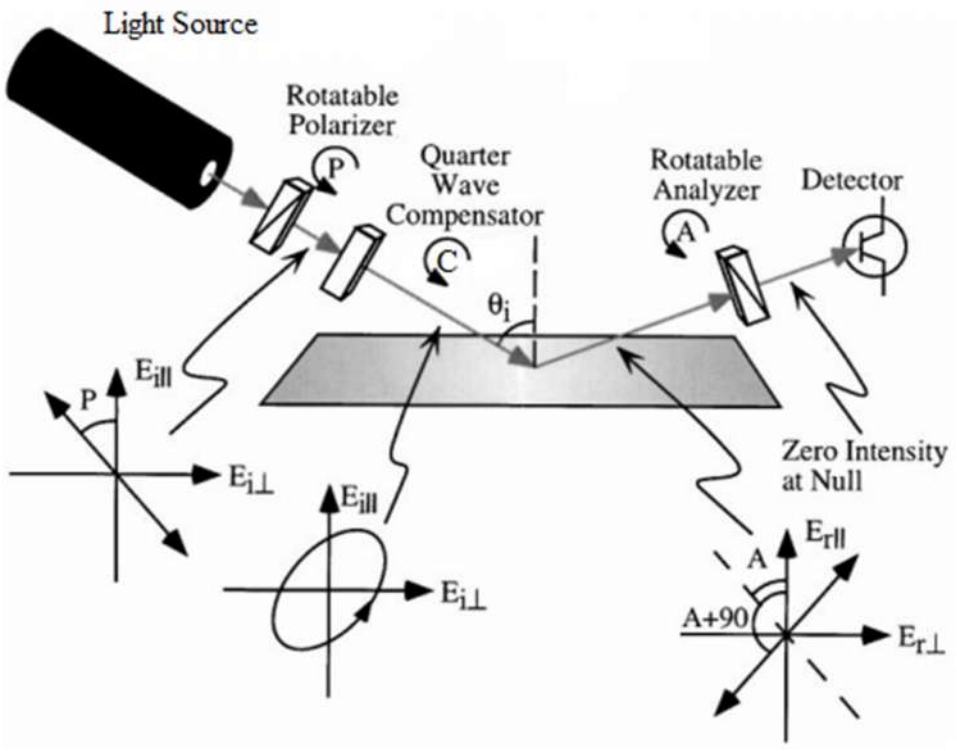

Figure 2.6 Schematically representations of the arrangement of polarizer compensator sample analyser null ellipsometer.[99]

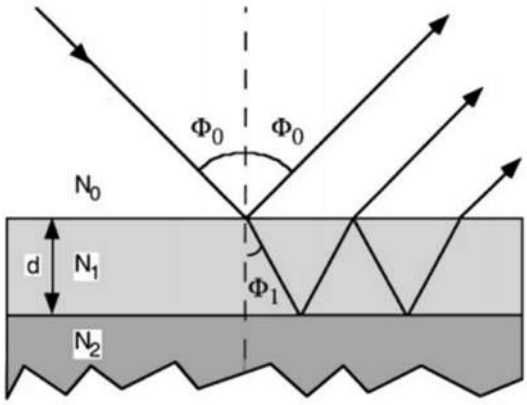

Figure 2.7 A profile schematically representations of the refraction of light beam

inside the thin film on solid surface (N_{012} stands for the refraction indexes of phase air, thin film and substrate, respectively).[99]

The ellipsometer used in this project was an M-2000 ellipsometer (J. A. Woollam Co. Inc). As the measurement of ellipsometry requires reflection light from the sample surface, mica which is a diaphanous material is not suitable for use. Thus, silicon wafer was chosen as the substrate for all the samples requiring ellipsometric thickness measurement. Two types of samples were studied, namely an OEG-terminated silane monolayer on the native oxide layer of a silicon wafer, and a protein layer on OEG-NPEOC-APTES formed on the native oxide of Si. The former was analysed using a Cauchy layer model coupled to the model for native oxide layer while the latter was analysed by the combination of models B-Spline, Cauchy and native oxide. Five spots were measured for each sample and the average value of these five measurements was recorded as the thickness of the thin film.

2.6.3 Confocal laser scanning microscopy

The confocal laser scanning microscope was invented by M. Minsky in 1955 when the instrument was called a 'double-focussing stage-scanning microscope' instead of 'confocal microscope'[102]. However, his invention was unappreciated in the following thirty years until the appearance of modern confocal microscope which caught on with its ability of 2D and 3D high resolution imaging not only in inorganic materials but also *in vivo*[101].

Confocal laser scanning microscopy is utilized to obtain high resolution fluorescent images in a selected plane of a sample by focussing the laser beam emitted from the light source on the imaging plane by a series of optical units. As is shown in Figure 2.8 (a), a laser beam (yellow) reflected by a beam splitting mirror falls through an objective where the laser is focussed onto the selected plane. The reflected laser beam from the specimen (blue) passes through the objective again and is focussed into a pinhole aperture where the laser reaches the detector. Meanwhile, in 3D imaging, the filter around the pinhole aperture blocks most other reflected light from illuminated specimen above (red in Figure 2.8b) and beneath (orange) the plane of interest. A rotatable pinning disk with a number of pinholes on it is also addable to the system to speed up the scanning process (Figure 2.8c). Either way, the laser beam needs to move

from point to point until the image of the entire plane is acquired[101].

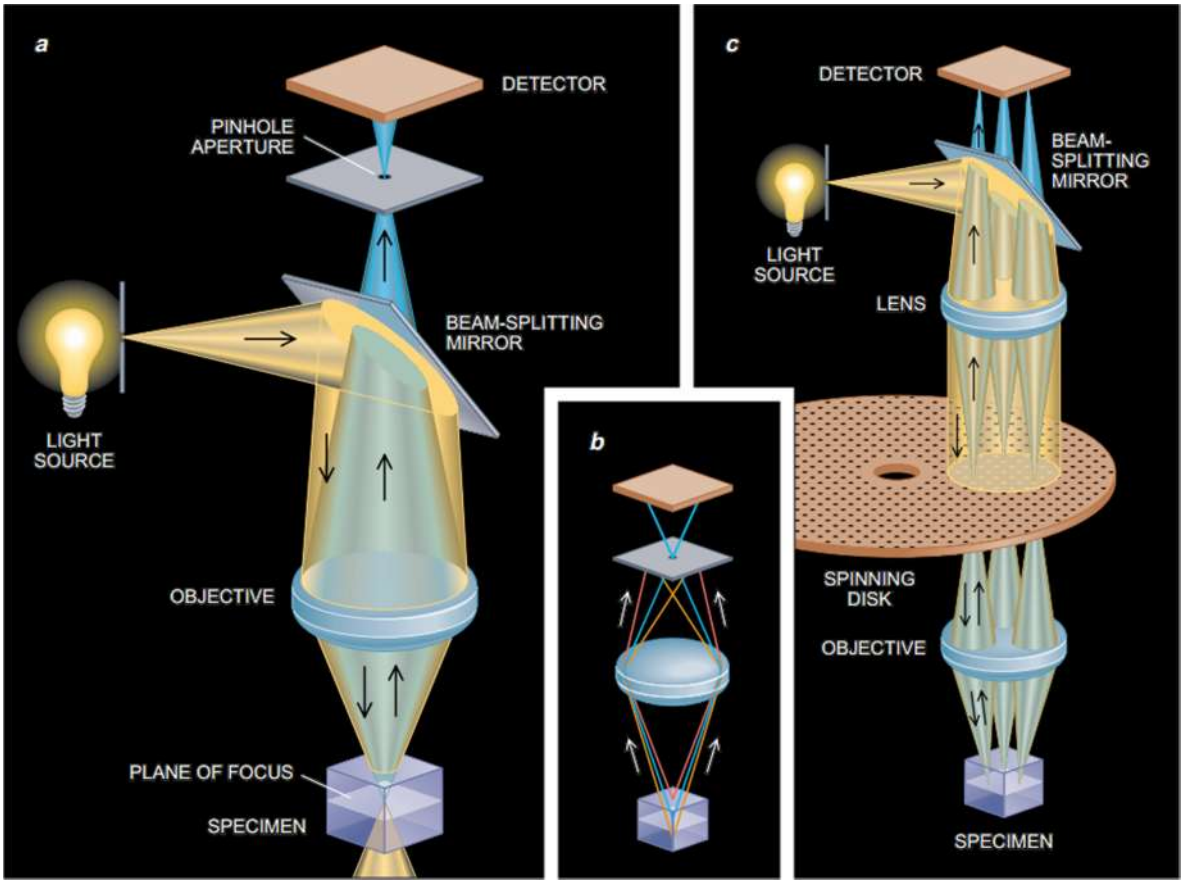

Figure 2.8 The optical arrangement of confocal laser scanning microscope.[101]

The principle of fluorescence emission from fluorophores on the specimen which is acquired by confocal is quite simple (figure 2.9). By absorption of incident light energy, electrons in the fluorophores are promoted from a stable lower state (S_0) to a higher excited state (S_1), and the absorbed energy is used to move to another singlet state (S_2) via intersystem crossing where electrons have the lowest vibration energy of their excited state. Finally, the fluorophore returns to S_0 again by emitting a photon. The emitted photons are acquired by confocal microscope detector and form the fluorescent images of the plane of interest.

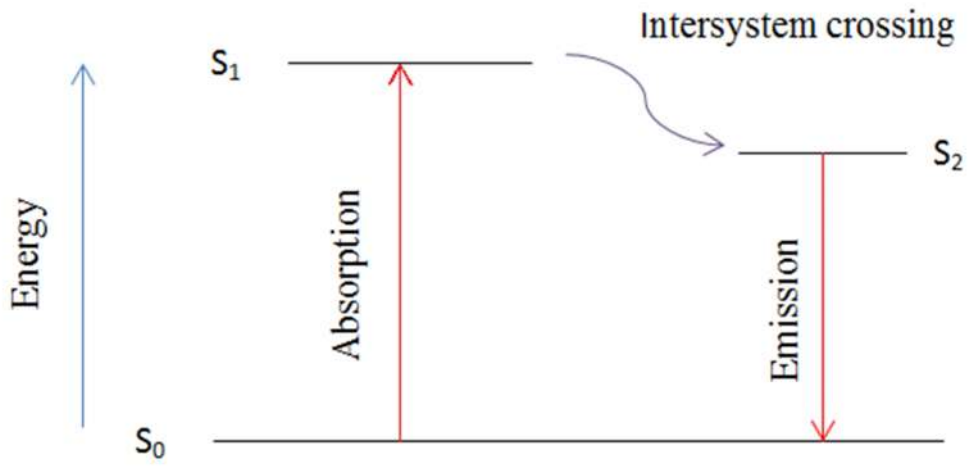

Figure 2.9 The principle of fluorescence emission.

All the imaging was carried out by a LSM 510 meta laser scanning confocal microscope (Carl Zeiss, Welwyn Garden City, UK).

2.6.4 X-ray photoelectron spectroscopy

X-ray photoelectron spectroscopy (XPS) is a quantitative surface spectroscopic technique. It is based on the photoelectric effect discovered by Hertz in 1880s. When a sample is irradiated by X-ray, photoelectrons are ejected with characteristic kinetic energies. Detection of these core shell electrons enables the composition and chemical structure of the surface to be determined. Samples to be analysed are placed in the ultra-high vacuum (UHV) analysis chamber in order to reduce contamination from adsorption of residual gas molecules and to ensure the samples electrons reach the detector without being scattered. High energy electrons from a heated filament are directed onto a metallic target (the anode) to produce X-rays. Typically, aluminium and magnesium are used as the anode materials. The X-ray penetrates several microns into the sample surface, but scattering causes most of the signal to be attenuated and the photoelectrons that are detected originate from the top few nanometres of the sample.

Energy conservation during the photoemission leads to the Einstein equation

$$E_B^F = h\nu - E_K - \phi_{sp} \qquad (2.5)$$

where E_B^F is the binding energy of the Fermi level (figure 2.10), E_K is the kinetic

energy acquired by the analyser, $h\nu$ is the energy of the exciting X-ray photon and ϕ_{sp} is the work function of the spectrometer (about 5 eV). Equation (2.5) assumes an elastic photoemission process which means that there is no energy loss during the transportation through the solid surface for photoemission. Hence, there will be a unique photoelectron spectrum for each photon energy that X-ray source can provide[105,107].

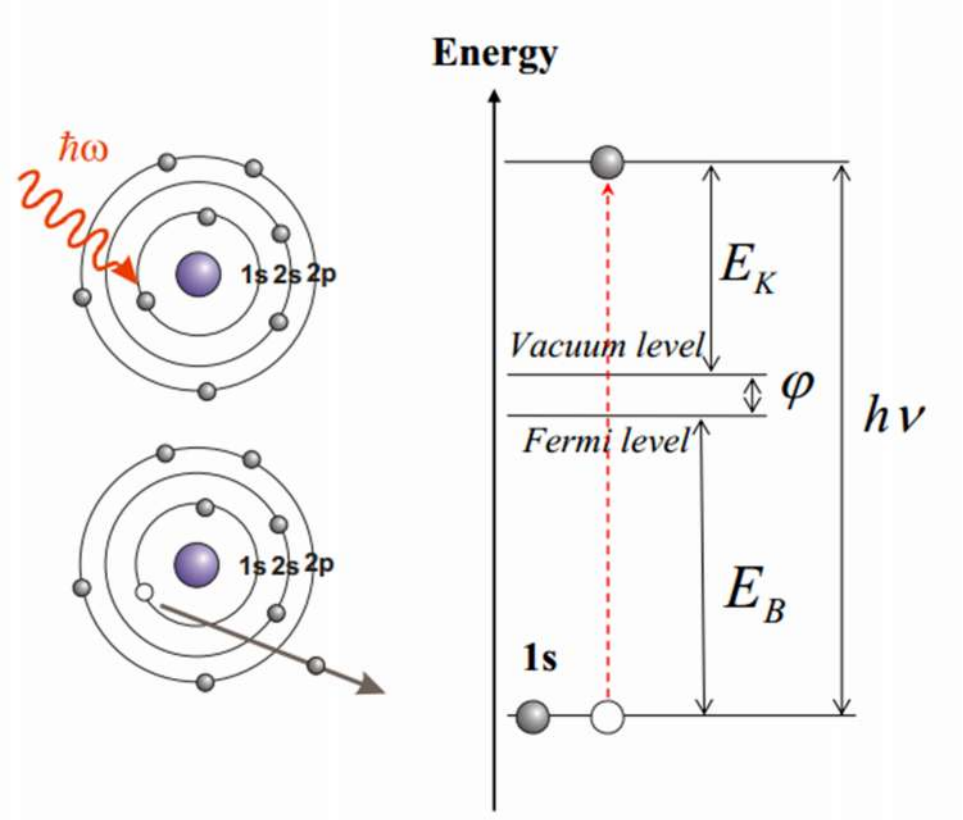

Figure 2.10 Schematically representations the process and energy conservation of photoemission.[106]

When the original state of the element is changed, for instance, by the formation of chemical bond with other atoms, the binding energy will be changed and this will be observed in the spectrum (see figure 2.11). This phenomenon is called the "chemical shift". By analysing the chemical shift, the structure of a specific element in a function group up to the whole molecule can be predicted.

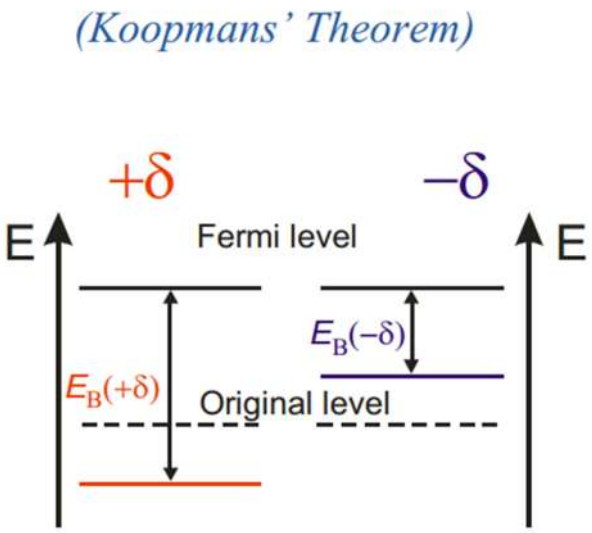

Figure 2.11 Schematically representations of the cause of chemical shift from ref 106.

Quantitative analysis is achieved by calculating the peak areas of elements in spectra. Several factors are considered in the calculation such as the background subtraction, relative sensitively factors and roughness factor etc.

2.6.5 Atomic force microscopy (AFM)

Atomic force microscopy (AFM), which was inspired by the technique of scanning tunnelling microscopy (STM) was invented by Binning *et al.* in 1986 [108]. In the AFM, a sharp tip attached to a flexible cantilever is scanned across the sample. As is shown in figure 2.12, the cantilever is suspended from a piezoelectric crystal with a low spring constant that may be moved up and down depending on the mode operation. Variation in the force acting on the tip causes variation in the interaction force on the cantilever. The cantilever may be treated as a Hookean spring, for which F = -kx. The deflection of a laser beam reflected off the back of the cantilever is detected and processed.[104]

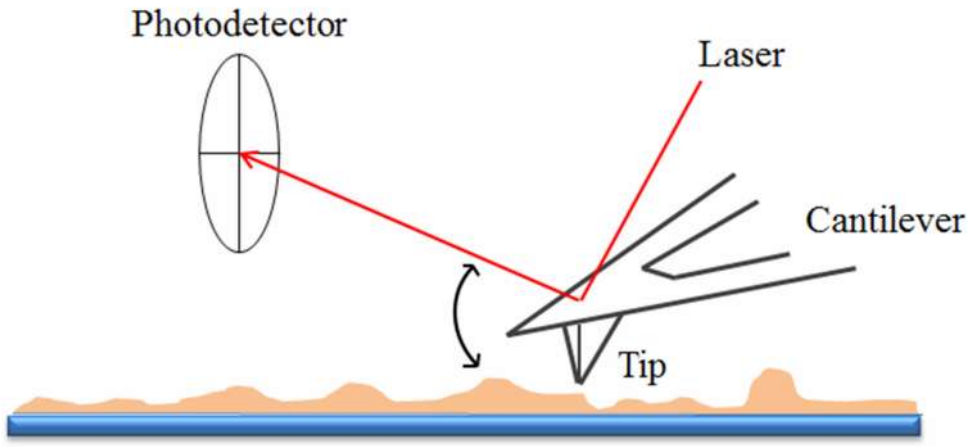

Figure 2.12 The basic principle of AFM.

2.6.5.1 Contact mode

In contact mode where repulsive interaction dominates the movement of AFM probe, the tip actually touches the sample surface. The tip scans smoothly across the uneven surface with extreme topographical changes and the topographical changes are revealed by the deflection of the cantilever. There are two strategies to carry out the scanning, namely constant height and constant force. When height is constant, it means that the cantilever never raised or lowered during the entire process. It is only the interaction forces vary with the changes of topography and AFM measures the forces. When the force is constant, the cantilever adjusts to the topography moving up and down to ensure the constant interaction force between tip and the surface and AFM records the movements. Hooke's law is used in order to produce an image:

$$F = -kx \qquad (2.6)$$

where the force F is determined by the deflection amount (x) and the force coefficient of the cantilever (k) [111,112].

Additionally, contaminants such as absorbed water layer and dusts in the air at the sample surface can result in a considerable influence on the condition of the tip-surface interaction, which leads to the exploration of scanning operation under liquids. Even though distinct results were observed using liquids circumstance for AFM measurement, problems accompany the advantages. For instance, the ions absorb onto the sample surface and the dielectric forces of the tip changes with different

polarisation force of each solvent [110].

2.6.5.2 Tapping mode

In tapping mode which was developed by Zhong *et al.* in 1993 [113] for the particular usage on soft surfaces, the tip also contacts the sample surface, but the contact is extremely short. In this fashion, lateral forces and damage on soft surfaces are reduced dramatically. The principle of tapping mode is to modulate the cantilever at its resonance frequency (hundreds of kHz) which enables a short tip-surface contact in each oscillation cycle. The amplitude and phase data are recorded and used to generate images. If the amplitude is constant during one scan, the z-piezo is adjusted to achieve high contrast of features on the scanned regions. However, when acquiring the phase images, it is the energy dissipation of the interaction forces caused by the lag between the driving force of the oscillation and the cantilever resonance that is measured by the AFM. During the phase imaging, the mechanical properties of the sample surface can be revealed. Meanwhile, the topographical image is generated with the feedback data of the cantilever deflection.

Chapter 3. The formation of self-assembled monolayers of oligo(ethylene glycol) terminated silanes on mica

3.1 Introduction

Much research has been carried out studying the protein resistance of self-assembled films formed by the adsorption of Oligo(ethylene glycol) (OEG) terminated thiols on different substrates (gold, titanium, copper and some other metals) since 1990s [118,119]. These films have attached growing interest for a wide variety of applications in biology, including analytical devices for medical diagnostics[114] and biomedical processing[117] which requires minimal bio-contamination. The mechanism of protein resistance of poly(ethylene glycol) (PEG) and related materials such as OEG terminated monolayers has been studied. Although many aspects are still disputed, it is now widely accepted that the binding of water to the ether groups plays an important role in preventing protein adsorption[115,116].

Early work on OEG terminated SAMs of alkyl thiolates was followed by studies demonstrating the protein resistance of films of OEG terminated alkyl trichlorosianles.[117] Because the protein resistance of an OEG functionalized surface depends upon molecular packing, the mechanism of formation of OEG terminated SAM was studied. Figure 3.1 shows schematically the generally accepted, stepwise mechanism of film formation. In figure 3.1, water from the atmosphere hydrates the silica surface. The silanol groups produced in this process react with the chlorine atoms on the head group of the adsorbate. Dehydration occurs forming a Si-O bond that joins the adsorbate to the surface, releasing hydrogen chloride as a by-product. The remaining Si-Cl bonds undergo reaction in a similar way. Finally, OEG silanes undergo hydrolysis to cross link with each other. At this point a densely packed and ordered monolayer of OEG terminated silane is formed. If the substrate is removed from the solution of the adsorbates before this moment, the reaction is incomplete, and the surface density will be lower. As the coverage increases, isolated adsorbates form islands and then, as monolayer coverage is approached, the roughness decreases.

However, if the sample is immersed for too long, polymerization will happen among OEG silanes, increasing the surface roughness. Hence, in order to produce a defect-free, densely packed and well-ordered SAM with OEG terminated silane, the control of preparation time is the key factor.

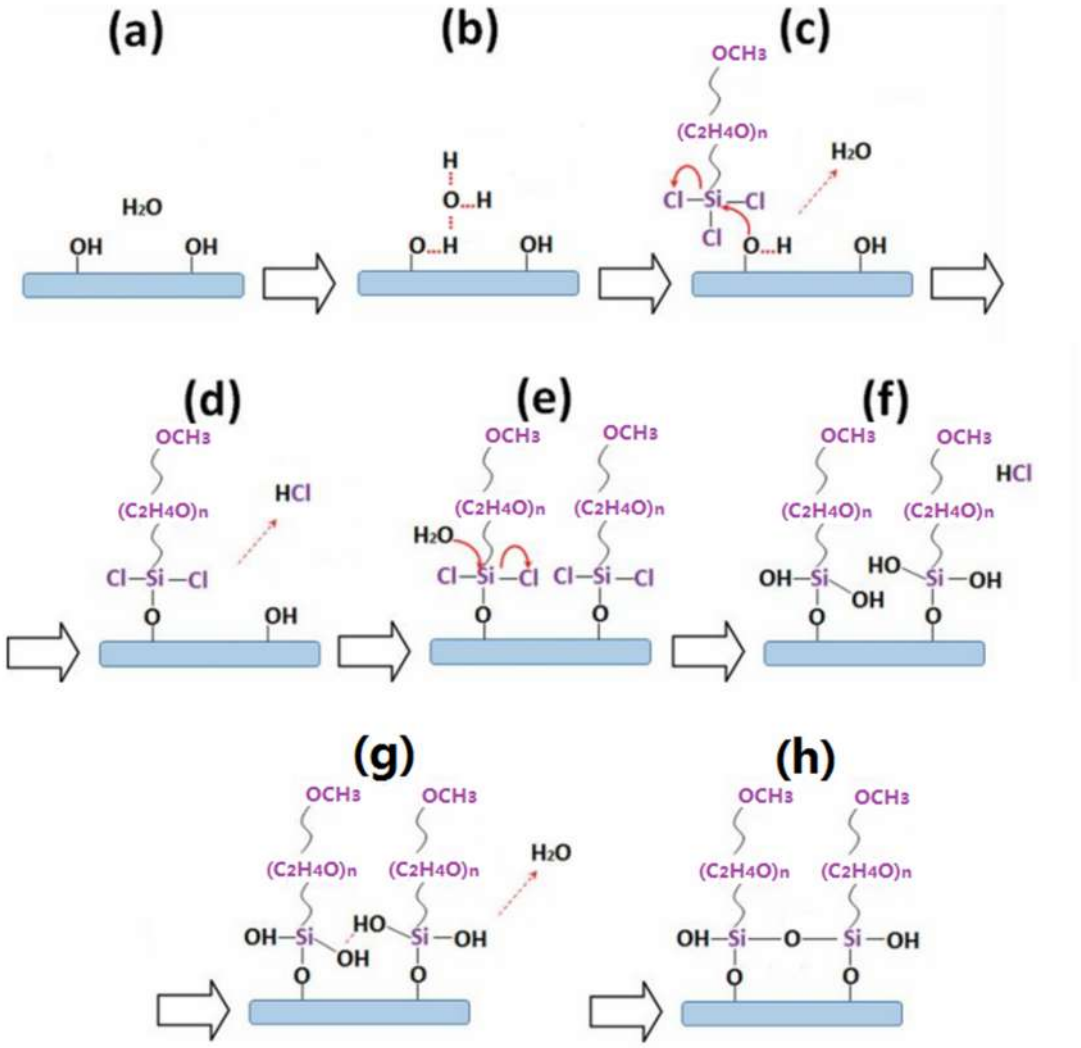

Figure 3.1 Schematic illustration of a most acceptable mechanism of the formation of OEG terminated trichlorosilanes SAM.

In this chapter, mica was compared with silicon as a substrate for monolayer formation, because of its low roughness making it suitable for AFM study. Both substrates was used to form SAMs with 2-[methoxy(polyethyleneoxy)propyl] trichlorosilanes (OEG terminated trichlorosilane) (1% v/v). Water contact angles, ellipsometric thickness, AFM roughness measurements and AFM height images, and

XPS spectra were obtained to enable the detailed characterisation of these SAMs on mica. Kinetic experiments were performed by varying the preparation time of each specimen, to enable determination of the optimum immersion time to yield high quality monolayers of 2-[methoxy(polyethyleneoxy)propyl] trichlorosilane (OEG silane).

3.2 Experimental

2-[Methoxy(polyethyleneoxy)propyl] trichlorosilane (90%) was supplied by Fluorochem. Hydrogen peroxide solution (100 volumes >30%), sulfuric acid (95%), ammonia solution (S. G. 0.88, 35%) were supplied by Fisher Chemical and ethanol (absolute) was supplied by VWR international S.A.S. Sodium dodecyl sulfate (SDS) was supplied by Sigma-Aldrich. Toluene (HPLC grade) was obtained from a Grubbs dry solvent system and de-ionised water was obtained from a Veolia water system (PureLab Ultra, ELGA). Silicon wafers (reclaimed, p-type, <100>) were bought from Compact Technology and mica sheets (25 mm×50 mm) were bought from SPI Supplies Division. A 12 place carousal reaction station was obtained from Radleys Discovery Technologies. Nitrogen gas was supplied by departmental compressed gas system. All the chemicals mentioned above were used as received.

Silicon wafers and mica sheets were cut into 1.5 cm×3.0 cm pieces. One corner of each sample was cut off to enable the two sides to be differentiated. Substrates were placed in the tubes in the carousel reaction station under a nitrogen atmosphere before injecting the solution of 2-[methoxy(polyethyleneoxy)propyl] trichlorosilane (OEG silane) (1% v/v) in toluene. It was essential that the substrates were immersed in the solution entirely and the whole station was covered by aluminium foil to prevent any possible exposed to UV light since this OEG-terminated silane used here was photo sensitive. Reaction time varied from 30min to 72h. Prepared samples were washed by toluene three times from a wash bottle, then ultrasonically cleaned and dried using nitrogen gas. All samples were placed in piranha level clean sealed tubes and annealed in the vacuum oven for at 120ºC. Tubes were covered by foil during all procedures.

Water contact angles were measured using a Rame-Hart goniometer with a static sessile drop system where pure water was used in this project and the volume of each droplet was about 2 μL. AFM height imaging and roughness measurements were carried out using a Digital Instruments Multimode Nanoscope IV (Veeco Instruments, Cambridge, UK) atomic force microscope in contact mode. In order to determine the optimum preparation time of OEG silane for a smoother surface on silicon and mica substrates, both of these techniques were utilized to reveal the topography and

smoothness of the samples. The ellipsometer used in this project was an M-2000 ellipsometer (J. A. Woollam Co. Inc). As the measurement of ellipsometry requires reflection light from the sample surface, mica which is a diaphanous material is not suitable for use. Thus, silicon wafer was chosen as the substrate for all the samples requiring ellipsometric thickness measurement. The ellipsometric measurement results were obtained to compare with the AFM imaging and contact angle results, to ensure they were in good agreement. Axis Ultra DLD X-ray photoelectron spectrometer (Kratos Analytical, Manchester, UK) was employed to achieve XPS spectra and the spectra were analysed via CasaXPS program (Casa, http://www.casaxps.com, UK). XPS C1s spectra on both substrates were used to confirm the formation of OEG silane SAM on the sample surfaces.

3.3 Results and discussion

3.3.1 Contact angle measurements

Figure 3.2 shows the variation in the contact angles of films formed by the adsorption of OEG-silane on silicon wafer substrates as a function of the preparation time. Both original clean substrates were very hydrophilic that yielded water contact angles were close to zero. Thus, the increase in contact angle of the samples after immersion in the silane solution can be attributed to the reaction between the adsorbates and the substrate. The contact angle reached 39° after 30 min, increasing more slowly to reach 58° after 2 h. After long immersion times, a small increase in the contact angle was observed, but the rate of increase slowed and a limiting value of 60° was reached after 72 h. Figure 3.3 shows the variation in the contact angle of OEG silane SAM on mica as a function of the immersion time. After 30 min, the contact angle for the film formed on mica was 27° compared to 39° on silicon, and generally showed lower values than those on silicon substrate. The limiting value was 55° after 72 h. Some tendencies can be seen from these diagrams. The contact angle values are positive correlated with the preparation times in trend, but, on both substrates, values decrease slightly at around 3.5 h to 4.5 h. The contact angle seems to approach a limiting value after ca. 2 h, which could correspond to monolayer formation. At longer times, the contact angle increases again, probably due to polymerization of the adsorbates leading to the formation of a rougher particulate layer that causes an increase in the contact angle.

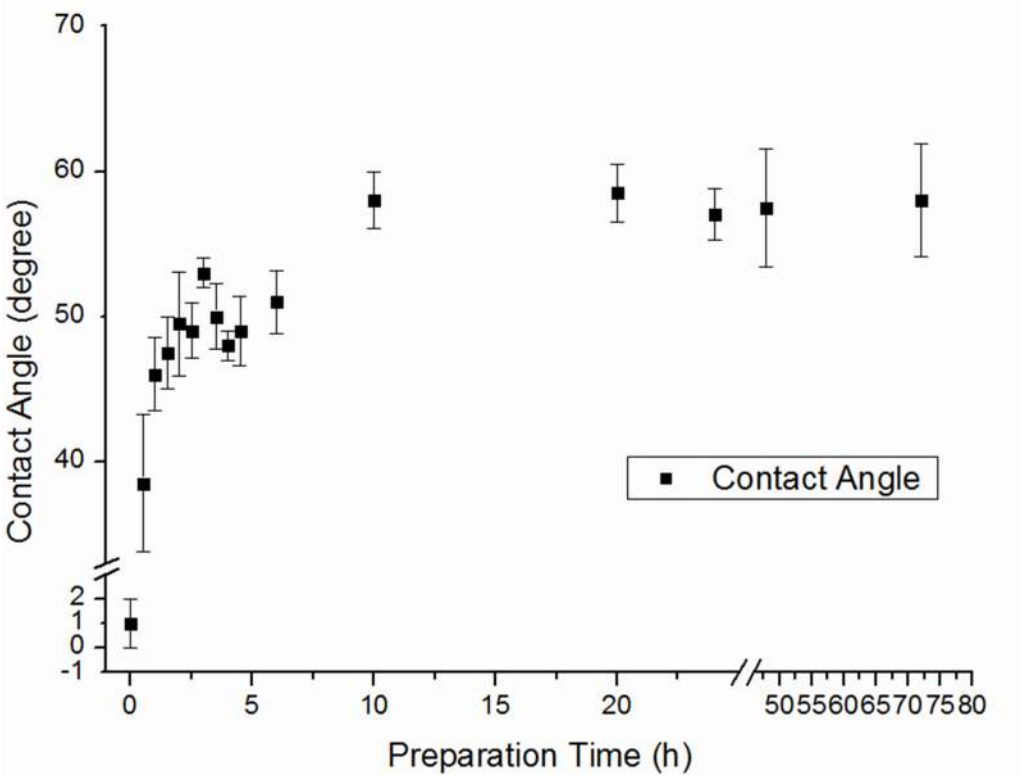

Figure 3.2 Contact angles of OEG silane SAM on silicon wafer substrate at different preparation times.

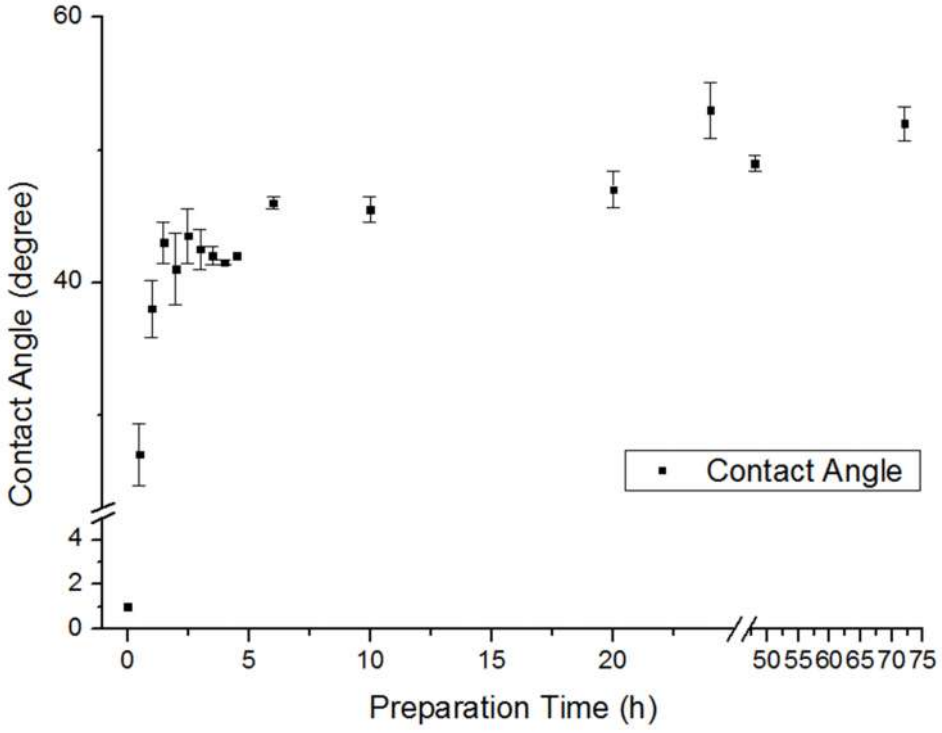

Figure 3.3 Contact angles of OEG silane SAM on mica at different preparation times.

3.3.2 Ellipsometric thickness

Because of the transparent nature of mica sheet, the emitted light source from ellipsometer is transmitted through the substrate after refraction, which makes it unable to detect the reflected light. Thus, only the silicon substrate was used to carry out ellipsometric measurement in this experiment. The ellipsometric thickness of OEG silane adsorbed on silicon, measured in air, was shown in figure 3.4. Given the theoretical average molecule length of the OEG silane studied is approximately 2.6 nm, it can be seen that the monolayer was nearly completely formed in 3 h when the monolayer thickness was 2.35 nm. From 3 h to 10 h, the thickness increased very little with time passed by, staying around 2.4 nm to 2.6 nm. After 10 h, the thickness began to increase, reaching a value of 5.1 nm at 20 h. The increase in thickness was attributed to the polymerization of OEG silane resulting in the formation of multilayer. These data and conclusion are consistent with the contact angle measurements and indicate that the monolayer was formed after ca. 3.5 h. The condition of the surface appears to change little until an immersion time of ca. 10 h in the solution.

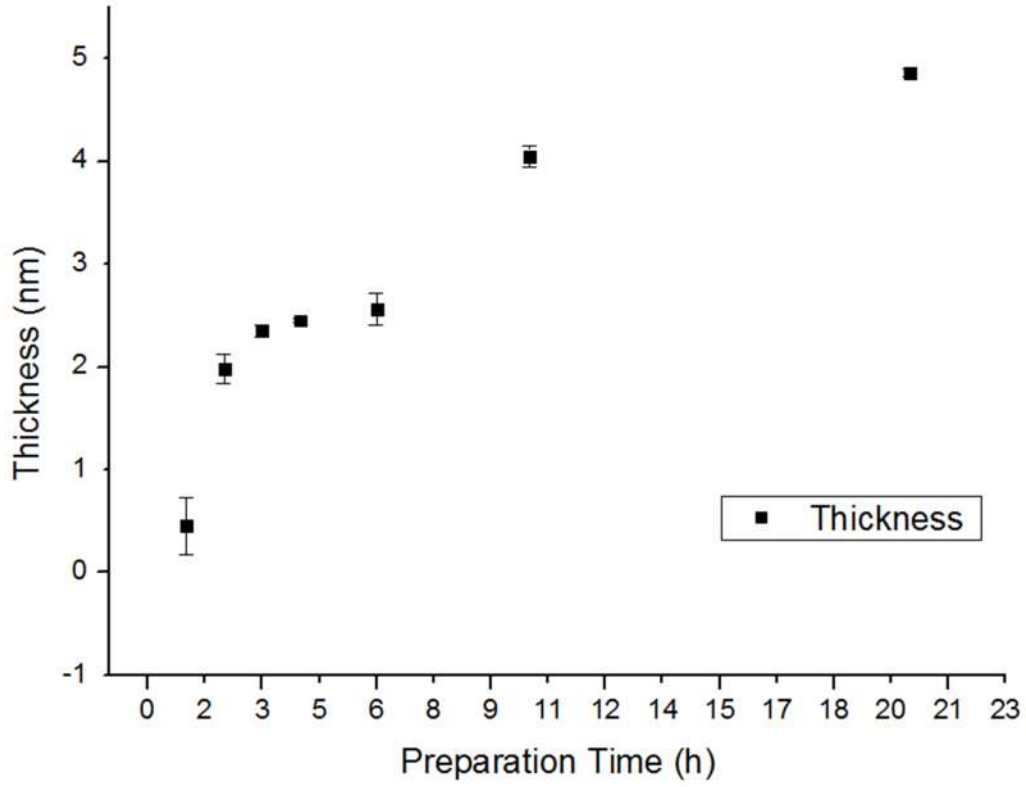

Figure 3.4 Variation in surface thickness as a function of preparation time of OEG silane on silicon wafer substrate.

3.3.3 AFM roughness measurement and height imaging

AFM was used to measure the root mean square (RMS) roughness of the samples. RMS is the root mean square average of the profile height deviations from the mean line, recorded within the evaluation length. The RMS roughness is calculated as follows [122]:

$$R_q = [(1/L) \int_0^L Z^2 (x) dx]^{1/2} \qquad (3.3)$$

where L is the evaluation length and Z(x) equals to the profile height function. By looking into the topography of the surfaces directly, AFM roughness measurement was the most efficient way to observe the samples. Figure 3.5 shows the variation in the surface roughness of OEG SAMs on silicon wafer substrates as a function of preparation time. Figure 3.6 shows the variation in surface roughness on mica substrate in comparison.

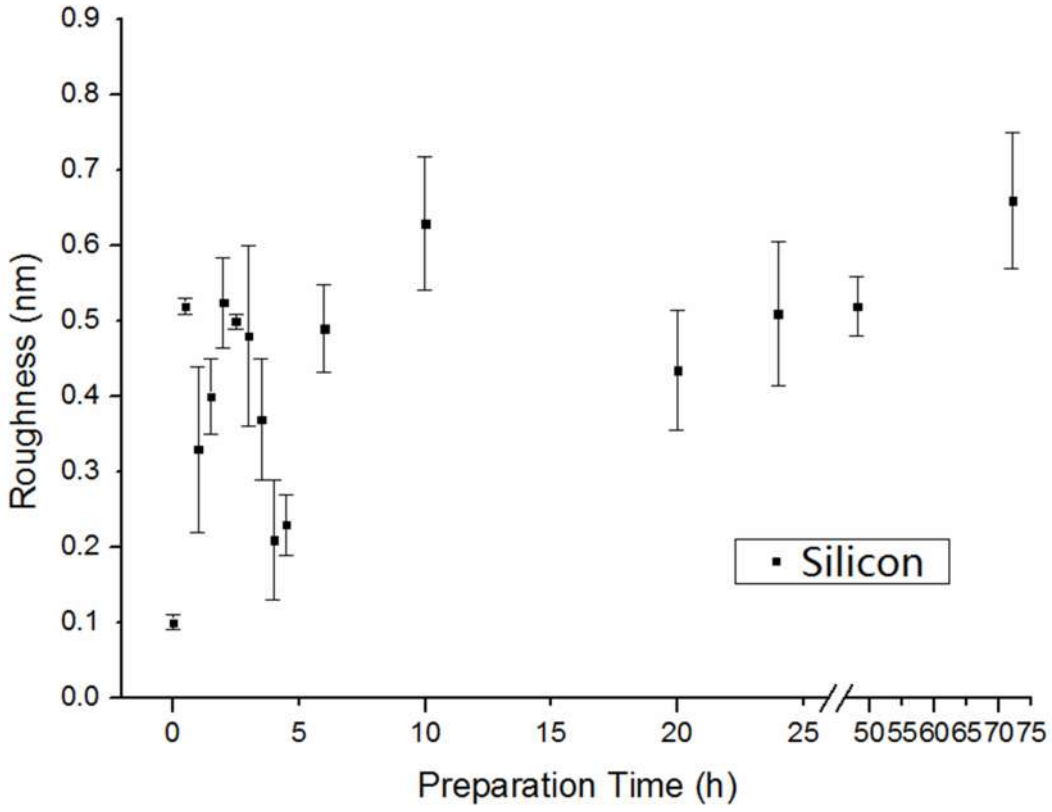

Figure 3.5 Variation in the surface roughness of OEG SAMs on silicon wafer substrates at different preparation time.

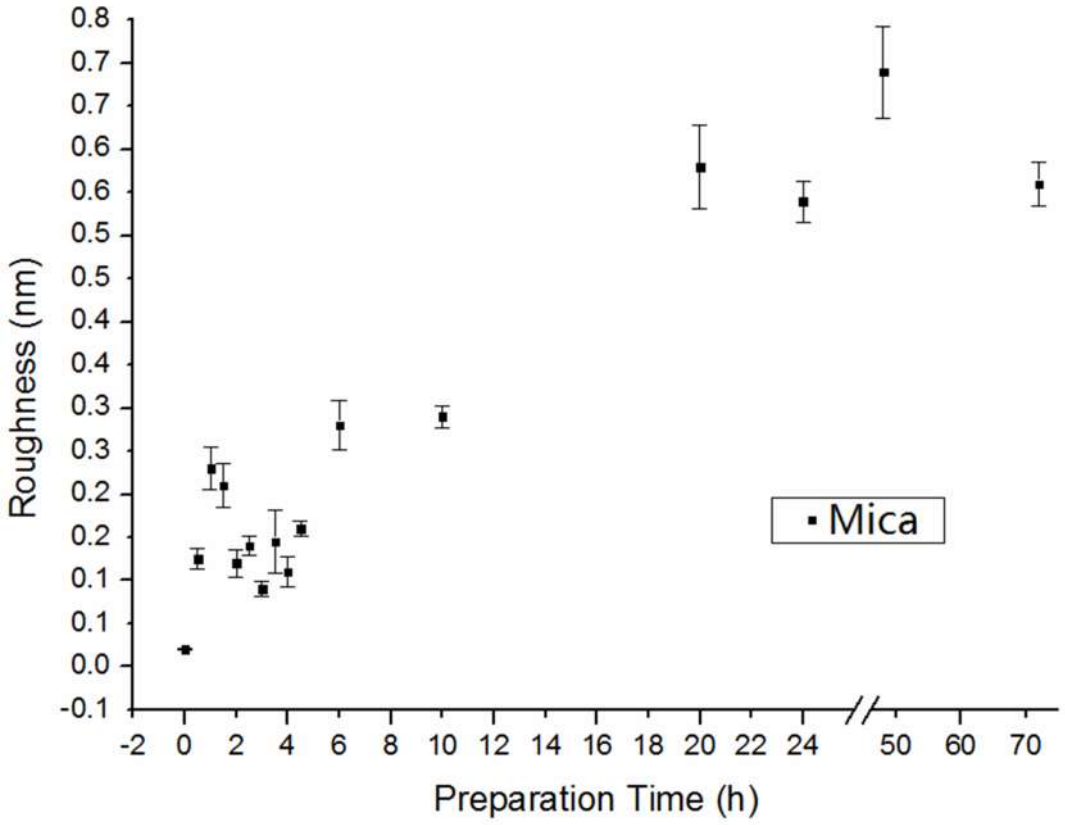

Figure 3.6 Variation in the surface roughness of OEG SAMs on mica sheet substrates at different preparation time.

In the first 3 h of immersion in the solution of adsorbate molecules, the roughness is typically in the range 0.4 – 0.6 nm on silicon substrate. However on mica, the majority of the measurements are 0.2 nm or less. Between 2 h and 4.5 h, all samples displayed a RMS roughness below 0.2 nm and reached the limiting value 0.086 nm. Only after times of ca. 10 h did the roughness of the films on mica approach that of the films formed on silicon. For both substrates, the roughness was at a minimum between 3.5 h to 4.5 h when the surface roughness was about 0.24 nm on silicon and ca. 0.1 nm on mica.

Figure 3.7 shows the AFM height images of OEG silane SAM on silicon after different preparation times. Figure 3.8 shows the images on mica substrate in size 5µm * 5µm at different preparation times.

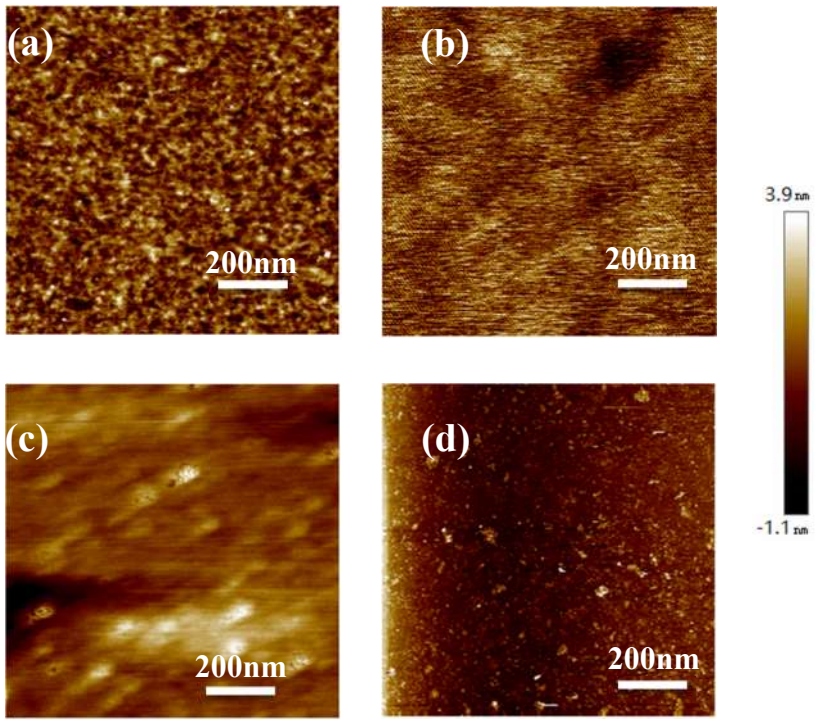

Figure 3.7 AFM height images of OEG silane SAM on silicon substrate (figure size 1μm * 1μm; z-range 5nm) at different preparation times. (a) 3h; (b) 4.5h; (c) 10h; (d) 20h.

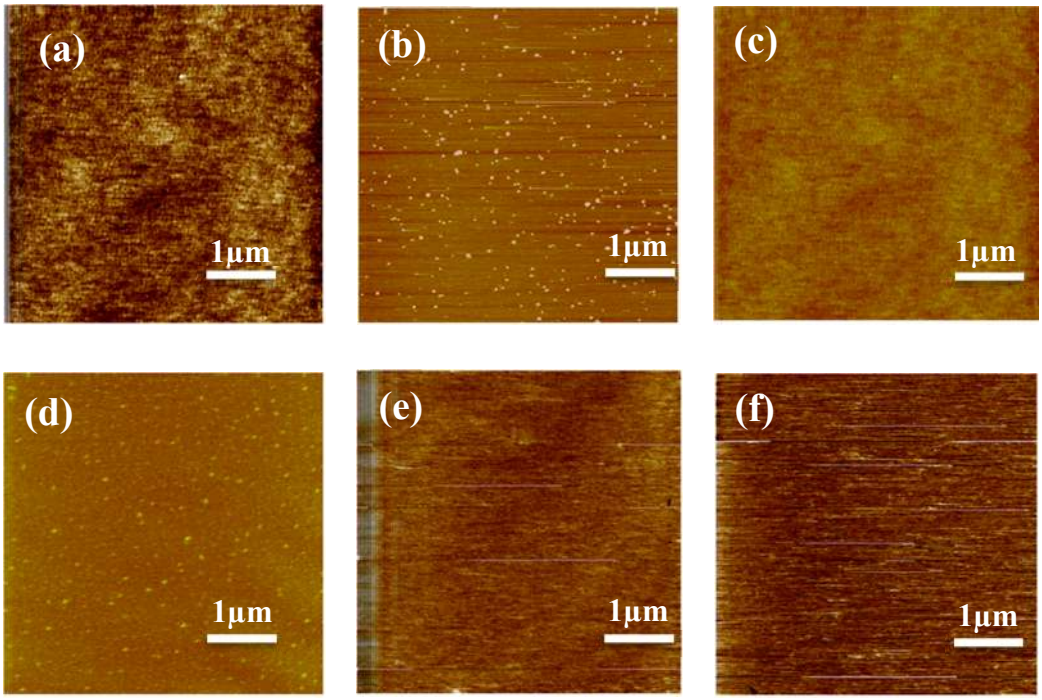

Figure 3.8 AFM height images of OEG silane SAM on mica substrate (figure size 5μm * 5μm; z-range 5.5nm) at different preparation times. (a) 1h; (b) 2h; (c) 3.5h; (d)

5h; (e) 10h; (f) 24h.

Quantitatively, the AFM height images are consistent with the RMS roughness data. After 2 h (figure 3.8b), some bright dots can be seen. Those dots were probably formed by OEG silane group firstly attached on mica surface and they were gone after another 1.5 h (figure 3.8c). At this point, the surface was the smoothest. After that, the surface sightly grew rougher, as is shown in figure 3.8e and figure 3.8f. Similarly, the roughness was minimized in figure 3.7b, when the 'islands' formed by OEG silane groups in figure 3.7a disappearred.

3.3.4 XPS analysis

The C1s spectra of OEG silane on both silicon and mica were obtained, as is shown in figure 3.9 and figure 3.10, respectively. The main peaks at 286.7eV represent the C-O bond while the secondary peaks at 285eV represent the C-C bond. The ratio of the C-O bond and the C-C bond is about 4:1, which disagrees with the molecular formula of OEG silane used. According to the formula shown in figure 3.9, the ratio of the C-O bond and the C-C bond should be between 7:1 and 10:1. The results of the contact angle measurements were relatively high which suggested the surfaces were hydrophobic. Thus this discrepancy was caused by the degradation of OEG chain by UV irradiation during preparation or the X-ray irradiation during the XPS rather than hydrocarbon contamination. Besides, in figure 3.10, the peaks at 293.5eV and 296.5eV are attributed to the potassium present in the mica.

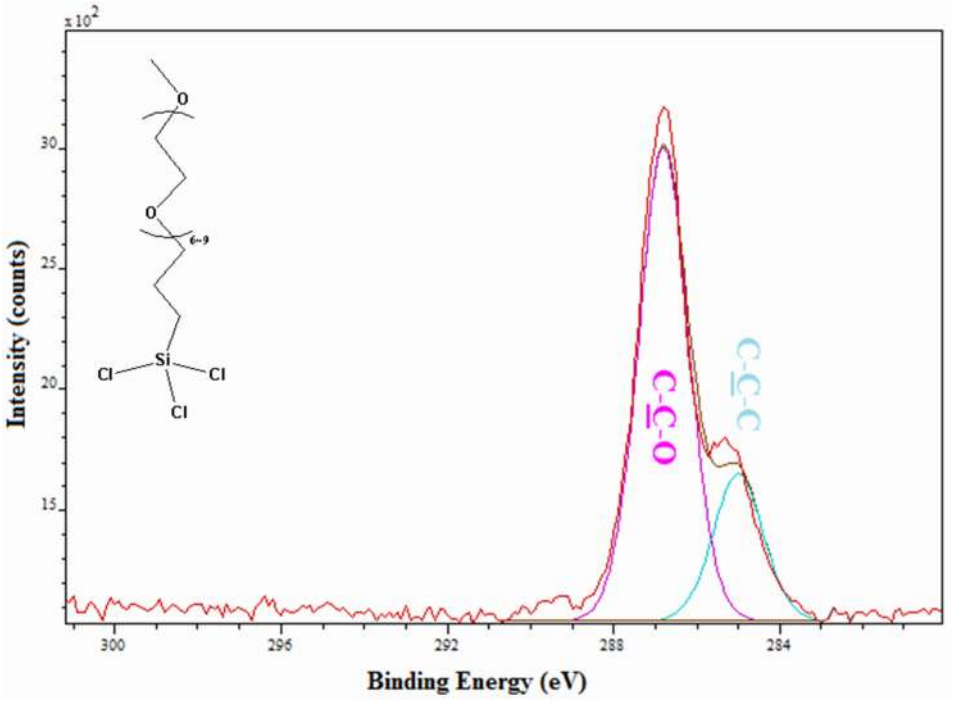

Figure 3.9 C1s spectrum of OEG silane on silicon substrate.

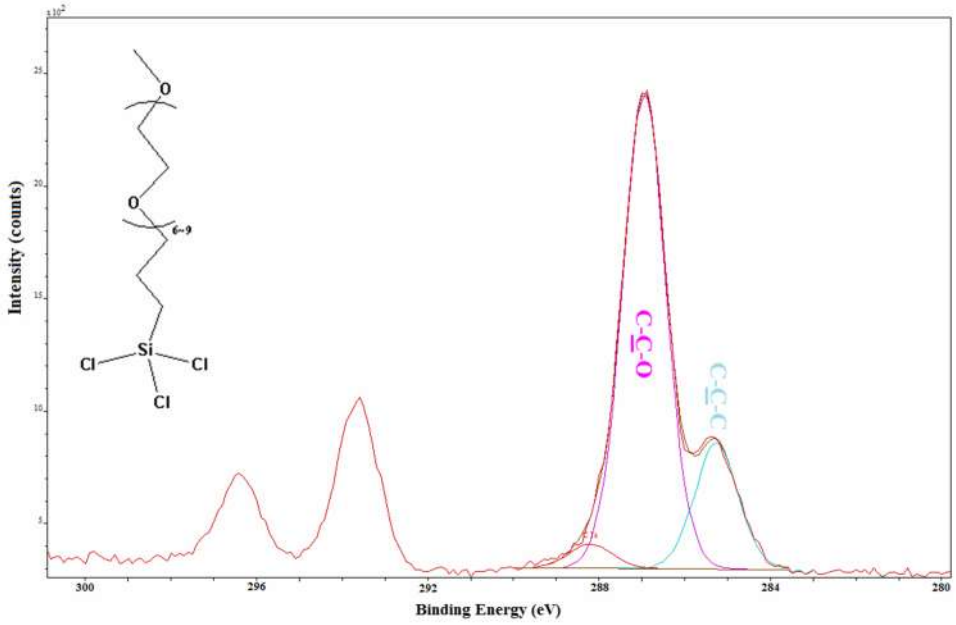

Figure 3.10 C1s spectrum of OEG silane on mica substrate.

3.4 Conclusion

A study has been completed of the adsorption of an OEG functionalised trichlorosilane onto silicon and mica. Contact angle measurements yielded limiting value of ca. 60° on both substrates. Monolayer formation was completed after ca. 3 h, but a small decrease in the contact angle was observed after 3.5 h to 4 h. The contact angle decreased between 3.5 h to 4.5 h preparation time which implied the SAM on the surface was smoother and well-ordered was observed. Contact angles on mica substrate were generally smaller than those on silicon substrate. The ellipsometric thickness of the SAM was about 2.5 nm at after 3 h which was consistent with the theoretical length of the OEG silane molecule. AFM roughness had been studied and height images were obtained. These results of roughness and topography of the surfaces were in good agreement with the results from ellipsometric thickness measurement and contact angle measurement showing that the optimum preparation time of OEG silane for both substrates was around 3.5 h to 4.5 h while mica was more suitable in producing smoother surfaces. XPS C1s spectra on both substrates had ensured the formation of OEG silane SAM on the sample surfaces.

Chapter 4. Micrometer and nanometer-scale protein patterning using oligo(ethylene glycol) (OEG) 4-nitrophenylethoxycarbonyl (NPEOC) protected 3-aminopropyltriethoxysilane (APTES) monolayers on mica

4.1 Introduction

Protein patterning at micrometer and nanometre scales has been achieved by the utilization of surface lithographic techniques, in combination with protein resistance at SAMs and protein immobilization methods. Selective removal of protein-resistance adsorbates enables adsorption of biomolecules at the surface. A variety of techniques have been developed for the formation of patterns in protein resistance monolayers. Dip-pen nanolithography (DPN) was invented and developed by Mirkin *et al.* in 1999[48]. DPN relies on the transfer from an AFM probe to surface molecules that have a high affinity for the surface[49-51]. However, the formation of patterns over large areas is very slow using DPN. Nanoshaving, as an elimination lithography technique, uses an AFM tip to remove adsorbates molecules from a fully formed SAM in the presence of a second adsorbate which assembles into the bare regions forming a molecular pattern[48,53]. Multiple component surfaces with high spatial precision down to sub-100 nm are achievable. However, as with DPN, the process is serial in nature and thus slow. Electron beam lithography (EBL) was developed for patterning nanometre scale features (as small as sub-10 nm) because, while diffraction effects limit the improvement in resolution of conventional photolithography, the wavelength of electrons is much smaller and diffraction is not a problem on nanometre length scales[56,59]. Scanning near field optical lithography (SNP) was developed in the author's laboratory and was used in this project. In SNP, a UV laser is combined with a scanning near field optical microscope to produce a near field source that can be used to carry our photochemical modification of a surface at high resolution. SNP is an alternative method to produce features with lateral resolution as good as 9 nm[60],

significantly smaller than the diffraction limit and rivalling the resolution of electron beam lithography. Sun *et al.*[64] formed patterns by using SNP to modify monolayers of both alkylthiolates and 4-chloromethylphenylsilane. In the former case, near field exposure caused photooxidation of the adsorbate head group, enabling its replacement by a contrasting thiol. In the latter case, near field exposure caused dehalogenation and subsequent conversion of the chloromethyl group to a carboxylic acid. Credgington *et al.* [63] reported similar nanostructures formed on conjugated polymers such as poly(*p*-phenylene vinylene), PPV and crosslinkable poly(9,9'-dioctylfluorene) with a lateral resolution below 60 nm ($<\lambda/5$). An alternate approach to photopatterning that combines high resolution with a capacity for exposure of large area is interferometric lithography (IL), in which two laser beams interfere to produce an interference pattern consisting of alternating bonds of constructive and destructive interference with a sinusoidal intensity cross section. In this study, a Lloyd's mirror interferometer, consisting of a sample and a mirror set at an angle 10° to each other was used.

A significant advantage of using photolithographic techniques for protein patterning is the extensive synthetic reactions following the photolithography that have been described by numerous researchers over the past decade[88-93]. The utilization of 'protecting groups' allows reactive functional groups to be protected until after selective photolithography has been performed. Alang Ahmad *et al.* [62, 125] reported the photochemistry of nitrophenylpropyloxycarbonyl protected aminopropyltriethoxysilane (NPPOC-APTES), which underwent photocleavage under UV exposure to yield an amine terminated surface. Without the addition of carbonyl scavenger, NPPOC-APTES accomplished a superior photodeprotection efficiency by yielding an alkene byproduct to display an amine terminate group at the surface. By immersing photomodified specimens in solutions of different reagents, surface derivatization could be achieved[125-127]. Subsequently, oligo (ethylene glycol) (OEG) modified 2-nitrophenylethoxycarbonyl (NPEOC) protected aminopropyltriethoxysilane (OEG-NPEOC-APTES) was introduced[123]. This molecule, like NPPOC-APTES, uses a nitrophenol group to protect an amine, but additionally has an OEG substituent on the phenyl ring. The mechanism of its photodeprotection process is shown in scheme 4.1. The OEG chain which was substituent at either the

m- or the p- position relative to the nitro group on the phenyl of NPEOC promoted the ability of protein nonspecific adsorption resistance [128].

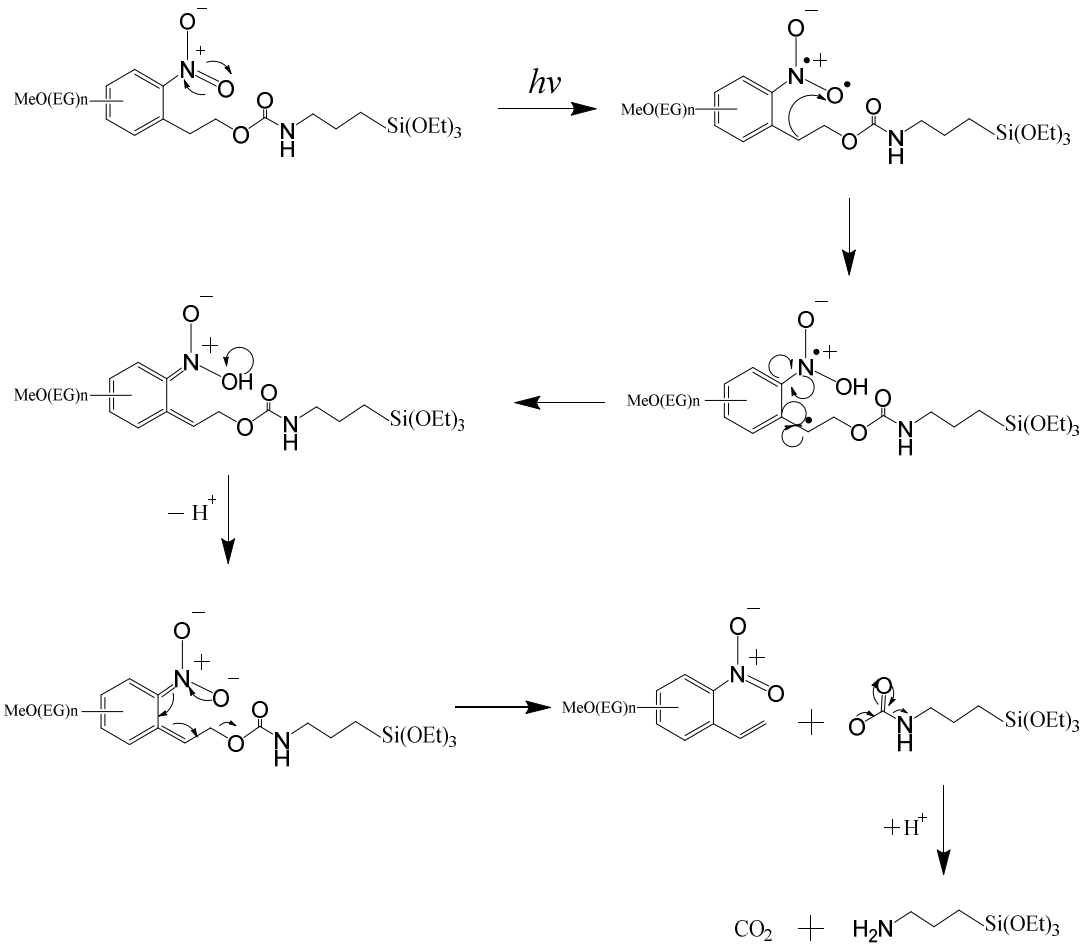

Scheme 4.1 The mechanism of the photodeprotection process of OEG-NPEOC-APTES.[124]

It can be seen that the protecting group of OEG-NPEOC-APTES is photo-cleaved from the film yielding carbon dioxide and leaving APTES attached to the surface. APTES sites are suitable for the immobilization of proteins. To activate APTES monolayer for protein attachment, a cross-linker (glutaraldehyde) was reacted with the samples. Glutaraldehyde is a bifunctional cross-linking agent, with an aldehyde group at each end, one for surface attachment to APTES and the other for protein binding.

4.2 Experimental

Oligo (ethylene glycol) (OEG) modified 2-nitrophenylethoxycarbonyl (NPEOC) protected aminopropyltriethoxysilane (OEG-NPEOC-APTES) was synthesized by AF ChemPharm Ltd. Protein GFP and LH2 were supplied by co-worker Dr M. Carton Department of molecular Biology and Biotechnology, University of Sheffield. Glutaraldehyde solution (Grade Ⅱ, 50% in water), phosphate buffered saline (PBS) and HEPES were bought from Sigma-Aldrich. Hydrogen peroxide solution (100 volumes >30%), sulphuric acid (95%), ammonia solution(S. G. 0.88, 35%) were supplied by Fisher Chemical and ethanol (absolute) was supplied by VWR international S.A.S. Toluene (HPLC grade) was supplied by departmental dry solvent system and de-ionised water was obtained from Veolia water system (PureLab Ultra) from ELGA. Nitrogen gas was supplied by departmental compressed gas system. All the Chemicals mentioned above were used as received.

Mica sheets were immersed in 1mM OEG-NPEOC-APTES toluene solution for 24 h and were washed by rinsing with toluene 3 times before being ultrasonically cleaned for 5 min. The samples were blown dry under a nitrogen gas stream. All samples were placed in clean sealed tubes and annealed in the vacuum oven for 1h at 120ºC. Samples were wrapped in foil to prevent exposure to light. Five annealed NPEOC samples were sent to XPS analysis. Only the element of nitrogen was analysed during the close scan which took 400 s each and every sample was scanned for 6 times. The transformation under exposure to X-ray was tested by XPS spectra analysing of these samples.

For micro patterns, samples were covered by a copper mask (1000, 1500 or 2000 mesh squared grids) (Agar, Cambridge, UK), then by a transparent clean quartz disk in order to keep the mask in position during subsequent manipulation, and finally exposed to a 244 nm wavelength UV laser beam from a Coherent Innova 300C frequency doubled argon ion laser. The laser intensity was varied between 10-100 mW and had a diameter approximately 2-3 mm. Samples were washed and ultrasonically cleaned in PBS solution before being immersed in glutaraldehyde (25% v/v) (GA) water solution. Then samples were washed with water from a washbottle. Finally, samples were incubated in a solution of GFP in PBS buffer overnight.

Samples were rinsed with PBS buffer solution 3 times and stored by immersion in PBS buffer solution in a fridge (4 ºC) prior to further experiments. All the operations were carried out in a dark room. Schematic representations of preparation procedures are as shown in scheme 4.2.

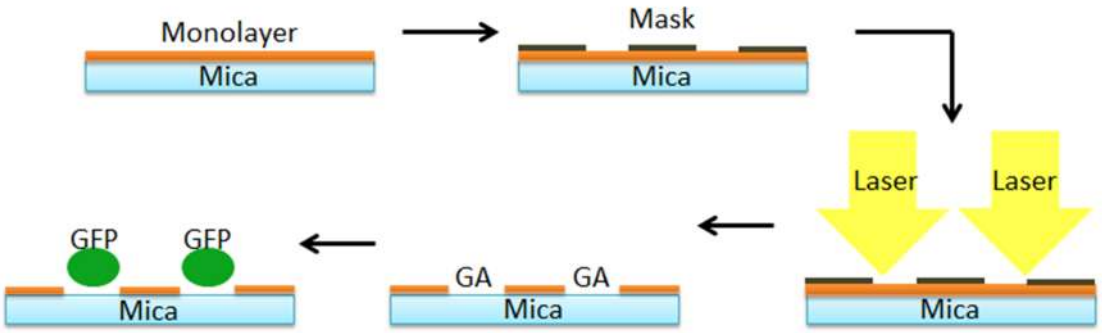

Scheme 4.2 Schematic representations of the manipulation procedures of fabricating a micron scale pattern using a mask.

Nanoscale patterning was carried out using a Witec AlphaSNOM coupled to a HeCd laser (325 nm). Cantilever probe with hollow pyramidal tips were used. Within the near field of the sample surface, the probe was moved through the surface as programmed. Six nano lines were 'drawn'. The length of each line was 70 µm and the width between two lines was 10 µm. The scanning speed of the SNP was 1 µm/s. GFP was immobilized onto the sample surface as for micron pattern discussed above. The exposed regions with GFP were observed under confocal laser scanning microscopy to obtain the fluorescence images of samples in both scales. A fluorescence image would not only show the shape and width of the pattern, but also indicate that the immobilization of other proteins (i.e. LH1, LH2) could be possible.

Interferometric lithography (IL) was carried out using a Lloyd's mirror interferometer coupled to the frequency doubled argon ion laser. The beam was focused to cover ca. 1 cm^2. LH2 was immobilized onto the IL patterned surface. Exposed samples were treated with glutaraldehyde water solution (25% v/v). Then samples were washed with water from a washbottle. Finally, samples were immersed in a solution of LH2 crystal in HEPES buffer overnight. Samples were rinsed with HEPES buffer solution 3 times and stored by immersion in HEPES buffer solution in a fridge (4 ºC) prior to further experiments. All the operations were carried out in a dark room. The manipulation

procedures are shown in scheme 4.3. AFM height images and cross section of the sample surfaces would be obtained to test whether OEG-NPEOC-APTES film was a suitable material for nanoscale patterning and protein immobilization. The cross section of the height image, the thickness of the exposed regions would reveal the existence of LH2.

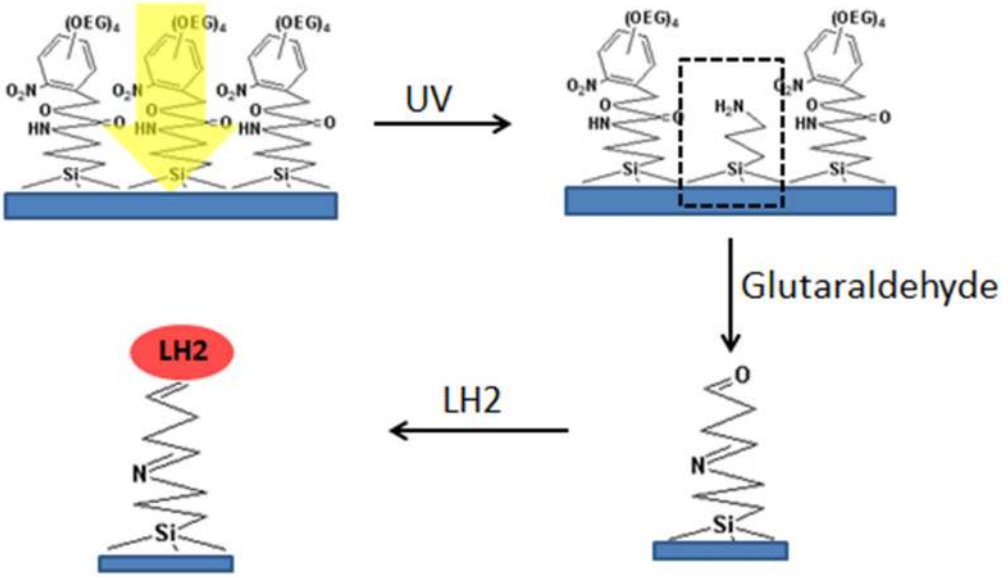

Scheme 4.3 Schematic representations of the manipulation procedures and the mechanism of fabricating a patterned surface.

4.3 Results and discussion

4.3.1 Characterisation of OEG-NPEOC-APTES

XPS C1s and N1s spectra were obtained to confirm the successful formation of OEG-NPEOC-APTES film on mica substrate. The spectra are shown in figure 4.1 (C1s) and figure 4.2 (N1s). In C1s spectrum, three components were fitted, although there should be 4 types of carbon atoms in the compound. The peak at 285 eV is attributed to the aromatic ring carbons and aliphatic carbons. The peak at 286.5 eV is attributed to two carbon atoms that are singly bonded to oxygen and to nitrogen. The chemical shifts for these two components are too close for them to be resolved. The peak at 289.2 eV presents the carbons in the carbamate group. The two peaks between 293 eV and 298 eV are attributed to the potassium atoms in the mica substrate. The N1s spectrum is simpler, in figure 4.2. Two components were fitted due to the two types of nitrogen in the compound. The nitro group contributes to the peak at 406 eV while the amino group contributes to the peak at 400 eV. The chemical shifts of the components in the spectra are in good agreement with chemical structure of OEG-NPEOC-APTES on mica substrate which confirm the formation of the film.

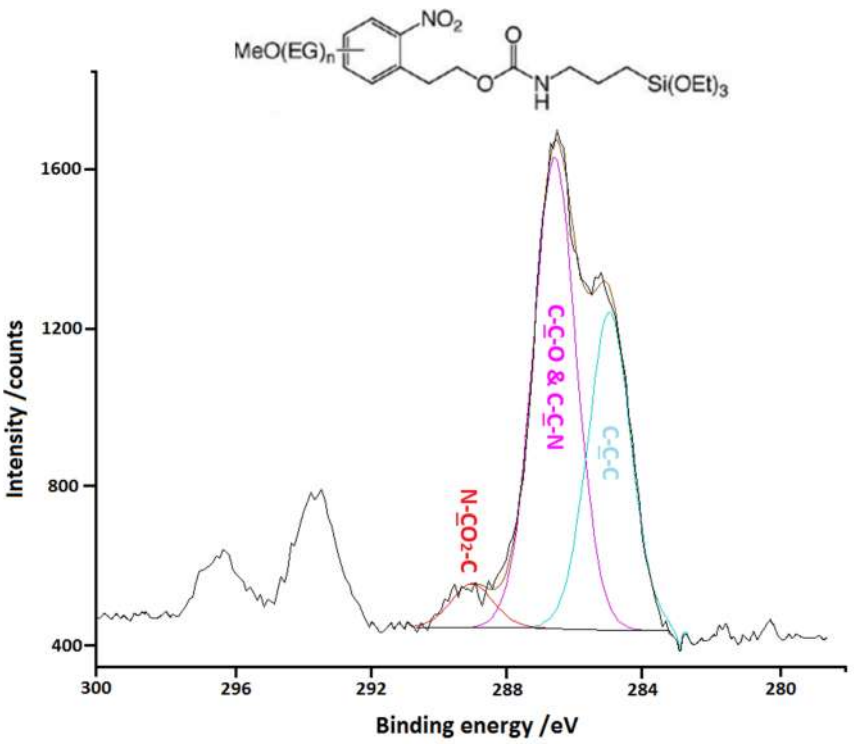

Figure 4.1 XPS C1s spectrum of OEG-NPEOC-APTES.

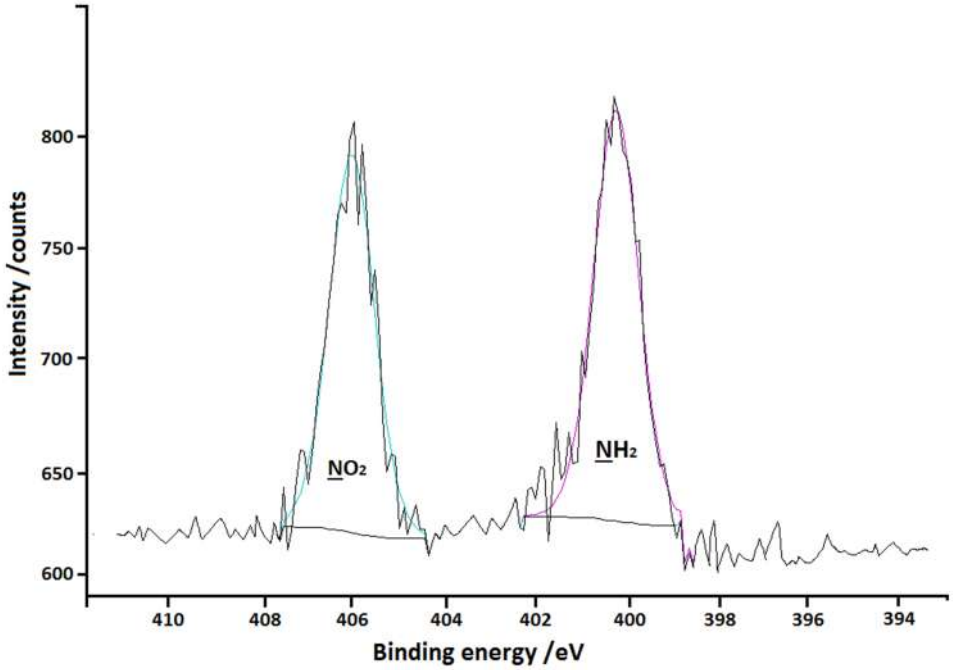

Figure 4.2 XPS N1s spectrum of OEG-NPEOC-APTES.

The possibility that X-ray damage occurred during analysis of OEG-NPEOC-APTES was studied, by acquiring a large number of spectra at regular intervals of time. The N1s spectra of the 6 scans of one single sample are shown in figure 4.3. In the top spectrum, where the exposure time is 400 s, the ratio of the peak regions of NO_2/NH_2 is ca. 1 which agrees very well with the molecular formula. When the exposure time increases to 800 s, the intensity of the nitro group is slightly reduced compared to that of the amine group, while the amine peak area stays unchanged over the 6 scans. After 2400 s, the NO_2/NH_2 ratio has reduced to 0.2. The variation in the ratio of NO_2/NH_2 as a function of the X-ray exposure time is shown in figure 4.4. As can be seen from the graph, the ratio of the peak regions between nitro group and amino group decreases as the exposure time increases. Hence, this result suggests that cleavage of the protecting group does occur over extended exposure.

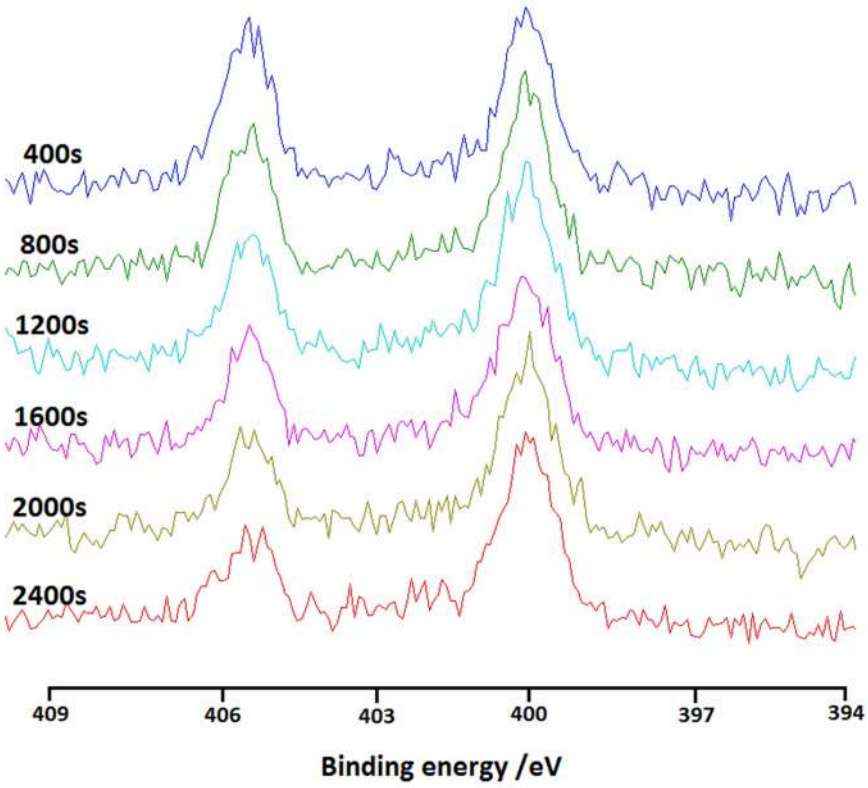

Figure 4.3 Variation in N1s spectrum of OEG-NPEOC-APTES as a function of exposure time to X-ray.

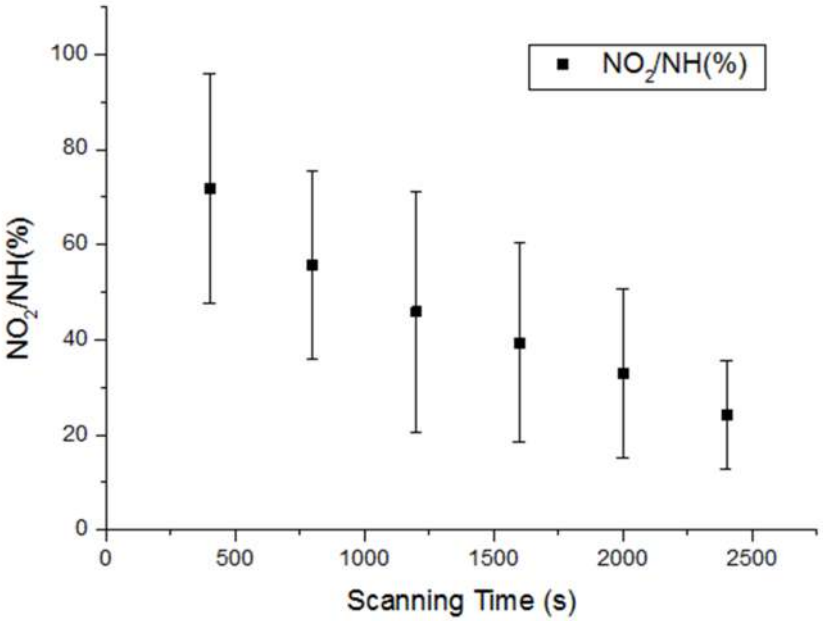

Figure 4.4 Variation in the ratio of NO_2/NH_2 as a function of the X-ray exposure time.

4.3.2 Micron and nanometre scale patterns of GFP

Micron patterns were produced by exposing OEG-NPEOC-APTES films to 244 nm UV light with an exposure of 4 J/cm^2 through a mask. The adsorbates in the exposed regions were expected to be deprotected, leading to an increase in surface energies. The friction force images were obtained and are shown in figure 4.5. The exposed regions (squares in figure 4.5) exhibited slightly increased contrast, consistent with the small increase in surface energy expected after removal of the protecting groups. From the cross section recorded for the friction force image, the surface energy of these square regions are higher than the bars in between where were masked during the exposure. The distance between two bars is 12μm.

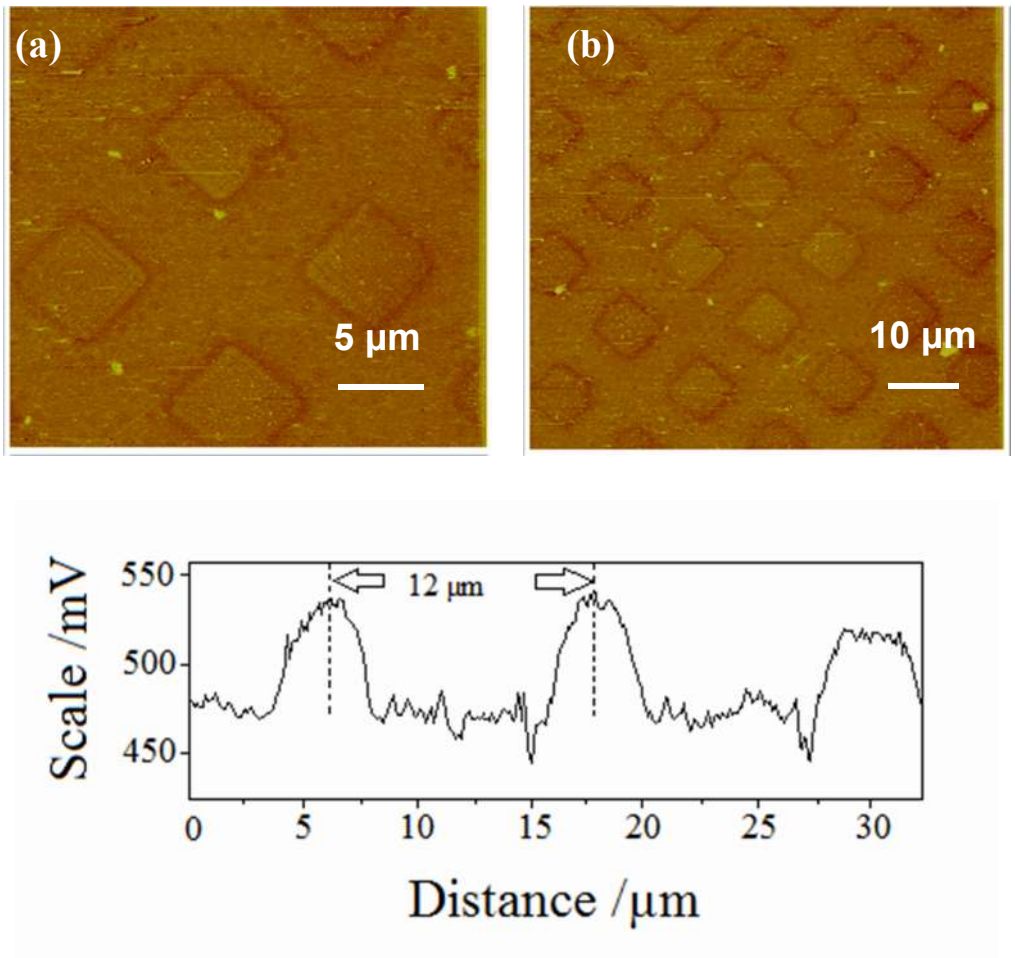

Figure 4.5 AFM friction force images and the cross section of 244nm UV light photodeprotected OEG-NPEOC-APTES micron pattern in dose 4 J/cm^2, size: (a) 30μm*30μm; (b) 60μm*60μm.

Nano lines were produced by scanning near field photolithography. The SNOM system was coupled to a HeCd laser (325 nm) for these studies. Six nano lines were 'drawn'. The length of each line was 70µm and the width between two lines was 10µm. The scanning speed of the SNP was 1µm/s. The friction force image and cross section of the nano lines was obtained and shown in the figure 4.6. The cross section of a nano line indicates the width of each line is 500nm. The clear cross section and the contrast between lines and unexposed area imply that scanning near field photolithography is an efficient approach to fabricate well-defined nanometre patterns.

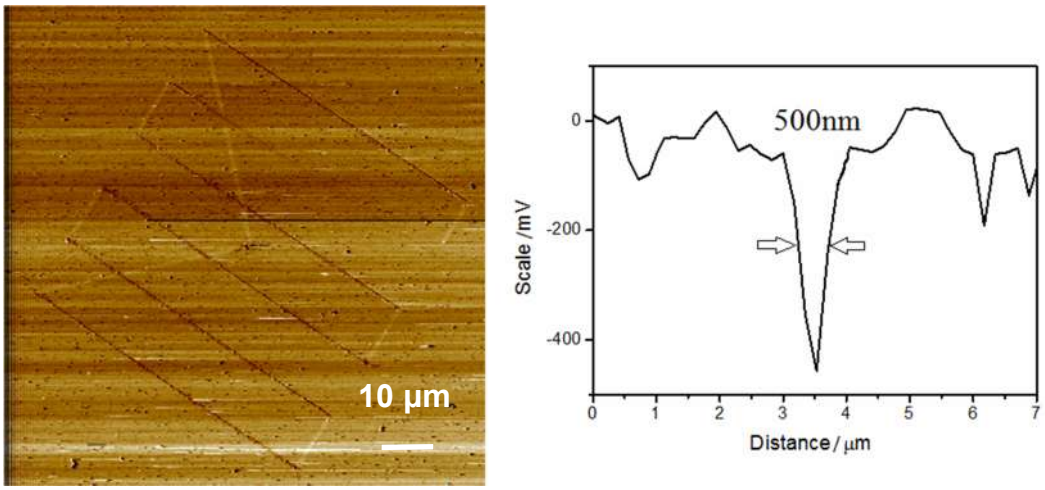

Figure 4.6 AFM friction force image and the cross section of scanning near field photolithography coupled with a 325nm UV light photodeprotected OEG-NPEOC-APTES nanometre pattern at a scanning speed of 1µm/s, size: 75µm*75µm.

After the deprotected surfaces were activated to protein immobilizations by glutaraldehyde, GFP was covalently immobilized. The unexposed area was still covered by OEG-NPEOC protecting group which provided the surface with protein resistance. In the modified areas, one of the aldehyde groups in glutaraldehyde reacted with the amine group from the APTES on the sample and the other aldehyde group reacted with the amine group in GFP, enabling the attachment of GFP in the modified areas. Fluorescence images of micron and nanometre scale GFP patterns on photodeprotected OEG-NPEOC-APTES are shown in figure 4.7. The clear contrast implies that well-defined patterns of GFP were formed. The dark bars in figure 4.7 (a, b) and the dark background in figure 4.7 (c, d) indicate that nonspecific adsorption was blocked very effectively by OEG-NPEOC group while bright fluorescence

observed in the exposed areas (the squares in figure 4.7a, b) and the lines in figure 4.7 (c, d). The width of the nano lines in figure 4.7 (c, d) were measured as ca. 500nm by their fluorescence which agrees with the friction force image.

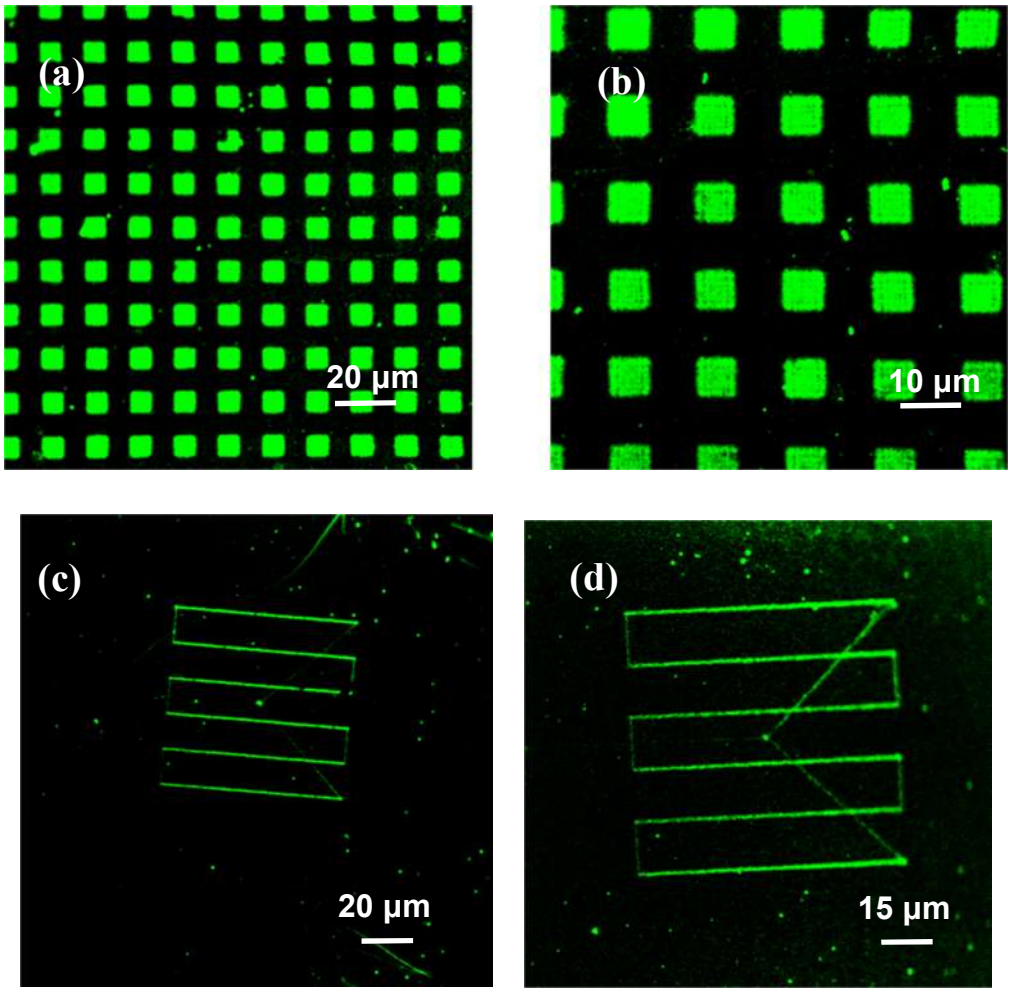

Figure 4.7 Fluorescence images of different GFP patterns on photodeprotected OEG-NPEOC-APTES. (a,b) micron patterns; (c,d) nanopatterns by SNP.

4.3.3 Nanometre scale pattern by IL and LH2 immobilization

4.3.3.1 Characterizing of LH2

As discussed in section 1.3.2, the bacteriochlorophylls (BChls) in LH2 absorb light at wavelengths 800 and 850 nm at room temperature. The UV-vis absorption spectrum of a solution of LH2 crystal (0.1% v/v, HEPES buffer, pH=7.4) is shown in figure 4.8. The two peaks at 800 and 850 nm indicate that the LH2 used was in appropriate condition and function. Subsequently, LH2 was immobilized on the glutaraldehyde-APTES surface using LH2 solutions in different concentrations. The variation in dry

thickness of LH2 layer on glutaraldehyde-APTES surface as a function of different concentrations is shown in figure 4.9. When the concertation of LH2 was relatively high (i. e. 1% v/v), the thickness of immobilized LH2 layer on the surface was 3.3nm. This value of the layer thickness was lower than the height of LH2 molecules. It is probably because the ellipsometric thickness measurement was carried out in the air which meant the protein molecules were dry and had lower conformational freedom. As the concentration of LH2 solution declined, the thickness of the LH2 layer fell significantly which indicated that 1% v/v was the most appropriate concentration for LH2 immobilization.

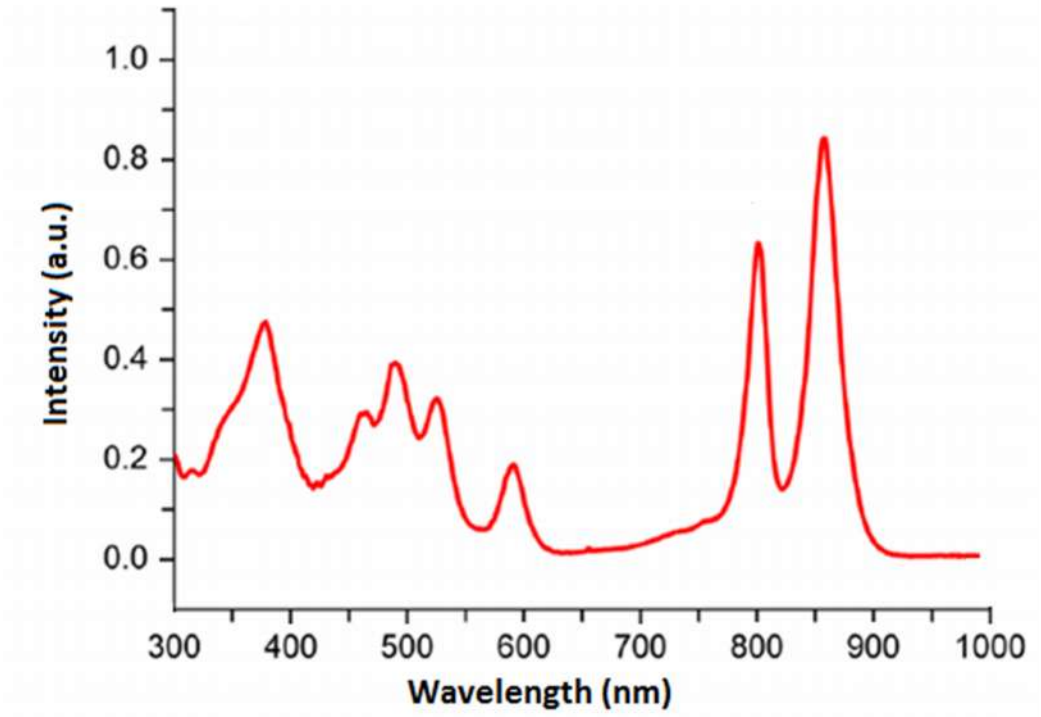

Figure 4.8 UV-vis absorption spectrum obtained from LH2 solution (0.1% v/v, HEPES buffer, pH=7.4).

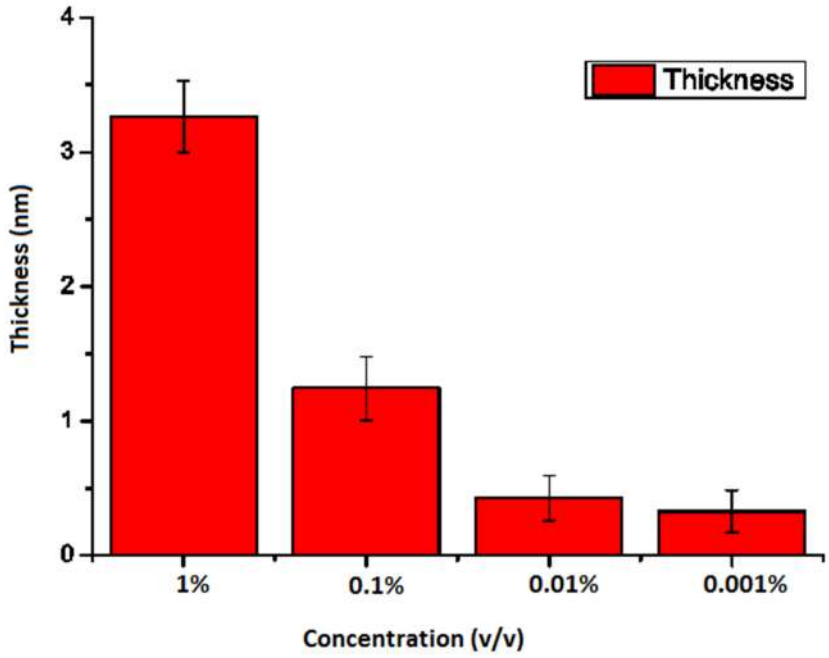

Figure 4.9 Variation in dry thickness of LH2 layer on glutaraldehyde-APTES surface as a function of different concetrations.

4.3.3.2 Friction force and height images of IL patterns

OEG-NPEOC-APTES surfaces were also patterned by IL. The angle of the two interfering beams was 10° . Thus, the width of the parallel lines which resulted was approximately 250nm. The friction force image and the cross section of the exposed sample surface were shown in figure 4.10. The bright and dark contrast lines in the image indicate that the superposition of the 244nm UV light produced well-defined higher surface energy regions where the LH2 would be suitable to be immobilized. Subsequently, the surface was activated using cross linker glutaraldehyde, and LH2 was immobilized onto the patterned samples. AFM height images and cross section of the sample surface were obtained and shown in figure 4.11. From the cross section of the height image, the thickness of the LH2 is ca. 3.8nm which agrees with the maximum thickness of the ellipsometric thickness measurement above.

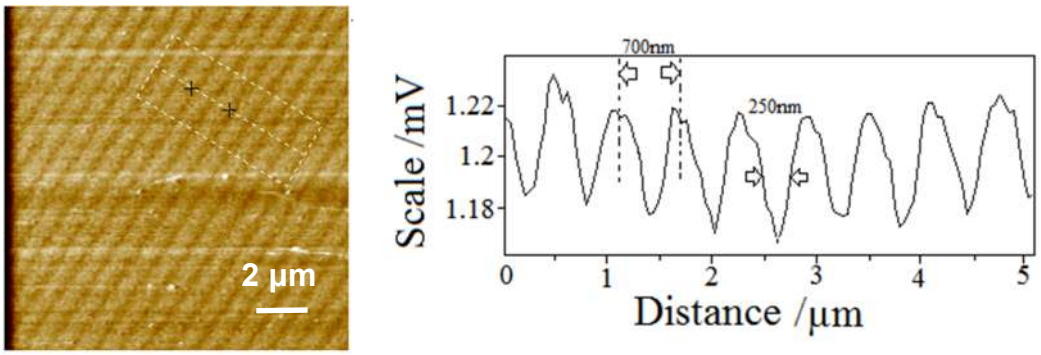

Figure 4.10 AFM friction force image and cross section of photodeprotected OEG-NPEOC-APTES surface patterned by IL. Size: 10µm*10µm, Angle 10°, Dose = 4 Jcm^{-2}.

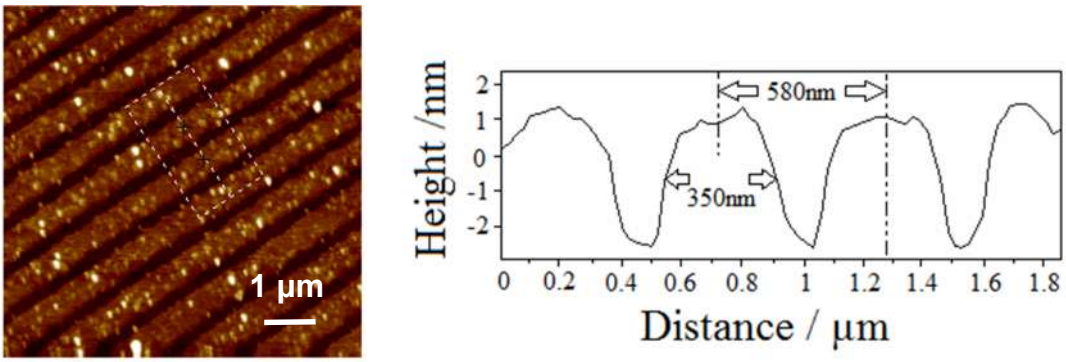

Figure 4.11 AFM height image and cross section of photodeprotected OEG-NPEOC-APTES surface patterned by IL. Size: 5µm*5µm.

4.4 Conclusion

OEG-NPEOC-APTES films on mica were fabricated. The behaviour of the OEG-NPEOC-APTES surface on exposure to X-ray was studied by comparing the XPS N1s spectra as a function of time. It was shown that the OEG-NPEOC protecting group was removed by X-ray exposure. Micron and nanometre scale patterns were yielded by mask-based and SNP methods. GFP was immobilized on the exposed regions of these samples. Fluorescence images of samples in both scales were obtained. IL was also utilized to fabricate nanometre scale patterns. LH2 was immobilized on samples fabricated by IL. AFM height image illustrated the thickness of the LH2 layer on the patterned regions. Well-defined patterns were obtained in all methods implying that photodeprotected OEG-NPEOC-APTES was a suitable material for protein patterning in various scales with various proteins.

Chapter 5. Conclusion

The present study has shown the successful fabrication of nanostructured assemblies of light-harvesting proteins by scanning near-field photolithography and interferometric lithography. Characterization was also carried out on the surfaces fabricated utilizing confocal laser scanning microscopy and AFM.

In chapter 3, SAMs of an oligo (ethylene glycol) functionalized trichlorosilane were formed successfully on both mica and silicon substrates. The contact angles stayed stable between 3.5 h to 4.5 h preparation time which implied the SAMs on the both substrates smooth and well-order monolayers at this time. The ellipsometric thickness measurement of the SAM was about 2.5 nm which was in good agreement with the contact angle result. AFM roughness and height images were obtained to observe the topography of the surfaces. It was illustrated that 3.5 h to 4.5 h was the optimum preparation time of OEG silane for both substrates while mica was more suitable in producing smoother surfaces.

In chapter 4, OEG-NPEOC-APTES films on mica substrates were successfully fabricated. It is shown that the OEG-NPEOC protecting group was removed by X-ray exposure. Micron and nanometre scale patterns were yielded by mask-based and SNP methods. GFP was immobilized on the exposed regions of these samples. Fluorescence images of samples in both scales were obtained. IL was also utilized to fabricate nanometre scale patterns. LH2 was immobilized on samples fabricated by IL. AFM height image illustrated the thickness of the LH2 layer on the patterned regions. Well-defined patterns were obtained in all methods implying that photodeprotected OEG-NPEOC-APTES was a sensational material for protein patterning in various scales with various proteins.

In the process of assembling low-dimensional constructs that incorporate membrane molecules and synthesizing the macromolecule structures that replicate the behavior of membrane systems, protein patterns of LH1 and LH2 at nanometer scale could be used as the platform to build up the low-dimensional system that replicates the bacterial photosynthetic apparatus on a chip. Thus, fabricating a well-defined OEG-

terminated silane SAM or OEG-NPEOC-APTES film as the foundation of membrane proteins was critical.

LH1 and other dye molecules could be immobilized on the nanoscale patterns. The spectrum of each component in the nanoscale patterns of proteins could be studied. It is hypothesized that there will be an energy shift due to the protein-protein interactions at nanometer scale. OEG-NPEOC-APTES surface functionalized with NTA could be utilized on other substrates like IL-fabricated gold nanostructures to prepared oriented protein patterns. The image resolution of LH2 patterns on SAMs could be increased by using high resolution AFM.

References:

1. Onclin, S.; Ravoo, B. J.; Reinhoudt, D. N. *Angewandte Chemie International Edition* **2005**, *44* (39), 6282–6304.
2. Netzer, L.; Sagiv, J. *Journal of the American Chemical Society* **1983**, *105* (3), 674–676.
3. Peterson, I. R. *Journal of Physics D: Applied Physics* **1990**, *23* (4), 379–395.
4. Zasadzinski, J.; Viswanathan, R; Madsen, L; Garnaes, J; Schwartz, D. *Science* **1994**, *263* (5154), 1726–1733.
5. NETZER, L.; ISCOVICI, R.; SAGIV, J. *Langmuir–Blodgett Films, 1982* **1983**, 235–241.
6. Netzer, L.; Iscovici, R.; Sagiv, J. *Thin Solid Films* **1983**, *99* (1-3), 235–241.
7. Bain, C. D.; Evall, J.; Whitesides, G. M. *Journal of the American Chemical Society* **1989**, *111* (18), 7155–7164.
8. Whitesides, G. M.; Laibinis, P. E. *Langmuir* **1990**, *6* (1), 87–96.
9. Schlenoff, J. B.; Li, M.; Ly, H. *Journal of the American Chemical Society* **1995**, *117* (50), 12528–12536.
10. Sellers, H. *Surface Science* **1993**, *294* (1-2), 99–107.
11. Geng, W. T.; Nara, J.; Ohno, T. *Thin Solid Films* **2004**, *464-465*, 379–383.
12. Nuzzo, R. G.; Zegarski, B. R.; Dubois, L. H. *Journal of the American Chemical Society* **1987**, *109* (3), 733–740.
13. Fenter, P.; Eisenberger, P.; Liang, K. S. *Physical Review Letters* **1993**, *70* (16), 2447–2450.
14. Chidsey, C. E. D.; Liu, G.-Y.; Rowntree, P.; Scoles, G. *The Journal of Chemical Physics* **1989**, *91* (7), 4421.
15. Ulman, A. *Chemical Reviews* **1996**, *96* (4), 1533–1554.
16. Haehner, G.; Woell, C.; Buck, M.; Grunze, M. *Langmuir* **1993**, *9* (8), 1955–1958.
17. Angst, D. L.; Simmons, G. W. *Langmuir* **1991**, *7* (10), 2236–2242.
18. Rye, R. R.; Nelson, G. C.; Dugger, M. T. *Langmuir* **1997**, *13* (11), 2965–2972.
19. Inoue, A.; Mizutani, W.; Ishida, T.; Choi, N.; Tokumoto, H. *Applied Surface Science* **1999**, *144-145*, 425–429.

20. Tripp, C. P.; Hair, M. L. *Langmuir* **1992**, *8* (4), 1120–1126.
21. Aswal, D. K.; Lenfant, S.; Guerin, D.; Yakhmi, J. V.; Vuillaume, D. *Analytica Chimica Acta* **2006**, *568* (1-2), 84–108.
22. Jia, Z.; Chen, S.; Zhang, J. *Journal of Applied Polymer Science* **2012**, *127* (4), 3017–3025.
23. London, G.; Carroll, G. T.; Feringa, B. L. *Organic & Biomolecular Chemistry* **2013**, *11* (21), 3477-3483.
24. Crampton, N.; Bonass, W. A.; Kirkham, J.; Thomson, N. H. *Ultramicroscopy* **2006**, *106* (8-9), 765–770.
25. Facci, P.; Alliata, D.; Andolfi, L.; Schnyder, B.; Kötz, R. *Surface Science* **2002**, *504*, 282–292.
26. Thomas, R. C.; Yang, H. C.; DiRubio, C. R.; Ricco, A. J.; Crooks, R. M. *Langmuir* **1996**, *12* (9), 2239–2246.
27. Doudevski, I.; Schwartz, D. K. *Journal of the American Chemical Society* **2001**, *123* (28), 6867–6872.
28. Rozlosnik, N.; Gerstenberg, M. C.; Larsen, N. B. *Langmuir* **2003**, *19* (4), 1182–1188.
29. Li, S.-S.; Xu, L.-P.; Wan, L.-J.; Wang, S.-T.; Jiang, L. *The Journal of Physical Chemistry B* **2006**, *110* (4), 1794–1799.
30. Angst, D. L.; Simmons, G. W. *Langmuir* **1991**, *7* (10), 2236–2242.
31. Tan, M.; Zhang, H.; Wang, Y.; Hongtao; Zhu, J.; Han, J. *Applied Surface Science* **2008**, *254* (20), 6332–6336.
32. Schreiber, F. *Progress in Surface Science* **2000**, *65* (5-8), 151–257.
33. Brewer, N. J.; Janusz, S.; Critchley, K.; Evans, S. D.; Leggett, G. J. *The Journal of Physical Chemistry B* **2005**, *109* (22), 11247–11256.
34. Dishner, M. H.; Hemminger, J. C.; Feher, F. J. *Langmuir* **1996**, *12* (26), 6176–6178.
35. Hutt, D. A.; Leggett, G. J. *The Journal of Physical Chemistry* **1996**, *100* (16), 6657–6662.
36. Ni, L.; Dietlin, C.; Chemtob, A.; Croutxé-Barghorn, C.; Brendlé, J. *Langmuir* **2014**, *30* (33), 10118–10126.

37. Ye, T.; McArthur, E. A.; Borguet, E. *The Journal of Physical Chemistry B* **2005**, *109* (20), 9927–9938.
38. Kumar, A.; Whitesides, G. M. *Applied Physics Letters* **1993**, *63* (14), 2002-2004.
39. Scavia, G.; Porzio, W.; Destri, S.; Barba, L.; Arrighetti, G. *European Polymer Journal* **2010**, *46* (8), 1660–1670.
40. Chen, T.; Jordan, R.; Zauscher, S. *Polymer* **2011**, *52* (12), 2461–2467.
41. Hidber, P. C.; Helbig, W.; Kim, E.; Whitesides, G. M. *Langmuir* **1996**, *12* (5), 1375–1380.
42. Béduer, A.; Seichepine, F.; Flahaut, E.; Vieu, C. *Microelectronic Engineering* **2012**, *97*, 301–305.
43. Kim, M.-S.; Lee, D.-H.; Cha, Y.-H.; Kim, K.-B.; Jung, S.-H.; Lee, J.-K.; O, B.-H.; Lee, S.-G.; Park, S.-G. *Microelectronic Engineering* **2014**, *123*, 33–37.
44. Szilasi, S. Z.; Huszank, R.; Csik, A.; Cserháti, C.; Rajta, I. *Nuclear Instruments and Methods in Physics Research Section B: Beam Interactions with Materials and Atoms* **2009**, *267* (12-13), 2296–2298.
45. Garra, J.; Long, T.; Currie, J.; Schneider, T.; White, R.; Paranjape, M. *Journal of Vacuum Science & Technology A: Vacuum, Surfaces, and Films* **2002**, *20* (3), 975-982.
46. Li, X.-M.; Huskens, J.; Reinhoudt, D. N. *Journal of Materials Chemistry* **2004**, *14* (20), 2954-2971.
47. Mrksich, M.; Whitesides, G. M. *Trends in Biotechnology* **1995**, *13* (6), 228–235.
48. Piner, R. D. *Science* **1999**, *283* (5402), 661–663.
49. Ding, L.; Li, Y.; Chu, H.; Li, X.; Liu, J. *The Journal of Physical Chemistry B* **2005**, *109* (47), 22337–22340.
50. McKendry, R.; Huck, W. T. S.; Weeks, B.; Fiorini, M.; Abell, C.; Rayment, T. *Nano Letters* **2002**, *2* (7), 713–716.
51. Garcia, R.; Martinez, R. V.; Martinez, J. *Chem. Soc. Rev.* **2006**, *35* (1), 29–38.
52. Hong, S. *Science* **2000**, *288* (5472), 1808–1811.
53. Xu, S.; Liu, G. *Langmuir* **1997**, *13* (2), 127–129.
54. Chwang, A. B.; Granstrom, E. L.; Frisbie, C. D. *Advanced Materials* **2000**, *12* (4), 285–288.
55. Amro, N. A.; Xu, S.; Liu, G. *Langmuir* **2000**, *16* (7), 3006–3009.

56. In *Supramolecular Chemistry: From Molecules to Nanomaterials*; Wiley-Blackwell (an imprint of John Wiley & Sons Ltd): United Kingdom, 2012.
57. Chang, J.; Zhou, Q.; Zettl, A. *Applied Physics Letters* **2014**, *105* (17), 173109-1-4.
58. Ballav, N.; Thomas, H.; Winkler, T.; Terfort, A.; Zharnikov, M. *Angewandte Chemie International Edition* **2009**, *48* (32), 5833–5836.
59. Love, C. J.; Estroff, L. A.; Kriebel, J. K.; Nuzzo, R. G.; Whitesides, G. M. *Chemical Reviews* **2005**, *105* (4), 1103–1170.
60. Sun, S.; Leggett, G. J. *Nano Letters* **2004**, *4* (8), 1381–1384.
61. Rogers, J. A. *Journal of Vacuum Science & Technology B: Microelectronics and Nanometer Structures* **1998**, *16* (1), 59-68.
62. Ahmad, S. A. A.; Wong, L. S.; ul-Haq, E.; Hobbs, J. K.; Leggett, G. J.; Micklefield, J. *Journal of the American Chemical Society* **2009**, *131* (4), 1513–1522.
63. Credgington, D.; Fenwick, O.; Charas, A.; Morgado, J.; Suhling, K.; Cacialli, F. *Advanced Functional Materials* **2010**, *20* (17), 2842–2847.
64. Sun, S.; Montague, M.; Critchley, K.; Chen, M.-S.; Dressick, W. J.; Evans, S. D.; Leggett, G. J. *Nano Letters* **2006**, *6* (1), 29–33.
65. Solak, H. H.; He, D.; Li, W.; Singh-Gasson, S.; Cerrina, F.; Sohn, B. H.; Yang, X. M.; Nealey, P. *Applied Physics Letters* **1999**, *75* (15), 2328-2330.
66. Xia, D.; Ku, Z.; Lee, S. C.; Brueck, S. R. J. *Advanced Materials* **2010**, *23* (2), 147–179.
67. Tizazu, G.; El-Zubir, O.; Brueck, S. R. J.; Lidzey, D. G.; Leggett, G. J.; Lopez, G. P. *Nanoscale* **2011**, *3* (6), 2511-2516.
68. Tsargorodska, A.; Zubir, O. E.; Darroch, B.; Cartron, M. L.; Basova, T.; Hunter, N. C.; Nabok, A. V.; Leggett, G. J. *ACS Nano* **2014**, *8* (8), 7858–7869.
69. Ahmad, S. A.; Leggett, G. J.; Hucknall, A.; Chilkoti, A. *Biointerphases* **2011**, *6* (1), 8-15.
70. Tizazu, G.; Zubir, O. el; Patole, S.; McLaren, A.; Vasilev, C.; Mothersole, D. J.; Adawi, A.; Hunter, N. C.; Lidzey, D. G.; Lopez, G. P.; Leggett, G. J. *Biointerphases* **2012**, *7* (1-4), 1–9.
71. Brueck, S. R. J. *Proceedings of the IEEE* **2005**, *93* (10), 1704–1721.

72. Davenport, D.; Nicol, J. A. C. *Proceedings of the Royal Society B: Biological Sciences* **1955**, *144* (916), 399–411.
73. M. Kneen, J. Farinas, Y. Li and A. S. Verkman, Biophysical Journal, 1998, 74, 1591–1599..
74. Prasher, D. C.; Eckenrodeb, V. K.; Wardc, W. W.; Prendergastd, F. G.; Cormierb, M. J. **1992**.
75. Sullivan, K. F. *Fluorescent Proteins, Volume 85*, 2nd ed.; Sullivan, K. F., Ed.; Elsevier Science: United States, 2007.
76. Orm, M.; Cubitt, A. B.; Kallio, K.; Gross, L. A.; Tsien, R. Y.; Remington, S. J. *Science* **1996**, *273* (5280), 1392–1395.
77. Shaner, N. C.; Steinbach, P. A.; Tsien, R. Y. *Nature Methods* **2005**, *2* (12), 905–909.
78. Durnford, D. G.; Deane, J. A.; Tan, S.; McFadden, G. I.; Gantt, E.; Green, B. R. *Journal of Molecular Evolution* **1999**, *48* (1), 59–68.
79. Harris, E. H. *The Chlamydomonas Sourcebook: Volume 1-3*; Stern, D., Witman, G., Eds.; Academic Press: Amsterdam, 2008.
80. Papiz, M. Z.; Prince, S. M.; Howard, T.; Cogdell, R. J.; Isaacs, N. W. *Journal of Molecular Biology* **2003**, *326* (5), 1523–1538.
81. Prince, S. M.; Howard, T. D.; Myles, D. A. A.; Wilkinson, C.; Papiz, M. Z.; Freer, A. A.; Cogdell, R. J.; Isaacs, N. W. *Journal of Molecular Biology* **2003**, *326* (1), 307–315.
82. Cogdell, R. J.; Isaacs, N. W.; Freer, A. A.; Arrelano, J.; Howard, T. D.; Papiz, M. Z.; Hawthornthwaite-Lawless, A. M.; Prince, S. *Progress in Biophysics and Molecular Biology* **1997**, *68* (1), 1–27.
83. Reynolds, N. P.; Janusz, S.; Escalante-Marun, M.; Timney, J.; Ducker, R. E.; Olsen, J. D.; Otto, C.; Subramaniam, V.; Leggett, G. J.; Hunter, N. C. *Journal of the American Chemical Society* **2007**, *129* (47), 14625–14631.
84. Ikemoto, H.; Tubasum, S.; Pullerits, T.; Ulstrup, J.; Chi, Q. *The Journal of Physical Chemistry C* **2013**, *117* (6), 2868–2878.
85. Stamouli, A.; Kafi, S.; Klein, D. C. G.; Oosterkamp, T. H.; Frenken, J. W. M.; Cogdell, R. J.; Aartsma, T. J. *Biophysical Journal* **2003**, *84* (4), 2483–2491.

86. McDermott, G.; Prince, S. M.; Freer, A. A.; Hawthornthwaite-Lawless, A. M.; Papiz, M. Z.; Cogdell, R. J.; Isaacs, N. W. *Nature* **1995**, *374* (6522), 517–521.
87. Hong, X.; Weng, Y.-X.; Li, M. *Biophysical Journal* **2004**, *86* (2), 1082–1088.
88. Kane, R. *Biomaterials* **1999**, *20* (23-24), 2363–2376.
89. Blawas, A. S.; Reichert, W. M. *Biomaterials* **1998**, *19* (7-9), 595–609.
90. Ahmad, S. A. A.; Wong, L. S.; ul-Haq, E.; Hobbs, J. K.; Leggett, G. J.; Micklefield, J. *Journal of the American Chemical Society* **2011**, *133* (8), 2749–2759.
91. Ahmad, S. A.; Hucknall, A.; Chilkoti, A.; Leggett, G. J. *Langmuir* **2010**, *26* (12), 9937–9942.
92. Muir, B. W.; Fairbrother, A.; Gengenbach, T. R.; Rovere, F.; Abdo, M. A.; McLean, K. M.; Hartley, P. G. *Advanced Materials* **2006**, *18* (23), 3079–3082.
93. Zhou, F.; Huck, W. T. S. *Physical Chemistry Chemical Physics* **2006**, *8* (33).
94. Ostuni, E.; Chapman, R. G.; Holmlin, E. R.; Takayama, S.; Whitesides, G. M. *Langmuir* **2001**, *17* (18), 5605–5620.
95. Besseling, N. A. M. *Langmuir* **1997**, *13* (7), 2113–2122.
96. T. Young, *Philosophical Transactions of the Royal Society of London*, 1805, **95**, 65–87.
97. J Bico, C Marzolin and D Quéré, *Europhysics Letters (EPL)*, 1999, **47**, 743–744.
98. R. M. A. Azzam and N. M. Bashara, *Ellipsometry and polarized light*, sole distributors for the U.S.A. and Canada, Elsevier North-Holland, Amsterdam, 1977.
99. P. Tengvall, I. Lundström and B. Liedberg, *Biomaterials*, 1998, **19**, 407–422.
100. A. Rothen, *Review of Scientific Instruments*, 1945, **16**.
101. J. W. Lichtman, *Scientific American*, 1994, **271**, 40–45.
102. M. Minsky, *Scanning*, 1988, **10**, 128–138.
103. B. Luck, K. Carlson, T. Collier and K.-B. Sung, *IEEE Potentials*, 2004, **23**, 14–17.
104. S. A. A. Ahmad, PhD Thesis, The University of Sheffield, 2009.
105. D. Briggs, D. R. Clarke, S. Suresh, I. M. Ward and M. H. Black, *Surface analysis of polymers by XPS and static SIMS*, Cambridge University Press, Cambridge, U.K., 1998.

106. D. Zemlyanov, Introduction to X-ray Photoelectron Spectroscopy and XPS application, Birck Nanotechnology Center, Purdue University, 2007.
107. *Webpage:* http://srdata.nist.gov/xps/.
108. G. Binnig, C. F. Quate and C. Gerber, *Physical Review Letters*, 1986, **56**, 930–933.
109. *Webpage:* http://www.mhhe.com/physsci/chemistry/carey5e/Ch02/ch2-2-1.html.
110. J. C. Vickerman, *Surface Analysis - the Principal Techniques*, John Wiley & Sons, United Kingdom, 1997.
111. P. Atkins and J. de Paula, *Atkins' Physical chemistry*, Oxford University Press c2002, New York, 2001.
112. I. Y. Sokolov and G. S. Henderson, *Surface Science*, 2002, **499**, 135–140.
113. Q. Zhong, D. Inniss, K. Kjoller and V. B. Elings, *Surface Science*, 1993, **290**.
114. L. K. Ista, FEMS Microbiology Letters, 1996, 142, 59–63.
115. S. R. Benhabbour, H. Sheardown and A. Adronov,Macromolecules, 2008, 41, 4817–4823.
116. M. Heuberger, T. Drobek and N. D. Spencer, Biophysical Journal, 2005, 88, 495–504.
117. S.-W. Lee and P. E. Laibinis, Biomaterials, 1998, 19, 1669–1675.
118. Z. Yang and H. Yu, Advanced Materials, 1997, 9, 426–429.
119. M. J. Harris, Ed., Poly(ethylene glycol) chemistry: Biotechnical and biomedical applications (topics in applied chemistry), Plenum Publishing Co.,N.Y., New York, 1st edn., 1992.
120. M. A. Fortes, Physicochemical Aspects of Polymer Surfaces, 1983, 107–139.
121. M. K. Chaudhury, Journal of Adhesion Science and Technology, 1993, 7, 669–675.
122. D. F. Parsons, R. B. Walsh and V. S. J. Craig, The Journal of Chemical Physics, 2014, 140, 164701.
123. A. Alang Ahmad, L. S. Wong, E. ul-Haq, J. K. Hobbs, G. J. Leggett and J. Micklefield, Journal of the American Chemical Society, 2011,133, 2749–2759.
124. S. A. A. Ahmad, PhD, The University of Sheffield, 2009.
125. S. A. Alang Ahmad, L. S. Wong, E. ul-Haq, J. K. Hobbs, G. J. Leggett and J.

Micklefield, Journal of the American Chemical Society, 2009,131, 1513–1522.
126. K. R. Bhushan, C. DeLisi and R. A. Laursen, Tetrahedron Letters, 2003, 44, 8585–8588.
127. M. C. Pirrung, L. Wang and M. P. Montague-Smith, Organic Letters, 2001, 3, 1105–1108.
128. M. Beier, Nucleic Acids Research, 2000, 28, 11e–11.

Abbreviation

AFM	Atomic force microscopy
AFPs	Autofluorescent proteins
APTES	Aminopropyltriethoxysilane
BChls	Bacteriochlorophylls
CMPTS	4-chloromethylphenylsiloxane
DPN	Dip-pen nanolithography
EBL	Electron beam lithography
EGFP	Enhanced green fluorescent protein
GFP	Green fluorescent protein
HEPES	4-(2-hydroxyethyl)-1-piperazineethanesulfonic acid
IL	Interferometric lithography
LH1	Light-harvesting complex I
LH2	Light-harvesting complex II
MeNPOC	R-methyl-o-nitropiperonyloxycarbonyl
NPEOC	2-nitrophenylethoxycarbonyl
NPPOC	Nitrophenylpropyloxycarbonyl
NPRW	Nanopen reader and writer
NVOC	O-nitroveratryloxycarbonyl
OEG	Oligo (ethylene glycol)
PBS	Phosphate buffered saline
PEG	Poly(ethylene glycol)
PFPA	Perfluorophenylazide
PMMA	Poly(methyl methacrylate)
POEGMA	Poly(oligoethylene glycol) methacrylate
RMS	Root mean square
SAMs	Self-assembled monolayers
SDS	Sodium dodecyl sulfate
SNOM	Scanning near field microscope
SNP	Scanning near field optical lithography
SPL	Scanning probe lithography

STM	Scanning tunnelling microscopy
UHV	Ultra-high vacuum
UV	Ultraviolet
wtGFP	Wild-type green fluorescent protein
XPS	X-ray photoelectron spectroscopy
μCP	Mirco-contact printing

List of Figures

List of Table

List of Scheme